NEW AND EFFECTIVE METHODS FOR PRODUCTION OF CEMENT-BASED PHOTOCATALYTIC MATERIALS

GUO MINGZHI

Ph.D

The Hong Kong Polytechnic University

2017

The Hong Kong Polytechnic University

Department of Civil and Environmental Engineering

NEW AND EFFECTIVE METHODS FOR PRODUCTION OF CEMENT-BASED PHOTOCATALYTIC MATERIALS

GUO MINGZHI

A thesis submitted in partial fulfilment of the

requirements for the degree of Doctor of Philosophy

JUNE 2016

CERTIFICATE OF ORIGINALITY

I hereby declare that this thesis is my own work and that, to the best of my knowledge and belief, it reproduces no material previously published or written, nor material that has been accepted for the award of any other degree or diploma, except where due acknowledgement has been made in the text.

_____ (Signed)

_____GUO MINGZHI_____ (Name of the student)

ABSTRACT

Photocatalytic functional cementitious materials have gained significant traction as people become increasingly aware of their living environments. With the natural energy (solar light) alone, various photocatalytic functions, such as air purification, can be realized. Extensive research has spurred the practical application of photocatalytic construction materials on a global scale. However, several challenges still limit their broader applications. Among them, a normally high cost and an impaired photocatalytic efficiency caused by encapsulation of TiO_2 by the cement hydration products stand out. Commonly, a trade-off has to be made between a high efficiency and a low cost. Therefore, achievement of good photocatalytic efficiencies with low amounts of TiO_2 implies considerable cost savings.

In this study, two novel methods have been developed to better incorporate nano-TiO_2 into two types of cementitious materials (namely self-compacting architectural mortar and concrete surface layers of eco-blocks). Recycled glasses derived from post-consumer beverage glass bottles were used as fine aggregates to replace natural river sand. The advantages of samples prepared by these new methods over those prepared by the traditional intermixing method were demonstrated in terms of photocatalytic degradation of various substances under various conditions.

For the architectural mortars, the traditional intermixing method was first adopted to combine TiO_2 with recycled glass for the purpose of enhancing the photocatalytic efficiency in terms of NO_x removal. The mechanical and durability properties of architectural mortars prepared with varying dosages of TiO_2 and recycled glass were also examined. It was found that the light transmittance property of recycled glass was responsible for the highest photocatalytic NO_x removal efficiency observed on the samples prepared with 100% recycled glass as aggregate and a dosage of 5% TiO_2. Adding more glass contents, coupled with increasing TiO_2 dosages, led to a slight reduction in both the compressive strength and flexural strength

(due to the formation of agglomerates) and an increase in both the ASR expansions and carbonation depths (but all the ASR expansions were below the permissible limit).

To fulfil the goal of increasing photocatalytic efficiencies while lowering the cost, an alternative strategy of applying a TiO_2 containing paint (PC-S7) on the surface of architectural mortars was investigated. The superior photocatalytic efficiency of the PC-S7-coated samples over the 5% TiO_2-intermixed counterparts was reflected by a wide range of photocatalytic activities. For example, the PC-S7-coated architectural mortars had both a significantly higher NO_x and xylene degradation performance in comparison with the 5% TiO_2-intermixed counterparts which achieved a much lower NO_x removal rate and failed to degrade xylene. In addition, the PC-S7-coated architectural mortars delivered a total inactivation of *E. coli* after 120 min of UVA irradiation, contrasting with a negligible *E. coli* killing activity by the 5% TiO_2-intermixed samples. Moreover, the PC-S7-coated samples also garnered a robust weathering-resistant ability, reflected by an almost unchanged ability to photocatalytic degrade RhB after exposure to either a facade weathering process or an accelerated carbonation process.

Investigation on the photocatalytic architectural mortars gave rise to an intriguing finding that white cement (WC) was superior to ordinary Portland cement (OPC) in boosting the photocatalytic NO_x removal activity. It was found that OPC displayed a much higher light absorption ability relative to WC. As a result, less light would be reflected to the surrounding TiO_2 surface, and thereby fewer electron-hole pairs will be generated. Even if the same amount of light does strike on the TiO_2 surface, a stronger charge transfer resistance of OPC makes the electron-hole pairs difficult to separate, and instead, more prone to recombination. These two adverse effects combine to impart an inferior photocatalytic NO_x performance to the OPC/TiO_2 mixtures. Overall, the main culprit seems to be a relative abundance of Fe_2O_3 in OPC.

As for the concrete surface layers, a simple and effective method (spray method) was developed to obtain a high photocatalytic efficiency with less amounts of nano-TiO$_2$. Its advantages over the conventional intermixing and dip-coating methods were well demonstrated. Moreover, the effects of various experimental and environmental factors on the photocatalytic NO$_x$ removal efficiency of the concrete surface layers fabricated by the new method were examined and compared with that of the samples fabricated by the intermixing method. It was found that the samples prepared by the spray method outperformed the intermix counterparts under all circumstances, demonstrating that the products produced using the new method hold great promise for practical applications in the construction sector.

PUBLICATIONS ARISING FROM THE THESIS

Guo, M.Z., Ling, T.C. and Poon, C.S. TiO_2-based self-compacting glass mortar: Comparison of photocatalytic nitrogen oxide removal and bacterial inactivation. *Building and Environment* **2012**, 53, 1-6.

Guo, M.Z., Ling, T.C. and Poon, C.S. Nano-TiO_2-based architectural mortar for NO removal and bacterial inactivation: Influence of coating and weathering conditions. *Cement and Concrete Composites* **2013**, 36, 101-108.

Guo, M.Z. and Poon, C.S. Photocatalytic NO removal of concrete surface layers intermixed with TiO_2. *Building and Environment* **2013**, 70, 102-109.

Guo, M.Z., Maury-Ramirez, A. and Poon, C.S. Versatile photocatalytic functions of self-compacting architectural glass mortars and their inter-relationship. *Materials & Design* **2015**, 88, 1260-1268.

Guo, M.Z., Maury-Ramirez, A. and Poon, C.S. Photocatalytic activities of titanium dioxide incorporated architectural mortars: Effects of weathering and activation light. *Building and Environment* **2015**, 94, 395-402.

Guo, M.Z., Maury-Ramirez, A. and Poon, C.S. Self-cleaning ability of titanium dioxide clear paint coated architectural mortar and its potential in field application. *Journal of Cleaner*

Production **2016**, 112, 3583-3588.

Guo, M.Z. and Poon, C.S. Photocatalytic NO$_x$ removal of cementitious materials: Influence of cement types and the underlying mechanisms. *Submitted to Environmental Science & Technology, under review*

Guo, M.Z., Ling, T.C. and Poon, C.S. Photocatalytic NO$_x$ degradation of concrete surface layers intermixed and spray-coated with nano-TiO$_2$: Influence of experimental factors. *Submitted to Cement and Concrete Composites, under review.*

PATENT

Poon, C.S. and Guo, M.Z. "Preparation method of photocatalytic concrete surface layers with high efficiency and robust weathering resistance", Hong Kong Patent Office (Application NO. 15110074.1)

ACKNOWLEDGEMENTS

This thesis would have been incomplete without the support of many people. First, I would like to thank my supervisor, Professor Chi Sun Poon, for granting me the opportunity to explore the fascinating area of cementitious materials. I am grateful to him for his great guidance, encouragement and support, which help me develop a wide range of skills that will benefit me in the future. He is meticulous in scientific research and kind-hearted in daily life. In my future academic career, I will follow his footsteps to be an integrity researcher.

My heartfelt thanks also go to Dr Tung-Chai Ling, Dr Anibal Maury-Ramirez and Dr Miren Etxeberria for helping me conduct various laboratory tests and giving me insightful discussions, helpful advices and inspiring ideas. Without their full support, I would not be able to put together this thesis. I am truly grateful to all of them.

I also wish to thank our laboratory technicians, Mr W. F. Tam, Mr K. H. Wong, Mr W. S. Lam and Ms Chloe Tang, for their responsive and efficient technical assistance, which greatly smoothed my experimental works. I would like to extend my thanks to Ms S. M. Lam, a former postgraduate student, H. T. Liu and P. H. Iu, two former undergraduate students, for helping me carry out tedious and time-consuming laboratory works.

I have had the tremendous pleasure of working very closely with many talented colleagues and good friends during my study at PolyU. Thanks for accompanying me through this journey of life. I will always cherish the wonderful memories we had together.

Finally, I am much indebted to my family and in particular to my wife, Dr Xiaoqing Liu, who has tolerated my long pursuit of a PhD degree with continuous encouragement and endless love. In the rest of my life, I will try my best to reward the love of my family.

Contents

List of Figures

List of Tables

ABBREVIATIONS

AOP	Advanced Oxidation Process
ASR	Alkali-Silica Reaction
BETX	Benzene, Toluene, Ethylbenzene, O-xylene
C_3A	Tricalcium Aluminate
C_4AF	Tetracalcium Aluminoferrite
CB	Conduction Band
CH	Calcium Hydroxide
CIE	Commission Internationale de I'Eclairage
C_2S	Dicalcium Silicate
C_3S	Tricalcium Silicate
CSH	Calcium Silicate Hydrate
CFU	Colony Forming Units
EDX	Energy Dispersive X-ray
EIS	Electrochemical Impedance Spectroscopy
FA	Fly Ash
ITZ	Interfacial Transition Zone
MB	Methylene Blue
MIP	Mercury Intrusion Porosimetry
MK	Metakaolin
NO	Nitric Oxide

NO_2	Nitrogen Dioxide	
NO_x	Nitrogen Oxides	
$\cdot OH$	Hydroxyl Radical	
OPC	Ordinary Portland Cement	
PCE	Perchloroethylene	
PCO	Photocatalytic Oxidation	
PL	Photoluminescence	
RG	Recycled Glass	
RH	Relative Humidity	
RhB	Rhodamine B	
ROSs	Reactive Oxygen Species	
rpm	Revolutions Per Minute	
SEM	Scanning Electron Microscope	
TCE	Trichloroethylene	
TGA	Thermal Gravimetric Analysis	
TiO_2	Titanium Dioxide	
UV	Ultraviolet	
VC	Vinyl Chloride	
VB	Valence Band	
VOCs	Volatile Organic Compounds	
w/b	Water to binder ratio	
w/c	Water to cement ratio	
WC	White Cement	
XRD	X-Ray Diffraction	

CHAPTER 1

Introduction

1.1 Background

The relentless expansion of big cities, especially metropolis, brings with it severe environmental concerns. Hong Kong is no exception. Due to the paucity of land space and a large population, Hong Kong is one of the most densely populated cities in the world. Thus, environmental problems become an especially acute issue for Hong Kong citizens. Among them, disposal of large amounts of waste glass bottles (over 100 thousand tonnes per year), produced mainly by consumption of beverage drinks, and air pollution problems, caused by a large volume of traffic vehicles, have raised the alarm to the sustainability of the society and the residents' health. Therefore, effective ways of tackling these pressing problems are badly required.

Using waste glass as a partial replacement of conventional aggregates in construction materials has become a prominent and viable route to alleviate the burden on landfills (Seung et al., 2004). The benefits of this recycling option include increased workability, enhanced resistance to chloride ion penetration and reduced drying shrinkage of cement-based materials (Topçu and Canbaz, 2004; Chen et al., 2011; Ling and Poon, 2011). On the other hand, TiO_2-mediated heterogeneous photocatalytsis has been widely considered as an advanced technique to combat air pollution problems (Guo et al., 2008). Only solar light is needed as the sole energy source to realize the photocatalytic oxidation (PCO) process, which can convert harmful pollutants into innocuous substances (Chen and Poon, 2009a). Keen interests in combining TiO_2-mediated photocatalysis with cementitious materials have

sparked extensive research on various photocatalytic cementitious materials.

The combined use of TiO_2 as photocatalyst and recycled glass as aggregate for the production of cementitious materials represents an important advancement in the construction industry. As such, it can kill two birds with one stone. On one hand, it can serve as a viable channel for recycling waste glass. On the other, it can function as an air-purifying device, effectively tackling air pollution problems plaguing people's health. Its advantages over other traditional construction materials mainly stem from the perception that it harbours an environmentally-friendly nature. In other words, the functional construction materials incorporated with recycled glass not only save natural resources but also benefit the environments.

Despite the perceived benefits of photocatalytic construction materials, their wider applications in the construction sector have been impeded by several hurdles. One is the relatively high cost due to a premium price of TiO_2 photocatalysts relative to other ingredients (Chen and Poon, 2009a). Another is the widely observed loss of photocatalytic efficiency compromised by the immobilization and encapsulation of TiO_2 particles by the hydration cement products (Rachel et al., 2002). Further studies are needed to overcome these hurdles in a bid to broaden the real-life application of photocatalytic construction materials and deepen our understanding of TiO_2-mediated photocatalysis in the cementitious system.

1.2 Research Objective and Scope

The main objective of this study is to develop photocatalytic functional cementitious materials concomitantly with a high efficiency and a low cost. Meanwhile, to assess the real-life application potential, lab-simulated weathering conditions are designed and applied to examine their long-term durability. Plus, it is expected that new insights into the attractive combination of TiO_2-mediated photocatalysis and cementitious materials will be gained. Several complementary and often synergistic objectives are as follows:

➢ Fabricate architectural mortars using TiO_2 as photocatalyst and recycled glass as aggregate in an attempt to enhance the photocatalytic efficiency and examine the effects of their incorporations on mechanical and durability properties.

➢ Evaluate the feasibility and effectiveness of applying a TiO_2 containing paint on the surface of architectural mortars as an alternative strategy to further strengthen the photocatalytic efficiency and bring down the cost.

➢ Investigate the influence of cement types on the photocatalytic activity and dissect the underlying mechanisms.

➢ Develop a simple and effective method to incorporate TiO_2 into concrete surface layers and identify both the experimental and environmental factors influencing their air-purifying performance.

➢ Examine the long-term durability of different photocatalytic functional products under various lab-simulated weathering conditions.

1.3 Thesis Organization

The remaining chapters of this thesis are organized in the following ways:

Chapter 2 reviews the principles of TiO_2-mediated photocatalysis, its advantages over traditional technologies and the factors influencing the photocatalytic reaction rate. More emphasis is placed on recent findings on the combination of TiO_2 photocatalyst with cementitious materials. Specifically, the interplay between nano-TiO_2 particles and the host cementitious materials, as well as various value-added functions with respect to diverse applications in the construction industry, is discussed in detail.

Chapter 3 gives a thorough description of the methodologies employed in this thesis.

Chapter 4 studies the combined use of TiO_2 and recycled glass to enhance the photocatalytic NO_x removal activity. Experimental results from the influence of TiO_2 dosages and recycled

glass contents on both the mechanical and durability of the architectural mortars are provided.

Chapter 5 explores the strategy of applying a TiO$_2$ containing paint on the surface of architectural mortars to augment the photocatalytic efficiency. A broad range of photocatalytic activities, including NO$_x$ and xylene removal, RhB degradation, bacteria inactivation and algae killing, are studied and compared with the 5% TiO$_2$-intermixed samples.

Chapter 6 examines the effect of cement types on the photocatalytic NO$_x$ removal behaviour. The underlying mechanisms are also dissected and discussed.

Chapter 7 develops a simple and effective way of incorporating nano-TiO$_2$ into concrete surface layers. The effects of a myriad of experimental factors, including NO flow rates, initial NO concentrations, UV light intensities, types of light source and relative humidity, on the photocatalytic NO$_x$ conversion of concrete surface layers prepared by the newly-developed method are examined and compared with the 5% TiO$_2$-intermixed samples based on two assessment approaches (NO$_x$ removal rate and NO$_x$ removal ratio).

Chapter 8 presents the results from experimental investigation on the effects of various environmental factors (dust accumulation and oil contamination) on the photocatalytic NO$_x$ conversion of two sets of samples developed in Chapter 7. In addition, the recovery of their NO$_x$ removal capacity after undergoing different cleansing processes is evaluated.

Chapter 9 summarizes the thesis and draws conclusions from the research work. Recommendations for future investigation are provided and discussed.

CHAPTER 2

Literature Review

2.1 Introduction

By any estimation, the story of titanium dioxide (TiO_2) is a scintillating chapter in the human history. It first gets involved in our daily lives as an annoying white paint. When exposed to strong sunlight, the TiO_2-based paints are prone to undergoing "chalking" (Jacobsen, 1949). A white powdery substance, similar to the chalk on a blackboard, tends to form on the paint surface. This phenomenon has been later recognized as the result of exposure of the white TiO_2 itself due to the removal of the surrounding organic ingredients (Fujishima et al., 2008). Then there came a breakthrough research in 1972. A TiO_2 anode cell was found to have the ability to simultaneously generate hydrogen and oxygen gases under ultraviolet (UV) light irradiation (Fujishima and Honda, 1972). As a concept and practice, advanced oxidation process (AOP) based on TiO_2 heterogeneous photocatalysis emerged on the global scene since then.

In the past several decades, TiO_2-mediated heterogeneous photocatalysis has received wide attention and intense research interests (Fujishima et al., 2000). Along the way, this promising technology has been successfully applied to a wide variety of areas as diverse as photocatalytic degradation of inorganic and organic pollutants in wastewaters, photocatalytic purification of air pollutants and photocatalytic destruction of microorganisms (Bhatkhande et al., 2001; Wolfrum et al., 2002; Zhao and Yang, 2003; Demeestere et al., 2007). However, its application in the field of construction and building materials emerged quite lately. By the end of the 1980s, the discovery of two TiO_2 associated effects, the self-cleaning effect and the photo-induced hydrophilicity, fuelled intensive and extensive research in the combined use of

TiO$_2$ photocatalyst with cementitious materials (Folli et al., 2012).

The aim of this review is to highlight recent findings on the combination of TiO$_2$ photocatalyst with cementitious materials and to encapsulate them in a single framework of photocatalysis related functionality. This literature review first focuses on the principles of TiO$_2$-assisted heterogeneous photocatalysis. Then, details are given on its advantages over traditional technologies and how the internal and external factors underlie photocatalytic reaction rate. Finally, more emphasis is placed on the interplay between nano-TiO$_2$ particles and their host cementitious materials, as well as the various value-added functions with respect to diverse applications in the construction industry.

2.2 TiO$_2$-Assisted Photocatalysis

2.2.1 Titanium Dioxide

Normally, photocatalysts are predominately semiconductors, such as CdS, CdSe, CdTe, ZnO, GaP, WO$_3$ and TiO$_2$. Among them, TiO$_2$ stands out as an excellent photocatalyst. So far, it has been the most widely used photocatalyst in the field of semiconductor-mediated photocatalysis because it is cost-effective, chemically inert, water insoluble, relatively safe, and most importantly, highly efficient in photocatalytic activities (Chen and Poon, 2009a).

In nature, TiO$_2$ occurs in three stable crystal structures: rutile, anatase and brookite (Fig. 2.1). The rutile phase is the most stable form, while anatase and brookite phases can irreversibly convert to the rutile phase upon heating at temperatures between 550 ℃ and 800 ℃ (Li and Ishigaki, 2004; Hanaor and Sorrell, 2011). The differences between rutile and anatase mainly derive from their density, hardness, and particularly, band gaps. Basic physical properties of the rutile and anatase type of TiO$_2$ are summarized in Table 2.1.
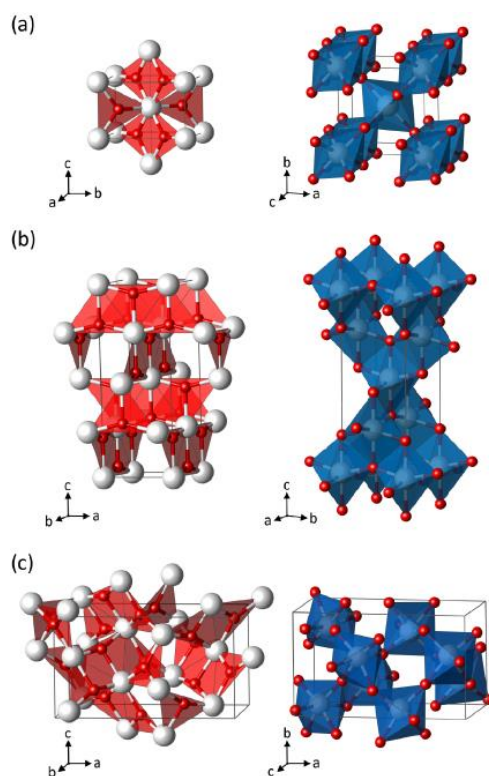
Figure 2.1 Planar Ti_3O building block representation (left) and TiO_6 polyhedra (right) for three TiO_2 crystal structures: a) rutile, b) anatase, c) brookite (Ti (white); O (red)) (Landmann et al., 2012)

Table 2.1 Basic physical properties of rutile and anatase TiO_2

Property	Rutile	Anatase
Crystal form	Tetragonal	Tetragonal
Density (g·cm^{-3})	4.23	3.87
Hardness (Mohs)	6-7	5-6
Refractive index	2.61	2.52
Band gap (eV)	3.0	3.2

2.2.2 Principles of TiO$_2$ Photocatalysis

Photocatalysis, by definition, is a typical photoreaction accelerated by the presence of a photocatalyst (Fujishima et al., 2008). To understand the underlying mechanisms of TiO_2-

mediated photocatalysis, it is helpful to get familiar with the electronic structure of semiconductors. In semiconductor associated photocatalysis, the photocatalytic efficiency relies heavily on the electronic structure of a semiconductor. Unlike conductors, semiconductors have both a valence band (VB) and a conduction band (CB), which are separated by the presence of a forbidden band. Thus, an energy gap (E_g) exists between the VB and the CB. As a result, the electrons and holes, which generally bind together in the VB, will not separate from each other without excitation. Compared with insulators, however, such an energy gap is relatively narrow and can be overcome by thermal or optical means. Fig. 2.2 gives a comparison of the electronic band structures of conductors, semiconductors and insulators.

CB
VB

(a) Metal   (b) Metal   (c) Semiconductor   (d) Insulator
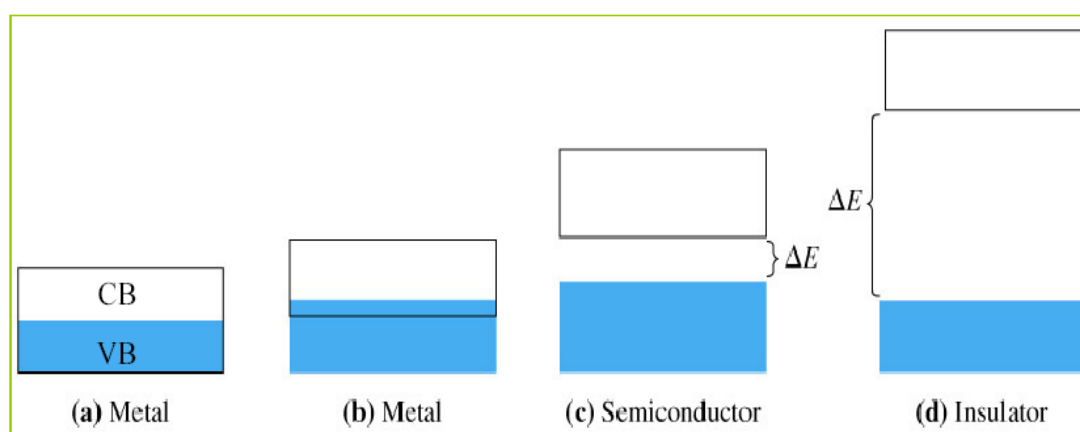
Figure 2.2 Diagram of the electronic band structure of metals, semiconductors and insulators

(Chen, 2010)

In principle, the processes of TiO_2-assisted photocatalysis can be divided into the following four main stages (Fig. 2.3):

    (a) Upon exposure to irradiation of UV light, TiO_2 can be excited by photons with energy equal to or larger than its band gap. As a consequence, electrons from the VB are promoted to the CB, leaving behind holes in the VB;

$$TiO_2 + hv \rightarrow TiO_2 + h^+ (VB) + e^- (CB)$$
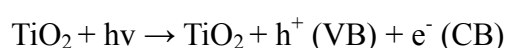
(b) The generated electron-hole pairs can separate and migrate to the TiO_2 surface, where they further react either with the absorbed water and oxygen molecules separately to form powerful oxidative and reductive species (hydroxyl radicals and superoxide ions) or directly with the absorbed substances;

$$TiO_2\ (h^+) + OH^- \rightarrow TiO_2 + OH^{\cdot}\ or\ TiO_2\ (h^+) + A \rightarrow TiO_2 + A^+$$

$$TiO_2\ (e^-) + O_2 \rightarrow TiO_2 + O_2^{\cdot-}\ or\ TiO_2\ (e^-) + B \rightarrow TiO_2 + B^-$$
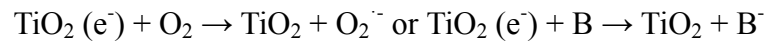
(c) These oxidative and reductive species are mainly responsible for carrying out a string of subsequent oxidation and reduction reactions with inorganic or organic matters on the surface of TiO_2;

$$OH^{\cdot} + A \rightarrow H_2O + A^+$$

$$O_2^{\cdot-} + B \rightarrow O_2 + B^-$$
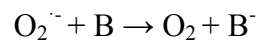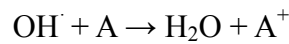
(d) Meanwhile, a portion of the generated electron-hole pairs could recombine within a very short time period, losing energy as heat.

$$h^+\ (VB) + e^-\ (CB) \rightarrow heat$$
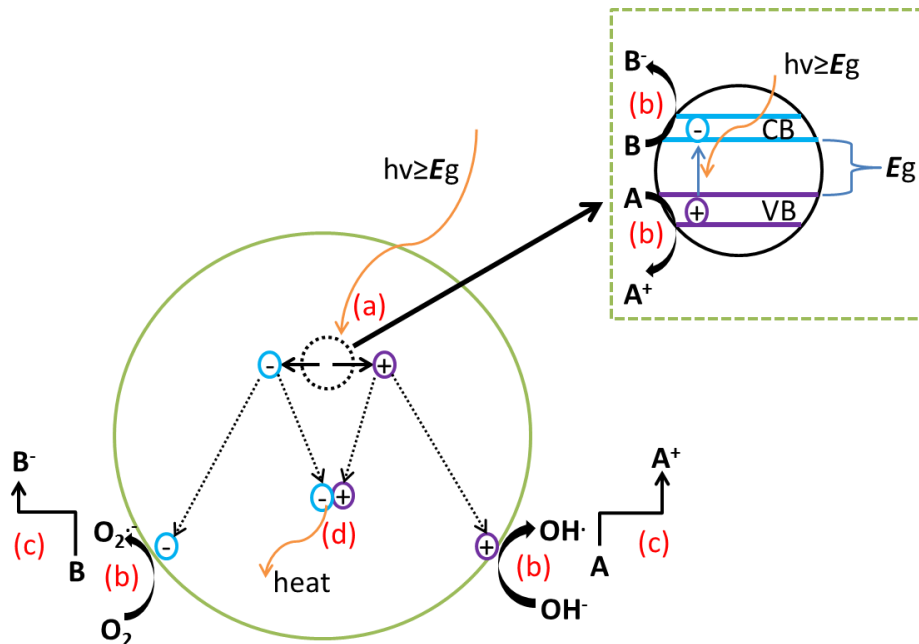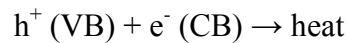
Figure 2.3 Illustration of major photocatalytic processes that occur on a TiO_2 particle upon absorption of a photon of ultra-band gap light

2.2.3 Comparison between TiO₂ Photocatalysis and Photosynthesis

As demonstrated above, all the resources required for the TiO_2 photocatalysis come from the ambient environments. Solar light (UV part), water vapour and oxygen, are all readily available and renewable. More importantly, TiO_2 photocatalyst acts only as a catalyst, which will not be consumed throughout the whole process. These features, combined with a similar energy converting process, raise a reasonable comparison between the TiO_2 heterogeneous photocatatlysis and the photosynthesis in plants.

Photocatalysis is analogous to photosynthesis in both actors and scenarios. In photosynthesis, the protagonist is undoubtedly chlorophyll, which is a powerful photocatalyst. It functions as the counterpart of TiO_2 to convert light energy from the Sun into chemical energy responsible for fuelling plants' metabolism. During the photosynthesis process, oxygen is released as a by-product with the concomitant production of carbohydrate molecules from reduction-oxidation of carbon dioxide and water. A direct comparison of the two similar phenomena is illustrated in Fig. 2.4.
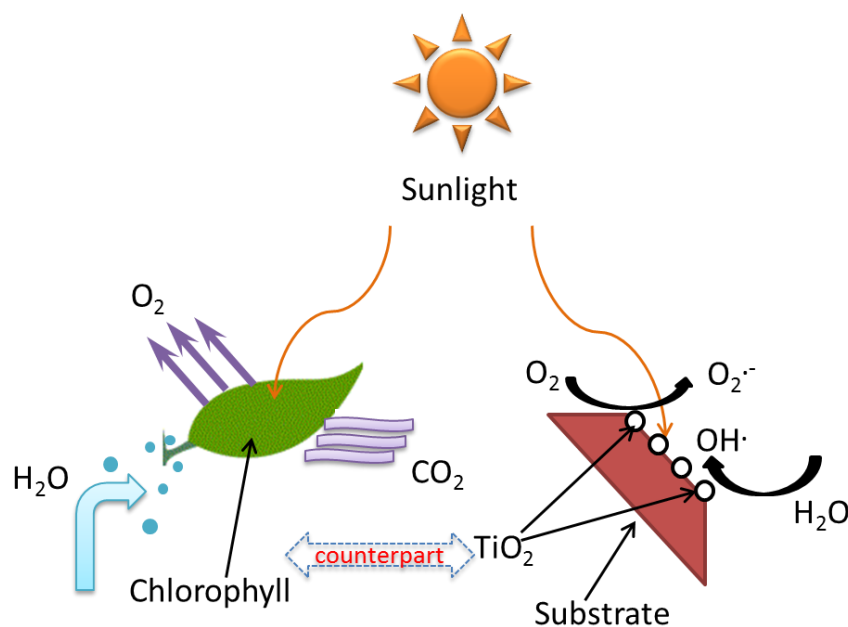
Figure 2.4 Comparison of photosynthesis in plants and photocatalysis mediated by TiO_2 under irradiation of sunlight

Such an analogous relationship between TiO_2-mediated photocatalysis and photosynthesis in plants elicits a wide variety of research on the TiO_2 photocatalysis. Indeed, research in this field has grown at an exponential rate. The focus of most research rests squarely on the employment of TiO_2-mediated photocatalysis as an environmentally friendly technology to meet clean energy demand and tackle environmental pollution.

2.3 Factors Influencing TiO_2 Photocatalysis

The process of TiO_2 photocatalysis is governed by various factors. Thus, the photocatalytic activity of a particular TiO_2 depends on a myriad of factors. These factors can be either internal or external. The fundamental difference is that internal influencing factors are inherent, and external influencing factors are derived from the surrounding environments. For example, the crystal phase, structure and morphology and particle size of TiO_2 belong to the internal influencing factors, while the temperature, light intensity and relative humidity (RH) of the ambient environments fall into the external influencing factors category. Internal influencing factors could exert their influences on the photocatalytic activity by means of altering the separation and transportation of photo-generated charges (h^+ and e^-) to the photocatalyst surface. Unlike internal influencing factors, external influencing factors determine the photoactivity by tuning the supply of ingredients for the photocatalytic reaction and by tweaking the reaction kinetic. Therefore, a better understanding of how different factors affect the photocatalytic activity will assist the design, synthesis, modification and application of TiO_2-mediated photocatalysis.

2.3.1 Internal Influencing Factors

2.3.1.1 Effects of Crystal Phase

As mentioned in the previous sector, the crystal phase of TiO_2 has a big impact on its photocatalytic performance. In nature, mainly three crystal types of TiO_2, rutile, anatase and

brookite, have been found, and their respective band gaps are 3.00 eV, 3.26 eV and 3.13 eV (Dhar et al., 2013). By far, anatase and rutile phases have garnered the most intensive research attention and play a significant role in industrial applications due to their thermodynamic stable nature, while brookite is poorly understood because it is scarce in nature and not synthetically viable (Dambournet et al., 2010; Thilagam et al., 2011). Among the three crystalline forms, anatase is the most photocatalytic effective one (Hanaor and Sorrell, 2011). This is, at least partially, attributed to its more negative redox potential of the CB. As a result, when water and oxygen molecules are adsorbed on the anatase surface, more highly reactive $^{.}OH/^{-}OH$ redox couples can be generated. However, it has been well known that a mixture of anatase and rutile (such as Degussa P25, which consists of 70-80% anatase and 20-30% rutile) is superior to its pure respective components (anatase and rutile) in terms of photocatalytic efficiency. Such an enhanced photocatalytic activity is mainly ascribed to the ease of charge separation on the surface of anatase in the presence of rutile, where the excited electrons travelling from anatase get trapped, thereby effectively repressing the recombination of charge pairs (Hurum et al., 2005; Demeestere et al., 2007; Sun et al., 2010). Therefore, TiO_2 Degussa P25 finds favour with researchers in most of the photocatalytic studies.

2.3.1.2 Effects of Structure and Morphology

The structure and morphology of titanium dioxide are intricately related to its photocatalytic activities because the stability of the TiO_2 and the charge carriers' surface or bulk recombination and surface trapping might depend on the crystalline quality and the particles shape. Also, the surface atomic configuration and the exposure degree of reactive crystal facets strictly govern adsorption and selectivity of the photocatalyst (Lee et al., 2010). Moreover, the global photocatalytic efficiency of the TiO_2 photocatalyst relies heavily on the relative reactivity of the exposed surfaces (Colbeau-Justin et al., 2003; Munirathinam et al.,

2015). Under different experimental conditions, TiO$_2$ synthesis can lead to a wide variety of morphologies as diverse as classical truncated square bipyramids, squares plates, rods, needles, cubes, belts and hollow rods (Dufour et al., 2015). Depending on equilibrium or nonequilibrium conditions, the evolution of the crystal growth will, respectively, diminish or increase the exposure of high-energy facets ({001}), ultimately developing into specific shapes with the minimum total surface free energy (Fig. 2.5) (Liu et al., 2011). A definite relationship between the photocatalytic efficiency and the morphology remains elusive due to the difficulties of obtaining well defined TiO$_2$ crystalline surface and the subsequent lack of careful description (Luan et al, 2013).
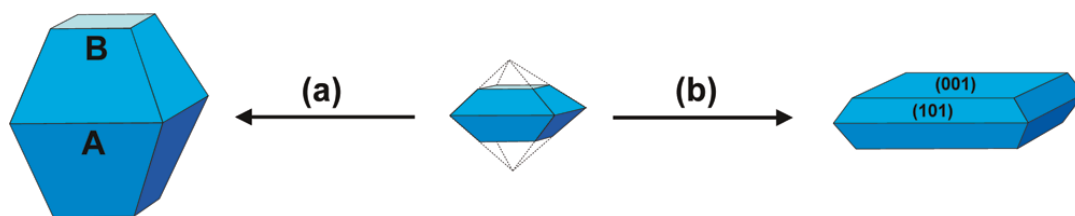
Figure 2.5 Crystal evolution of anatase TiO$_2$ nucleus (middle), typically nucleated as truncated octahedral bipyramid (TOB) seed, exposing eight {101} facets and two {001} facets. (a) Under equilibrium conditions, the high-energy {001} facets diminish quickly and the crystal spontaneously evolves into thermodynamically stable {101}-dominated TOB (left). (b) Under nonequilibrium conditions, the higher-energy {001} facets can be stabilized, typically, by selective adhesion of capping agents and the crystal growth results in a metastable {001}-dominated TOB (right). The side lengths labelled A and B are used to define the degree of truncation (B/A) and to estimate the percentage of {001} facets. (Liu et al., 2011)

However, attempts have been made to shed light on the possible correlation between different morphologies of anatase and their corresponding photocatalytic efficiency. In general, the more exposure of the high-energy facets, the higher efficiency of the photocatalysts (Zheng et al., 2009; Liu et al., 2011). A set of four finely tailored morphologies of pure anatase

nanoparticles (AµW, AGlu, ARods and ACubes) were obtained using TiO$_2$ sol-gel syntheses (Fig. 2.6) (Dufour et al., 2015).
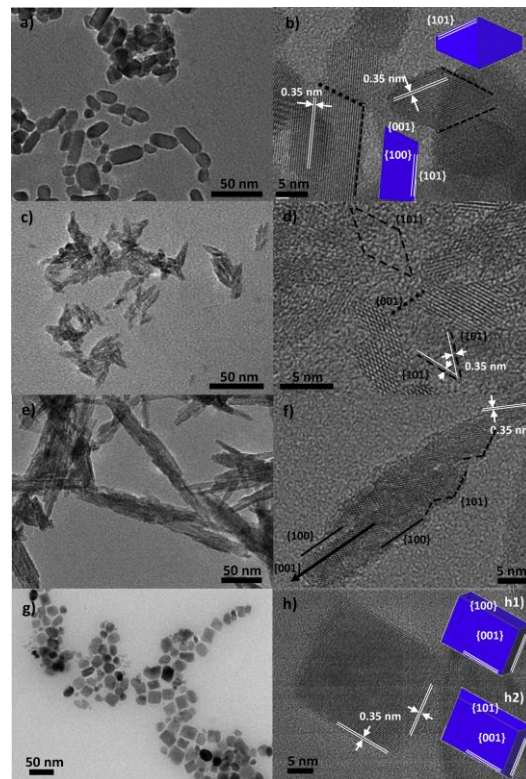
Figure 2.6 TEM and HRTEM images of (a and b) AµW, (c and d) AGlu (e and f) ARods and (g and h) ACubes samples. Measured distances between lattice fringes are attributed to the (101) anatase planes. Blue polyhedrons presented in selected HRTEM images represent 3D objects that may account for the 2D HRTEM image. Lateral faces of the particles corresponding to {100} planes are shown with plain lines, those corresponding to {100} planes are shown with dashed lines and those corresponding to {001} planes are shown with dotted lines. (Dufour et al., 2015)

The photocatalytic test demonstrated that the RhB degradation rate was in the order of AµW>AGlu>ARods>ACubes, while the time required to degrade 95% of the dye was in the order of AGlu>ARods>AµW>ACubes. Detailed analysis pinpointed a correlation between the nature of the exposed surfaces (their corresponding surface acidic behaviour) and the photocatalytic efficiency. Specifically, the AµW sample, which exposes mainly the less acidic

14

{100} faces, was inferior to the AGlu sample, which exposes predominantly the {101} ones. It seems that the anatase exposed surface may play a decisive role in determining the photocatalytic degradation of compounds that involves direct charge transfer on the adsorbed molecule. Despite such a detailed study, caution should be taken when extrapolating the conclusions to other phases of TiO_2 or different targeted pollutants. Some other studies showed that a high percentage of the {001} facet of the anatase TiO_2 contributed to an enhanced photocatalytic activity. For example, the anatase TiO_2 nanosheets with 64% and 89% of {001} facet both were superior to P25 TiO_2 (Yang et al., 2009; Han et al., 2009).

2.3.1.2 Effects of Particle Size

The particle size of the TiO_2 photocatalyst has pronounced influences on its photoactivity. Apparently, the particle size is directly related to the surface area; a decrease in one is accompanied by a corresponding increase in the other. Since the active sites of TiO_2 are highly dependent on the surface area, its photocatalytic efficiency will inextricably be affected by the particle size. In fact, it has been well demonstrated that a decrease in the particle size of TiO_2 gave rise to an increase in the photocatalytic activity. For instance, a decrease in the TiO_2 particle size resulted in an increase in the photocatalytic degradation of propyne (CH_3CCH) in water (Anpo et al., 1987). Similarly, it was observed that as the particle size of TiO_2 decreased, the adsorption rate of methylene blue (MB) on suspended TiO_2 particles increased accordingly. The increased adsorbability, in turn, led to an increase in the photocatalytic activity of TiO_2 (Xu et al., 1999).

However, the particle size does not exert its influence on the photocatalytic activity solely through changes in the surface area. Other properties of semiconductors, such as the spectral properties and the charge carrier dynamics (the dynamics of the electron/hole recombination process), are sensitive to particle size changes, especially in the nanometre range (Micic et al., 1990; Serpone et al, 1995; Zhang et al., 1998). Therefore, the photocatalytic efficiency

did not monotonically increase with decreasing particle size (Wang et al., 1997; Zhang et al., 1998). Some studies revealed the existence of an optimum particle size (Maira et al., 2000; Almquist and Biswas, 2002). It was observed that the highest photoactivity of TiO_2 (in terms of reactive oxygen species (ROSs) production per area) occurred for the particle size of 30 nm. For particle size below 30 nm, the generation of ROSs per area diminished and remained constant when the particle size was smaller than 10 nm. This observation was attributed to complex changes in defect sites on the TiO_2 surface (Jiang et al., 2008). Likewise, an optimum particle size of 11 nm was observed for chloroform degradation in water. It was assumed that the competing effects of larger surface area and higher rate of electron-hole recombination (due to the increased proximity of the charges) comes into play when the particle size decreases below a certain value (Wang et al., 2001). Similar explanations have been established to explain the existence of an optimum particle size, such as the complex interplay between surface area, light absorption and scattering efficiency and charge-carrier dynamics (Almquist and Biswas, 2002). It seems that when going from a microcrystal to a nanocrystal, the electrochemical properties are affected, thus leading to changes in light absorption and scattering ability, charge-carrier recombination activity and consequently the alternation in photocatalytic efficiency.

2.3.2 External Influencing Factors

2.3.2.1 Effects of Light Sources and Intensity

Photocatalytic reaction occurs as a result of exposure to light irradiation. Light acts as an engine driving the reaction by providing the required energy in the form of photons. Both the wavelength and intensity of light have a bearing on the photocatalytic reaction.

As aforementioned, to make the photocatalytic activity happen, the photon required should have the energy at least equal to the photocatalyst's band gap. Since all the three types of TiO_2 have a bang gap larger than 3.0 eV, the wavelength of light source has to be in the UV

region (below 400 nm) to fuel the photocatalytic activity (Choi et al., 2001). Normally, UV-A with a wavelength of 300-370 nm is predominately used as a source of light energy. However, a wide variety of light sources have been employed and proven effective in extensive studies. The routinely adopted light sources include Xenon lamps, mercury vapour lamps, Xe arc lamp, Hg-Xe lamp and black-light-type UV lamp (Zhao and Yang, 2003; Mo et al., 2009). The investigation on the photocatalytic degradation of formaldehyde over anatase TiO$_2$ films under three UV lamps (UVC, UVA black (UVA1) and UVA white (UVA2)) demonstrated that the inherent rate constant (k), which is independent of light intensity, was in the order of $k^{UVC} \gg k^{UVA1} \sim k^{UVA2}$ at low light intensity (Zhu et al., 2015). However, varying degree of photocatalytic activities can be obtained depending on the proportion of UV part in the whole spectrum of these diverse light sources and also on their respective intensity.

Generally, a positive relationship between light intensity and photocatalytic reaction rate has been observed ubiquitously (Ollis et al., 1991; Peral and Ollis, 1992; Obee and Brown, 1995; Puddu et al., 2010). The reaction rate increases proportionally with increasing the light intensity up to a certain threshold, beyond which, it increases with the square root of the intensity. However, no agreement has been established on a fixed threshold for the light intensity. For example, it was observed that below one sun equivalent (1-2 mW·cm^{-2}) of UVA light illumination, the degradation rate increases with the intensity linearly. Above one sun equivalent, whereas, the rate increases with the square root of the intensity (Ollis et al., 1991; Peral and Ollis, 1992). Similarly, when the intensity of UV light was lower than 250 W·m^{-2}, the photocatalytic reaction rate increases with the intensity in a linear manner and then shifted to a different manner of increasing with the square foot of the intensity upon irradiation by the UV light intensity above 250 W·m^{-2} (Herrmann et al., 2007). Such dependence of photocatalytic oxidation rate on the UV light intensity has been well demonstrated in the following equation (Eq. 2.1).

$r = KI^n$ (n $= 0.5,$ when: I $>$ S$_\lambda$; n $= 1,$ when I $<$ S$_\lambda$ Equation 2.1

Where K is a constant, I is the UV intensity, and S_λ is the one sum equivalent under the λ wavelength.

The related changes between the photocatalytic reaction rate and the UV intensity are mainly the manifestation of a competing effect between the electron/hole generation and recombination. Below a certain threshold of the light intensity (discussed above), increase in the electron/hole generation dominates. Above the threshold intensity, however, it shifts to the domination of the electron/hole recombination (Egerton and King, 1979; Wang and Hsieh, 1998).

2.3.2.2 Effects of Humidity

Humidity is indicative of the amount of water vapour in the air. Relative humidity (RH), which is expressed as percent, is commonly adopted to give measurements of humidity. RH is not only an environmental factor affecting the TiO_2-mediated photocatalytic reaction, but also an integral part of the reaction itself. Water vapour functions as a precursor of hydroxyl radicals (OH$^.$), which are highly reactive participants responsible for the degradation of various gaseous compounds. Therefore, the existence and changes of humidity surrounding the TiO_2 photocatalyst will inevitably cause a corresponding fluctuation in the photocatalytic reaction rate.

Since the amount of water vapour relates to the number of hydroxyl radicals in a proportional way, a higher RH generally gives rise to a higher photocatalytic activity (Boonstra and Mutsares, 1975). However, excess water vapour tends to compete with the gaseous reactants for adsorption site on the TiO_2 surface, unfavourably reducing its reactive sites. Moreover, the light blocking effect comes to dominate when water vapour exceeds a certain amount, impairing the reaction rate. In fact, the positive effect works in tandem with the negative effect to shape the overall photocatalytic reaction rate (Kim and Hong, 2002). The

observation of an optimal RH lends strong support to the above assumption (Obee and Brown, 1995; Hung and Mariñas, 1997; Demeestere et al., 2005). For example, it was found that greater conversions of chloroform were obtained in the presence of moderate concentrations of water vapour. However, further increasing humidity resulted in a decline in trichloroethylene (TCE) degradation (Hung and Mariñas, 1997). Similarly, the degradation of benzene first increased, reached a plateau and then decreased successively with increasing RH continuously (Wu et al., 2005). Moreover, positive, zero-sum and negative effects of humidity on the reaction rate of formaldehyde degradation were found under three regimes of low, medium and high humidity, respectively (Zhu et al., 2015).

However, controversy concerning the effect of humidity on the photocatalytic degradation of gas phase pollutants still remains. It has been reported that the mineralization of pesticide dichlorvos diminished significantly with increasing RH (Sleiman et al., 2008). Similarly, the NO_x removal declined as the RH was elevated (Ballari et al., 2011). On the contrary, the degradation of TCE to CO_2 increased from 53% at 0% RH to 71% at 100% RH (Oua and Lo, 2007). Apart from the aforementioned effects induced by RH, the possible accumulation of intermediates on the TiO_2 surface with respect to different reactants and the subsequent deactivation of the photocatalyst also play an important role in influencing the reaction rate (Vorontsov et al., 2001; Demeestere et al., 2005). This may partly explain the commonly observed discrepancy between different studies.

2.3.2.3 Effects of Temperature

Like humidity, temperature also has a twin effect on the photocatalytic activity, especially for the degradation of gaseous compounds. It influences both the reaction kinetic and the adsorption of gaseous compounds on the photocatalyst surface (Obee and Hay, 1997). Specifically, a positive relationship between temperature and the reaction rate is commonly observed. On the contrary, elevation in temperature leads to a reduction in the amount of

gaseous pollutants adsorbed on the photocatalyst surface. These two effects compete with each other to determine the overall photocatalytic reaction rate. This has been supported by experimental observations of the existence of an optimal temperature related to a maximum reaction rate. For example, the degradation of vapour acetone increased with increasing temperature from 30 to 77 ℃, but further temperature increase did not induce a continuous increase in the reaction rate (Zorn et al., 1999).

However, among different gaseous compounds, discrepancies have been found regarding the effect of temperature on their degradation. For instance, an increase in the degradation rate of toluene, trichloroethylene (TCE), perchloroethylene (PCE) and acetaldehyde was accompanied by an increase in temperature (Obee and Brown, 1995; Sanchez et al., 1999; Hager and Bauer, 1999). Whereas, for formaldehyde and ethylene, an opposite trend was observed (Obee and Brown, 1995; Obee and Hay, 1997). Such discrepancies may derive from the differences in the limiting factors for the photocatalytic degradation progress of different gaseous compounds. If the reaction is a kinetic limited process, the reaction rate will be promoted by increasing temperature. On the other hand, if the reaction is a mass transfer limited process, the effect on the adsorption of gaseous compounds prevails. As a result, increasing temperature will encourage the desorption of the pollutants from the surface of the photocatalyst, leading to a reduction in the reaction rate (Pichat and Herrmann, 1989).

In general, the following two equations (Eq. 2.2 and Eq. 2.3) best describe the effect of temperature on the two important processes closely related to the photocatalytic degradation of gaseous compounds. The reaction rate constant (k) followed an Arrhenius temperature dependence formula (Obee and Hay, 1997):

$$k \propto f\left(\exp\left(\frac{-E}{RT}\right)\right) \hspace{4cm} \text{Equation 2.2}$$

Where E is an apparent activation energy, T is the temperature, and R is the gas constant

$(1.99 \times 10^{-3} \text{ kcal (mol·K)}^{-1})$.

The adsorption equilibrium coefficient (K) followed a temperature dependent equation, similar to the Arrhenius one (Pichat and Herrmann, 1989):

$$K \propto f\left(\exp\left(\frac{-H}{RT}\right)/\sqrt{\text{T}}\right) \qquad\qquad \text{Equation 2.3}$$

Where H is the change of enthalpy in the adsorption of the adsorbed reactant.

2.3.2.4 Effects of Initial Reactant Concentration

The initial concentration of reactants also has significant implications for the photoreaction rate. However, the exact relationship between them still remains controversial. Some studies found that increasing inlet concentrations of gaseous pollutants was accompanied by a decline in the photocatalytic degradation rate (Duan et al., 2002; Demeestere et al., 2005; Hüsken et al., 2009). When the initial pollutant concentration was within a lower range, such influence was more remarkable. Whereas, in the range of higher concentrations, the degradation rate changed in a more relaxing way (Herrmann et al., 2007; Hüsken et al., 2009). It has been proposed that at relatively lower initial concentration levels, the reaction rate of gaseous pollutants (vinyl chloride (VC)) followed the pseudo-first order reaction rate kinetics in excess of the oxidizing species. At higher concentrations, however, the reaction kinetics changed to zero order and became less dependent on the concentration level (Mohseni and David, 2003). These observations can be attributed to the fact that at a lower range of initial pollutant concentrations, the photocatalytic reaction is not limited by the number of active sites on the TiO_2 and no competitive adsorption effect between the intermediates and the pollutant happens. On the contrary, at a higher range of concentrations, the catalyst saturation and adsorption competition become more evident (Sleiman et al., 2009).

For the gas-solid phase reaction of heterogeneous photocatalysis, the Langmuir-Hinshelwood

(L-H) model has been commonly employed to describe the kinetics (Fox and Dulay, 1993; Obee and Brown, 1995).

$$\rightarrow \frac{1}{r} = \frac{1}{kKC_o} + \frac{1}{k} \qquad\qquad\qquad \text{Equation 2.4}$$

Where r is the reaction rate, k is the apparent reaction rate constant occurring at the active site of the photocatalyst surface, K is the apparent adsorption equilibrium constant and C_o is the initial concentration of the pollutant.

The L-H model well demonstrates the dependency of the reaction rate on the initial pollutant concentration, and it has been found to be a good fitting to the experimental data in many study cases (Duan et al., 2002; Demeestere et al., 2005).

On the contrary, other studies revealed a positive relationship between the initial pollutant concentration and the corresponding degradation rate. For example, the photocatalytic degradation rate of ethylene was enhanced with increasing the inlet concentration from 10 to 260 ppmv (Obee and Hay, 1997). Similarly, increasing the concentration of serval VOCs (TCE, acetone and methanol) from 0.005 to 0.020 $mol\cdot m^{-3}$ promoted an increase in their photocatalytic degradation rate accordingly (Kim and Hong, 2002).

The existence of such discrepancies may be, at least, partially derived from the adoption of different gaseous reactants. The possible generation of various intermediates is likely to play an important role in interfering with the ongoing photocatalytic reaction, adding further layers of complexity to the already complex reaction dynamics. Therefore, care should be taken when interpreting and comparing the influence of initial gaseous pollutants.

2.3.2.5 Effects of Residence Time (Flow Rate)

Usually, the residence time of a certain gaseous pollutant is more conveniently reflected by the flow rate under various experimental conditions. A high flow rate means a short residence time of the pollutant in the experimental reactor. Generally, a positive relationship between the residence time and the degradation rate is observed. For example, it has been

demonstrated that the NO degradation rate was enhanced by a longer residence time of the NO pollutant in the reactor, while a reduced residence time coincided with a reduced reaction rate (Hüsken et al., 2009). A similar behaviour was observed for the degradation of toluene. A significant decline in the toluene conversion rate was induced by an increase in the flow rate (Jeong et al., 2005; Sleiman et al., 2009).

However, increases in the flow rate will inevitably elicit two competing effects: the reduction in residence time in the reactor and the increase in the mass transfer rate (Biard et al., 2007). When the former factor plays a dominant role, (in other words, the reaction is mass transfer limited), an increase in the flow rate will lead to an accompanying increase in the reaction rate. Whereas, if the latter factor comes into play (reaction kinetic limited), further increasing the flow rate gives rise to a reduced reaction rate (Stokke and Mazyck, 2008).

It is noteworthy that the nature of reactant and its corresponding affinity with the TiO_2 surface could also play a role in the photocatalytic reaction, which complicates the influence of the flow rate on its reaction rate. For example, the variations in the flow rate exerted a negligible influence on the conversion rate of dichlorvos but an obvious effect on the toluene degradation (Sleiman et al., 2008; Sleiman et al., 2009).

2.4 Application of TiO_2-assisted Photocatalysis in Cementitious Materials

In the past three decades, remarkable progress has been made towards the development of sustainable construction and building products. Incorporation of smart materials, such as photocatalyst, into cementitious materials represents a viable way to achieve such sustainable goals. The combination of TiO_2 with cement-based materials is rather attractive because a mutually beneficial relationship between them can be established. On one hand, the hydrated cementitious matrix acts as a safe and stable framework that hosts the foreign TiO_2 particles. On the other hand, the residing TiO_2 particles impart various value-added functions to the

host construction materials. Such mutual benefits have fuelled the interests in and facilitated the development of a wide variety of photocatalytic construction materials as diverse as paving blocks, exterior tiles, soundproof walls, tunnel walls and finishing coatings (Chen and Poon, 2009a).

2.4.1 Interplay between TiO_2 and Cementitious Materials

Introduction of TiO_2 to cementitious materials will inevitably modify the host materials' behaviour in both fresh and hardened conditions, as well as their mechanical and microstructure development, which in turn will affect the resulting photocatalytic behaviour. A better understanding of how TiO_2 particles and their host materials interact and modify each other is of vital importance to design and develop satisfactory photocatalytic cementitious materials for practical applications. Due to its simplicity, intermixing TiO_2 nanoparticles in the cement matrix is the most common method to incorporate the catalyst. Thus, discussion is confined to the interplay between the nano-TiO_2 particles (added by means of the intermixing method) and its host materials in the following sections.

2.4.1.1 Influence of TiO_2 Incorporation on Properties of Cementitious Materials

Workability One of the most recognizable influences of adding TiO_2 into the cementitious materials is a spontaneous change in the workability. In fact, the workability of cementitious materials will be reduced by the introduction of TiO_2 regardless of whether it is added as a replacement of cement or as an extra addition. It has been found that all the mixtures blended with TiO_2 nanoparticles suffered a decline in slump value, displaying non-acceptable workability (Nazari and Riahi, 2010). And with an increase in the dosage of TiO_2, there is a proportional decrease in the fluidity. For example, to achieve a similar fluidity, the superplasticizer dosage has to be increased by 16.5-23.0% and 42.0-51.2% with an increase of 2% and 5% nano-TiO_2 as compared to the plain mortar without TiO_2, respectively (Guo et al., 2012). Similarly, mortar samples (w/c=0.6) prepared by adding 1%, 3% and 5% nano-

TiO$_2$ experienced a reduction in the slump flow of 2.8%, 19.8% and 20.8%, respectively, compared with the reference sample (Zhang et al., 2015).

Since TiO$_2$ is inert and will not react with water, the widely observed reduction of workability can be mainly attributed to nano-TiO$_2$'s high specific surface area, which is significantly higher than that of the cement particles. As a result, nano-TiO$_2$ will absorb more water on the surface, reducing the amount of free water available in the mixture (Zapata et al., 2013; Mukharjee and Barai, 2014). Therefore, more water or superplasticizer is required to maintain the same level of workability of an equivalent mix without nano-TiO$_2$. Similar phenomena have been observed on other nanomaterials, such as nano-SiO$_2$ and nano-Al$_2$O$_3$, further supporting the above assumptions (Mohseni et al, 2015).

Rheology The rheological parameters, mainly yield stress and plastic viscosity, are normally reflected by different deformation rates. As mentioned above, the high surface area of nano-TiO$_2$ exerts a strong impact on the mixture, and such influence is also discernible on the rheological properties (Mohseni et al., 2015). In the fresh state, cementitious materials behave like a fluid material, where the yield stress represents the initial resistance to the flow, caused by contacts between particles, while the plastic viscosity controls the behaviour once the required torque is fulfilled to initiate the movement (De Larrard, 1999). These rheological properties of fresh cementitious materials are highly sensitive to the addition of nanomaterials. Generally, the addition of nano-TiO$_2$ leads to a considerable increase in the values of torque and yield stress, making the mixture less deformable (Senff et al., 2012). Such behaviour is particularly true for samples with a higher nano-TiO$_2$ content. And beyond a certain dosage, simply adding superplasticizer alone is not sufficient to minimize the stronger cohesive van der Waals forces of finer particles and break down the agglomerates formed. For instance, mortar samples containing 5.2% nano-TiO$_2$ and 1.3% nano-silica (by weight of cement) exhibited a noticeable reduction in fluidity and were not suitable for

measurement by rheometer due to their lower plasticity. As the mixing process proceeded up to the end of the test, the difference in the values of yield stress between the nano-TiO$_2$ containing sample and the reference became more significant (Senff et al., 2012).

The cause for this tendency might be the reduction of free water (as is the case of fluidity) available to deflocculate a larger number of finer particles. As such, the lubricant effect diminishes, and the distance between finer particles becomes increasingly closer, raising the internal cohesion of the mixture. Consequently, the three-dimensional interconnected agglomerates tend to form more frequently, along with an increase in the number of contacts between particles. The particle friction and the initial interconnected agglomeration will further increase with a higher amount of nano-TiO$_2$ added in the mixtures. Such effect ultimately manifests itself in an elevated initial resistance to deformation, i.e., yield stress (Senff et al., 2012).

Hydration Generally, nanoparticles tend to accelerate the hydration process of cementitious materials, especially during the early stages (Senff et al., 2009). Nano-TiO$_2$ is no exception. It has been extensively observed that adding nano-TiO$_2$ led to an acceleration of initial cement hydration reflected by the earlier formation of Ca(OH)$_2$ and C-S-H gel from C$_3$S phase at early curing ages (Nazari and Riahi, 2010). Moreover, adding nano-TiO$_2$ particles up to 4% (as a partial replacement of cement) accelerated C-S-H gel formation by increasing the Ca(OH)$_2$ crystalline amount during the early stage of hydration (Jalal et al., 2013). Also the setting time and the dormant period were significantly reduced in the presence of nano-TiO$_2$. For example, compared with the samples without TiO$_2$ particles, the inclusion of nano-TiO$_2$ powders not only encouraged the main peak of heat evolution to emerge earlier, but also significantly augmented its intensity and shortened its duration of occurrence. This influence became more evident and enhanced when the dosage of nano-TiO$_2$ was increased from 5% to 10% (Chen et al., 2012). Similar findings have been reported that the addition of 1%, 3% and

5% nano-TiO$_2$ shortened the initial setting time by 37.9%, 63.4% and 76.5%, respectively. Meanwhile, the corresponding reduction in the final setting time was 15.7%, 37.4% and 46.2% (Zhang et al., 2015).

It has been widely accepted that cement hydration can be considered as a dissolution and precipitation process (Hubler et al., 2011; Lothenbach et al., 2011). In the early stage of cement hydration, the fineness and specific surface area of nano-mineral admixtures play a key role in determining the dissolution rate of cement compounds. The accelerating effect of nano-TiO$_2$ on cement hydration can be ascribed to its seeding effect in the heterogeneous nucleation process (Fig. 2.7). Nano-TiO$_2$ particles could act as potential heterogeneous nucleation seeds, through which the dissolution of cement, as well as the precipitation of the hydrates, could be promoted, and the grain boundary region was densely populated with nuclei and transformed completely early in the overall process of hydration (Thomas, 2007; Lee et al., 2009; Chen et al., 2011). The high specific surface areas of nano-TiO$_2$ particles provide a string of favourable and stable nuclei whereby hydration products can grow and accumulate readily and progressively.
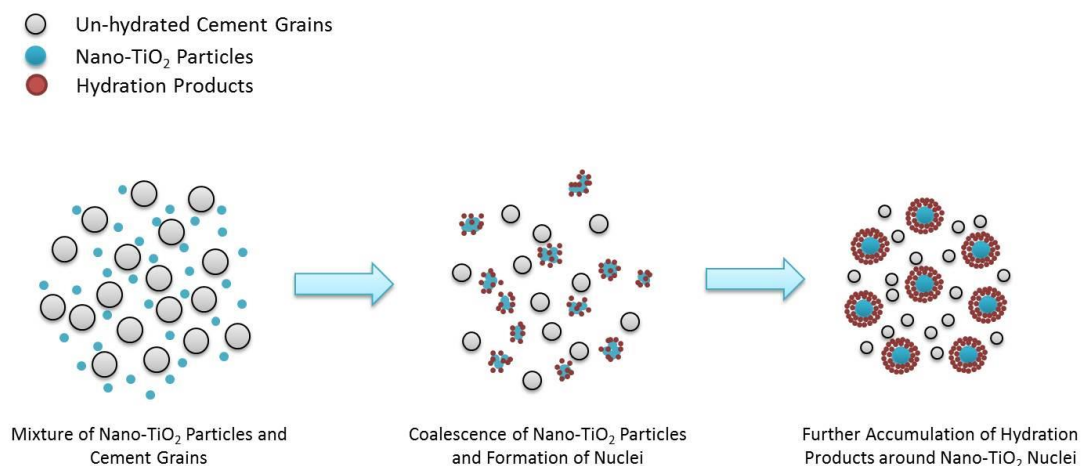
Figure 2.7 Illustration of nano-TiO$_2$ incurred nucleation effect in the cement matrix

Shrinkage The dimensional stability of hardened cement pastes can also be influenced by the inclusion of nano-TiO$_2$. This is well exemplified by the impact on the drying shrinkage of

nano-TiO$_2$ incorporated cementitious materials. It was observed that under the same curing regime, cement pastes containing TiO$_2$ nanoparticles experienced a mitigated drying shrinkage as a result of the reduced water loss (Zhang et al., 2015). Interestingly, although varying RH curing conditions did not change the trend of the drying shrinkage induced by the addition of TiO$_2$ nanoparticles, the decreasing effect was more obvious under a lower RH curing condition. For instance, in comparison with the reference samples, the TiO$_2$ incorporated cement pastes reduced the drying shrinkage by 18% and 27% under the curing RH of 90±5% and 55±5%, respectively, at a curing age of 90 d (Yang et al., 2015).

Nano-TiO$_2$ particles induced mitigation on the drying shrinkage could be closely related to the improvement in pore structures along with the increase of the hydrophilicity of the paste. As super fine powders, nano-TiO$_2$ could act as fillers to refine the pore structure (Fig. 2.8). The refining of pores can be reflected by changes in the porosity, which is a good indicator of alternations in the pore landscape. It has been found that incorporating nano-TiO$_2$ into cement pastes not only decreased the porosity, but also modified the distribution size and volume of pores (Chen et al., 2012). Increasing the dosage of nano-TiO$_2$ resulted in a corresponding decreasing trend of the accumulative pore volume (Zhang et al., 2015). Interestingly, compared with the reference sample, the nano-TiO$_2$ incorporated samples had a significantly lower proportion of pores within the mesopore range (1.25-25 nm) but a slightly higher proportion in the coarser range (larger than 25 nm), indicating that the reduction of porosity mainly occurred within the capillary pore range based on the MIP measurements. This refinement in micro structures was well mirrored by the observations of SEM morphology. The structure of nano-TiO$_2$ incorporated samples was much denser than that of the reference counterparts, reflected by shorter and more closely stacked C-S-H (Yang et al., 2015). Moreover, the width and number of micro cracks in the matrix with nano-TiO$_2$ was also significantly reduced.
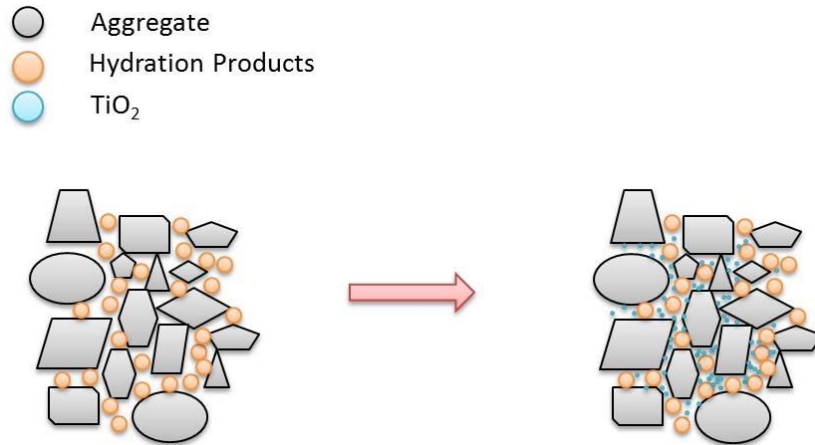
Figure 2.8 Filler effect of nano-TiO$_2$ particles in cement-based matrix

Strength The influence of nano-TiO$_2$ incorporation on the strength of cementitious materials is rather controversial. On one hand, adverse effects on the mechanical strength were observed upon replacing or adding TiO$_2$ nanoparticles in the cementitious materials. For example, bending and compressive strength tests were performed on mortar samples (w/c=0.5) which substituted standard cement with 5 and 10% TiO$_2$. After 28 days curing, mortar samples containing 10% TiO$_2$ suffered up to approximately 20% and 10% of reductions in the bending and compressive strength, respectively (Meng et al., 2012). In another separate study, compressive strength tests were performed on concrete samples (w/c=0.69 and 0.52) which contained TiO$_2$ in concentrations ranging from 0 to 5 %. Reductions about 4 and 9% in compressive strengths were observed in concrete samples (w/c=0.52) added with 2.5 and 5% TiO$_2$, respectively, in comparison with the reference samples (Diamanti et al., 2013). Furthermore, the compressive and flexural strengths of mortar samples prepared with a mixture of lime, OPC and gypsum decreased by increasing the amount of TiO$_2$ (Lucas et al., 2013).

On the other hand, extensive studies revealed that the mechanical properties were improved by adding TiO$_2$ nanoparticles (Nazari, 2011). Compressive strength tests performed after three weeks on three different white Portland cement pastes (w/c=0.5) which contained 10%

TiO$_2$ showed an increase of up to 20% in the compressive strength (Lackhoff et al., 2003). Similarly, compressive strength tests performed on mortar samples (w/c=0.485) added with 5 and 10% TiO$_2$ indicated that the compressive strength of all mortars was improved at all ages (Chen et al., 2012). However, although compressive, splitting tensile and flexural strength tests showed improvements with increasing TiO$_2$ content up to 5% in self-compacting concrete samples, the best case was observed for samples containing 4% TiO$_2$. The reduced compressive strength when high dosages (> 4%) of TiO$_2$ were used might be due to the fact that the quantity of TiO$_2$ present in the mix was higher than the amount required to combine with the liberated lime during the hydration process. Also, it might be due to the defects generated during the dispersion of the nanoparticles that caused weak zones (Nazari and Riahi, 2010).

It seems that the dispersion of nano-TiO$_2$ in the cement-based matrix holds the key to determining whether a positive or negative effect will ensue. The adverse effect on the mechanical strength with the addition of nano-TiO$_2$ is usually attributed to the difficulty in dispersion of the nano-materials in the mixtures of cementitious materials (Rao et al., 2015). However, if well dispersed, nano-TiO$_2$ will generally, if not always, generate an amelioration of the strength, which is believed to be a combined result of the seeding and filler effects (Senff et al., 2012; Zhang et al., 2015). Therefore, caution should be taken when it comes to the effect of incorporation of nano-TiO$_2$ on the ultimate strength of cementitious materials.

2.4.1.2 Influence of Properties of Cementitious Materials on TiO$_2$ Photocatalytic Performance

Effects of Curing Age The photocatalytic efficiency of cement-based products containing TiO$_2$, especially those intermixed with TiO$_2$ particles, is highly dependent on the curing age. In general, a negative relationship between the curing age and the corresponding photocatalytic efficiency has been established (Poon and Cheung, 2006). In other words, the older the specimen, the lower its relevant photocatalytic activity is. For example, the

photocatalytic atrazine degradation rate of hardened cement pastes declined with increasing the curing age (Lackhoff et al., 2003). Consistent with this finding, it has been found that in comparison with samples at a 7-day curing age, the concrete surface layers cured at 28 days and 56 days suffered an average loss of 7.7% and 21.1% in the photocatalytic NO_x removal ability, respectively (Chen and Poon, 2009b).

The loss of photocatalytic activity with increasing the curing age could be related to the changes in microstructures. As cement-based materials undergo a longer curing age, a denser gel structure evolves due to the filling of available voids by hydration products (Brandt, 2009). Consequently, the incremental pore volume and the total porosity of cementitious materials will decrease progressively (Espinosa and Franke, 2006). This will unfavourably reduce the amount of lights that will otherwise be able to travel through the pores and ultimately reach the surface of the embedded TiO_2 particles. Since the photocatalytic efficiency of TiO_2 relies heavily on the access to the light irradiation, blocking of the light transmission pathway adversely affects the resulting photocatalytic activity. On the other hand, the evolvement and accumulation of more hydration products inevitably wrap up and encapsulate some of TiO_2 particles, thereby contributing to additional losses in the overall photocatalytic activity (Fig. 2.9).
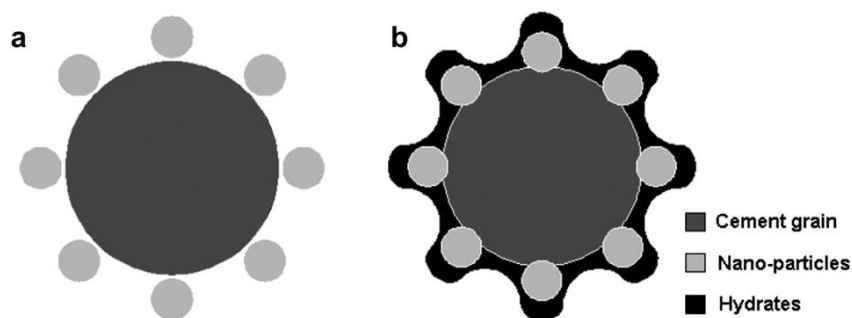
Figure 2.9 Illustration of encapsulation of TiO_2 nanoparticles in the cement matrix by

hydration products (Chen et al., 2011)

Effects of Aggregate Type In most cases, aggregate presents in cement-base matrix as an

inert substance. Thus, its influence on the photocatalytic activity is mainly derived from its physical properties. Among various physical properties, the light transmitting ability of aggregate plays a decisive role. On this basis, glass aggregate is superior to other types of aggregate in boosting the photocatalytic activity of TiO_2 incorporated cementitious materials. It has been found that using recycled glass as a replacement of river sand led to an enhanced photocatalytic NO removal performance. With a higher replacement percentage by glass cullets, there was an increasing trend in the amount of NO removed. When the river sand was completely replaced by the glass cullets, the corresponding photocatalytic NO removal efficiency increased by almost 200% in the best-case scenario (Chen and Poon, 2009b). Apparently, the light-transmitting nature of glass aggregate not only allows the irradiation light to penetrate into a greater depth to activate more TiO_2 particles residing in the inner part of the host materials, but also reflects a considerable amount of light to the surface of those TiO_2 particles on their top surface (Fig. 2.10). This assumption is further supported by the observation that a strong correlation existed between the UV absorption of different coloured glass aggregates and their respective photocatalytic activity. For instance, samples containing the brown glass aggregate, which has the highest UV absorbance, displayed the lowest NO removal efficiency. In contrast, its counterpart with clear glass aggregate possessed a much higher NO removal ability (Guo and Poon, 2013).
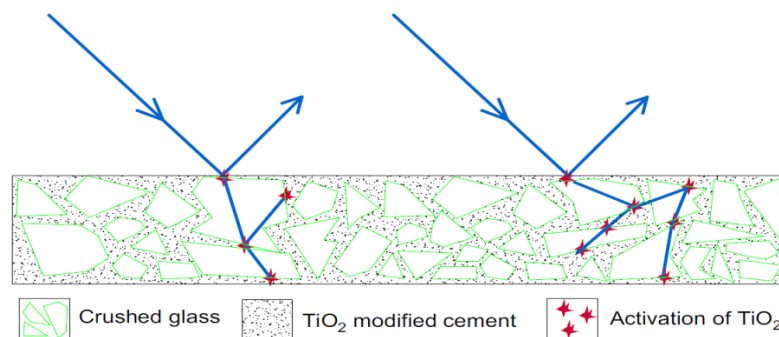
Figure 2.10 Pathways of light and activation of TiO_2 in block surface layer using glass as aggregates (Chen and Poon, 2009b)

32

Effects of Cement Type As mentioned earlier, Portland cement is by far the most widely used cement in the world. Although their ingredients may vary considerably depending on places where the raw materials are sourced, they commonly bear a grey colour due to the presence of iron and other transition metals. In stark contrast, the lack of these metals in white cement renders it a white colour. Such a difference between grey coloured Portland cement and white coloured white cement corresponds to an accompanying difference in the photocatalytic efficiency of their respective TiO_2 incorporated products. Generally, the combination of white cement and TiO_2 gives rise to a higher photocatalytic efficiency than the equivalent of Portland cement and TiO_2. For instance, white cement concrete with 5% TiO_2 (by weight of cement) outperformed Portland cement concrete with the same amount of TiO_2 in photocatalytic degradation of phenanthroquinone dye (Cassar et al., 2003). Similarly, white cement pastes with either 5% or 10% TiO_2 content (by weight of cement) delivered a higher NO_x removal activity than their OPC counterparts regardless of curing ages (Chen and Poon, 2009c). Another important observation revealed that mortars produced by dark cement (iron-rich cement: 17 wt.% content in Fe_2O_3) were dwarfed by those produced by white cement (an iron-lean cement: 0.1 wt.% content in Fe_2O_3) in terms of photocatalytic NO_x removal (Pérez-Nicolás et al., 2015).

The exact reason behind this phenomenon remains unclear. But it has been postulated that the existence of ion and transition metals that distinguish white cement from Portland cement might be responsible for the observed difference in the photocatalytic performance. They may interfere with the light absorption and electron-hole separation process in a negative way. It is highly likely that iron oxide and transition metals in Portland cement will compete with the TiO_2 particles for the incident photons from light sources, thus reducing the amount of light that will otherwise be utilized by TiO_2 to realize the photocatalytic activity. It is also possible that the separation of electron-hole pairs will be adversely inhibited by the transition metals

(Chen and Poon, 2009c). However, solid experimental evidence is much needed to give a better and deep understanding of how key ingredients in different types of cements influence the photocatalytic activity.

Effects of Carbonation When cement-based materials are exposed to the atmospheric environments, they will undergo a slow process of carbonation upon absorption of CO_2 from the surrounding air. This can exert an inevitable influence on the photocatalytic functions of TiO_2 incorporated cementitious materials by altering their mechanical properties. Typically, carbonation due to cement ageing has a detrimental effect on the photocatalytic activity of various cementitious materials prepared with the TiO_2 addition. It has been well demonstrated that increased carbonation of cement (reflected by decreasing pH values) led to a significant reduction in the atrazine degradation (Lackhoff et al., 2003). Consistent with this finding, a 12% loss of photocatalytic NO_x removal ability was observed on cement pastes exposed to accelerated carbonation in comparison with the reference samples without carbonation. Furthermore, there was a decreasing trend with increasing the duration of carbonation (Chen et al., 2009).

The carbonation incurred loss in the photocatalytic capacity is associated with the alternations in the mechanical properties of the cementitious materials. It has long been known that carbonation can not only cause a reduction in the specific surface area, but also reduce the porosity of cementitious materials (Johannesson and Utgenannt, 2001). This is mainly due to an increase in volume with the conversion of $Ca(OH)_2$ to $CaCO_3$ through the carbonation process. Another factor at play may be the reduced sorptivity caused by carbonation, which unfavourably results in smaller amounts of adsorbed gaseous pollutants (Dias, 2000).

2.4.2 Versatile Photocatalytic Functions and Their Applications

The diverse photocatalytic-related functions rendered by inclusion of TiO_2 photocatalysts in cementitious materials are the linchpin of the corresponding real-life applications. These

attractive photocatalytic functions mainly include self-cleaning ability, air-purifying activity, anti-bacterial capacity and anti-fouling property (Fig. 2.11). In the following sections, the development of fundamental laboratory investigations on each of these aspects and the real-life applications of TiO_2-based construction materials are reviewed and discussed extensively.
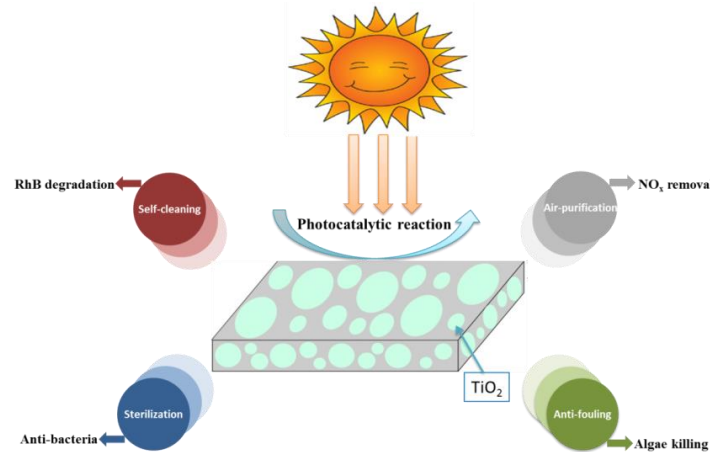
Figure 2.11 Versatile photocatalytic functions of TiO_2 incorporated cementitious materials

2.4.2.1 Self-Cleaning Ability

Principle The synergy of two properties associated with the TiO_2 photocatalyst allows the self-cleaning activity to happen. One is the redox reaction promoted by the TiO_2 upon light activation, and the other is the photo-induced super-hydrophilicity. The principles of the former property have been discussed in detail in the previous section. The latter property can be explained by the processes illustrated in Fig. 2.12.
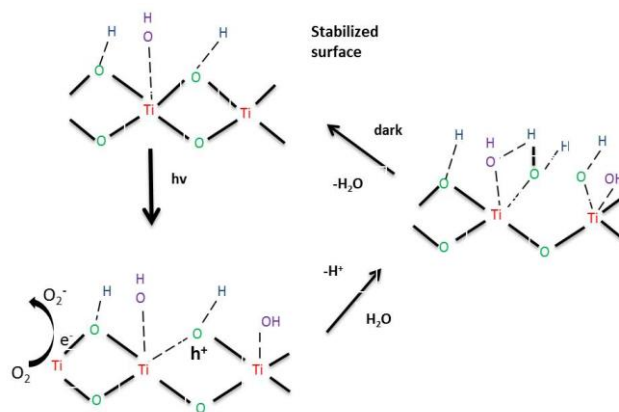
Figure 2.12 Illustration of photo-induced hydrophilic TiO_2 surface (Hashimoto et al., 2005)

It has been perceived that the photo-generated holes are mainly responsible for the highly hydrophilic conversion. Under UV irradiation, the generated holes in the bulk of TiO_2 will diffuse to the surface and be trapped at lattice oxygen sites. Although most of these holes participate in the redox reaction, a small portion may react with TiO_2 itself. With the help of water molecules at the titanium site, the bond between Ti atom and the lattice oxygen atom can be broken. Subsequently, the coordinated water molecules release a proton for charge compensation along with the formation of a new OH group. Since the surface energy of the TiO_2 surface covered with the thermodynamically less stable OH groups is higher than that of the TiO_2 surface covered with the initial OH groups, water droplet is more prone to flatting out rather than beading up on such a surface (Hashimoto et al., 2005). It should be pointed out that this photo-induced hydrophilicity can be reversed in the dark. In the self-cleaning process, the photo-induced super-hydrophilicity and photocatalytic redox reaction take place simultaneously.

Laboratory Investigation Laboratory experiments on the self-cleaning capacity of TiO_2-incorporated cementitious materials have been carried out in an extensive manner. In most cases, white cement is the favoured matrix provider due to its aesthetic-pleasing appearance, for which a self-cleaning ability is more desirable. In real atmospheric environments, dirt, grease and various organic contaminants are all the targets of the self-cleaning activity. However, for simplicity purposes, in the laboratory investigation organic dyes have been widely employed as model and proxy contaminants to evaluate the potential and ability of various TiO_2-based cementitious materials. Among them, RhB is the predominant target used in the laboratory experiments (Krishnan et al., 2013a). Specific colorimetric tests have been developed to assess the efficiency of the dye degradation and subsequent initial colour recovering (Srivastava et al., 2015). The colorimetric measurement is based on the parameter a^* from the colour system CIE (Commission Internationale de I'Eclairage) $L^*a^*b^*$. This

system decomposes any colour measurement in three coordinates: (L^*) plots the lightness with values between white and black, (a^*) represents values between red and green, while (b^*) does the same with values between blue and yellow (Fig. 2.13).
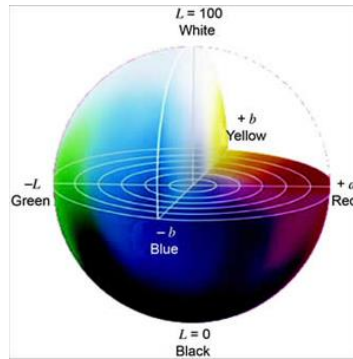
Figure 2.13 CIE $L^*a^*b^*$ system (Shevell, 2003)

For instance, the self-cleaning ability of two cementitious products, a 10 mm thick rendering and a 1 mm thick mineral paint (both containing nano-sized TiO_2), was examined by monitoring the photocatalytic degradation of RhB. It was observed that after undergoing less than a day of artificial sunlight irradiation, all the samples restored approximately 65% of their initial colour (Vallee et al., 2004). This finding was mirrored by a later study on TiO_2-based white mortar cubes impregnated with RhB. The TiO_2 induced self-cleaning activity allowed the RhB contaminated white mortar cubes to recover around 75-95% of their initial colour after exposure to 24 hours of "daylight lamp" irradiation (Dienemann, 2006). More recently, it has been observed that TiO_2-modified self-compacting mortars were effective in the discolouration of RhB under both UV and strong halogen light irradiation. During the course of first 2 h of UV light irradiation, the discoloration rate was almost constant for all the TiO_2 incorporated samples regardless of the TiO_2 content (Chen et al., 2011).

Real-life Application In real-life service, most of the construction materials are constantly exposed to the atmospheric environments. Inevitably, greasy and sticky deposits from the ambient air, especially the highly polluted urban air, tend to adhere to and accumulate on the surface of buildings. The aesthetic appearance of these affected buildings will be impaired

gradually with time. This necessitates routine maintenance, dramatically increasing the cost in labour. Given the attractive self-cleaning ability of TiO_2-based cementitious materials, it is expected that the practical application of such products will significantly reduce the cost of maintenance in an environmentally-friendly way.

On the other hand, the promising experimental results on the self-cleaning ability of a myriad of TiO_2-based cementitious materials on the laboratory scale have laid a solid foundation for practical applications in the field of construction and environment. The first real-life application of self-cleaning cementitious materials was realized in Rome in 2003 (Pacheco-Torgal and Jalali, 2011). The church "Dives in Misericordia", which is consisted of 346 prestressed concrete blocks, was manufactured mainly using white cement and TiO_2 photocatalysts (Fig. 2.14). It has been demonstrated to possess the ability to restore the colour of the white cement within 8 h of photocatalytic degradation of the dye. More importantly, during its service life (at least in the first 6 years), it was found that there was only a slight difference between the internal and external lightness, demonstrating a good capability of maintaining the aesthetic appearance with the assistance of solar light irradiation (Chen and Poon, 2009a). Other relevant examples are Music and Art City Hall in Chambery and Air France building in France, Saint John's Court in Montecarlo and GRC building in Milan (Guerrini and Corazza, 2008; Srivastava et al., 2015).

Figure 2.14 Church "Dives in Misericordia", Rome, Italy. (Cassar et al., 2003)

2.4.2.2 Air-Purifying Activity

Principle Unlike the self-cleaning process, the photocatalytic degradation and conversion of a wide variety of air pollutants, mainly NO_x and VOCs from traffic emissions, relies solely on the photon-induced redox reaction. In the case of NO degradation, the UV induced holes and subsequent active derivatives, such as superoxide anion and hydroxyl radicals, are able to oxide NO firstly to NO_2 and then to HNO_3 (Dalton et al., 2002).

$$NO + HO_2^{\bullet} \rightarrow NO_2 + OH^{\bullet}$$

$$NO_2 + OH^{\bullet} \rightarrow HNO_3$$
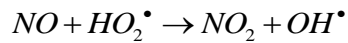
However, the photocatalytic oxidation (PCO) of VOCs is a more complex process. A much higher photocatalytic activity is required. In other words, a successful NO conversion activity does not necessarily always translate into guaranteed degradation of VOCs. This is understandable given that the structures of VOCs are more intricate. Moreover, the generation of various intermediates further complicates the whole POC process (Gunschera et al., 2009). Nevertheless, if the PCO of the VOC pollutants goes completely, the final degradation products should be the harmless CO_2 and H_2O (Chen et al., 2011).
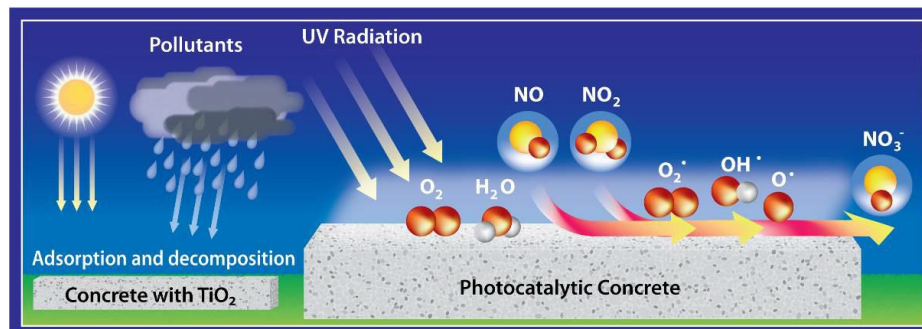
Figure 2.15 Illustration of the air-purifying process of photocatalytic building materials

(Boonen and Beeldens, 2014)

Throughout the course of PCO, only solar light (the UV part) is needed to degrade a wide range of gaseous pollutants on the surface of various construction materials. The depolluted contaminants will precipitate on the surface of photocatalytic active cementitious materials.

And ultimately, the decomposed air contaminants will be washed away by rain (Fig. 2.15).

Laboratory Investigation This aspect of research on various TiO_2 incorporated cementitious materials has by far received the most attention. It is understandable considering that most of the cementitious materials are commonly and constantly exposed to the atmospheric environments where intimate contacts with air pollutants are frequent. The laboratory investigation on the depollution efficiency of photocatalytic cementitious materials has been conducted using different test methods (Krishnan et al., 2013b). Among them, the flow-through method developed in accordance with ISO 22197, which simulates the air flow scenario in a real atmospheric condition, has been predominantly employed (Fig. 2.16).
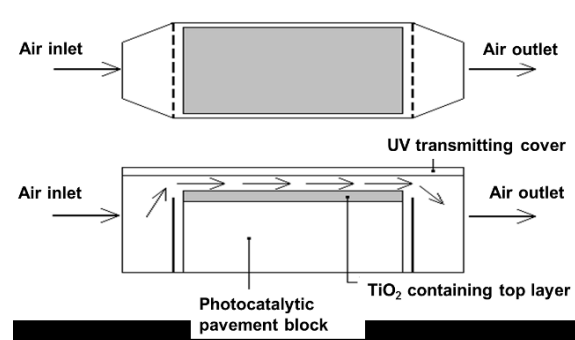
Figure 2.16 Schematic diagram of photocatalytic air-purifying test set-up based on ISO 22197-1:2007 (Boonen and Beeldens, 2014)

It has been well demonstrated that synergetic effects on the photocatalytic NO_x removal induced by the combination of TiO_2 and cementitious materials were observed. Clearly, the efficiency of NO_x removal by the TiO_2/cementitious materials dwarfed that of other tested materials (the photocatalyst alone or any other combination) (Cassar, 2004). However, not all the TiO_2-based cementitious materials are capable of removing NO_x. Under an optimum laboratory condition, a comparative study on the photocatalytic NO_x removal ability of different photocatalytic cementitious materials revealed that the NO_x degradation efficiency varied significantly with respect to different products. Some can remove as high as 40% of NO_x, while others possessed no NO_x removal effect (Hüsken et al., 2007). But later studies

showed that both TiO_2 incorporated paving blocks and architectural mortars were able to deliver a satisfactory NO_x removal activity. For example, the concrete surface layer of paving blocks containing 5% TiO_2 (by weight of binder) displayed a NO_x removal efficiency of 100 $\mu mol \cdot m^{-2} \cdot h^{-1}$, while the architectural mortar samples with the same amount of TiO_2 possessed a capacity of about 80 $\mu mol \cdot m^{-2} \cdot h^{-1}$ (Chen and Poon, 2009b; Chen et al., 2011).

The photocatalytic degradation of VOCs by TiO_2-based cementitious materials has also been investigated. Aromatic hydrocarbons, such as benzene, toluene, ethylbenzene and xylene (BTEX), are commonly employed as representative VOCs in the laboratory experiments. For example, the photocatalytic degradation of BTEX was investigated using white cement samples incorporated with 0.5, 1, 3 and 6% of nano-TiO_2 powders on a weight basis. It was found that the photocatalytic degradation efficiency of o-xylene was the highest, while benzene was the most recalcitrant to be degraded. Moreover, there was a linear relationship between the photocatalytic degradation rate of BTEX and the concentration of the reactant and also the irradiation intensity (Strini et al., 2005). Under some optimal conditions, the photocatalytic toluene removal rate of TiO_2 imbedded roofing tiles and corrugated sheets exceeded 100 $mg \cdot m^{-2} \cdot h^{-1}$ (Demeestere et al., 2008). However, a later study demonstrated that self-compacting architectural mortars intermixed with 5% TiO_2 (by weight of cement) failed to deliver any discernible toluene removal activity (Chen et al., 2011). The sporadically observed discrepancies between different studies highlighted the complicated degradation processes of VOCs and also pointed out the difficulty of extrapolating results from one study to another similar one due to the inevitable variations in the experimental conditions adopted.

Real-life Application Air pollution has increasingly become a pressing problem in big cities, especially the densely populated metropolis. High concentrations of air pollutants derived from the exhaust of a large number of vehicles pose a great threat to the health of urban people. Buildings and pavement blocks are normally adjacent to the pollution sources. Thus,

imparting the air-purifying ability to these cementitious materials offers a convenient and attractive option to combat and tackle the air pollution problem in a sustainable fashion. And encouraging laboratory results propel the extension of photocatalytic cementitious materials to real-life applications.

Figure 2.17 Separate parking lanes with photocatalytic pavement blocks at the Leien – Antwerp, Belgium (Boonen and Beeldens, 2014)

In Europe, several pilot projects have been implemented in real conditions. During 2004-2005, a section of 10,000 m^2 of the parking lanes of a main axe in Antwerp was paved with photocatalytic pavements (Fig. 2.17). Anatase TiO_2 was mixed in the mass of the upper layer (5-6 mm) of the pavement blocks. Both lab tests and on-site measurements were carried out to monitor the efficacy and durability of these photocatalytic pavement blocks. Satisfactory durability was confirmed by measuring the photocatalytic NO_x removal ability of the applied pavement blocks in the laboratory after different periods of exposure. Although the accumulation of pollutants on the block's surface reduced the NO_x removal efficiency, washing the surface by water was able to restore the initial NO_x removal ability (Beeldens, 2007). Even with a service life of more than five years, these pavements can still maintain their photocatalytic efficiency (Beeldens and Boonen, 2011). Despite the difficulty of field measurements due to the unpredictable fluctuations of the neighbouring traffic, wind speed and relative humidity, preliminary on-site measurements gave an indication of efficacy of the photocatalytic pavements reflected by a decrease in the peak NO_x concentration at the sites of these photocatalytic pavements (Beeldens, 2008). Similar demonstrations were also obtained

in another pilot project running in Bergamo, Italy (Guerrini and Peccati, 2007).

In the past decade, the "photo-road" technology has also been developed and applied in a wide range of pilot projects in Japan. One of such applications was on the 7th belt highway in Tokyo (Fig. 2.18). An area of nearly 300 m^2 was covered by cement mixtures containing TiO_2 colloidal solutions. Approximately 50-60 mg·day^{-1} NO was estimated to be removed from the whole photocatalytic active area, which equates to the amount of NO emitted from about 1000 automobiles (Fujishima et al., 2008; Pacheco-Torgal and Jalali, 2011).

Figure 2.18 Application of TiO_2 photocatalytic materials on roadway for pollution reduction

(Fujishima et al., 2008)

More recently, the European Life+ Project PhotoPAQ was a campaign launched to demonstrate the potential of photocatalytic construction materials for air purification purposes in an urban environment. The air-purifying capability of TiO_2 containing photocatalytic cementitious coating materials were applied on the wall surface of the tunnel Leopold II (Fig. 2.19). A dedicated UV lighting system was installed inside the tunnel to activate the photocatalytic active products. During the field campaign, the photocatalytic degradation of these cementitious coating inside the tunnel on various air pollutants (such as NO_x, VOCs, particulate matter and CO) was carefully monitored. Unexpectedly, no observable reduction in air pollutants was observed. For example, the NO_x reduction efficacy was less than 2%, which was in stark contrast to the laboratory results. The deactivation of such photocatalytic cementitious coatings in the heavily polluted Leopold II tunnel due to a

large volume of traffics contributed to the failure to degrade air pollutants. Also, the normally high wind speed (up to 3 m·s^{-1}) inside the tunnel unfavourably reduced the contact time between the coatings and the pollutants, further exacerbating the decline in the photocatalytic performance (Gallus et al., 2015).

Figure 2.19 Application of the photocatalytic product and installation of the UV lamps in the Leopold II tunnel in Brussels (Boonen and Beeldens, 2014)

It seems that it is a totally different story when it comes to the real-life application of the TiO$_2$-based cementitious materials. Their photocatalytic efficacy and durability are influenced by a broad range of environmental factors, which change constantly. Thus, the evaluation of the real-time photocatalytic depollution efficiency is rather challenging. Moreover, deactivation of the photocatalytic cementitious materials in the atmospheric conditions happens due to the accumulation of reactants on the surface. Rejuvenation of the original photocatalytic activity relies heavily on the wash-away of the reactants and constant solar light irradiation. This may partly explains why the deactivation of the TiO$_2$ containing cementitious coating in the tunnel almost completely eliminated their photocatalytic activity.

2.4.2.3 Anti-Bacteria Capacity

Principle Different microbiological aspects made the disinfection kinetics of the photocatalytic bacteria killing process more complex than that usually observed for the oxidation of chemical pollutants (Marugán et al., 2010). Chemical activity is not directly comparable to biological activity given that decolouring the dye only needs relatively minor

modifications, and microorganism inactivation is a rather more complex process requiring a certain amount of reactive oxygen species (ROS) accumulation and involving much more radicals (Marugán et al., 2008). Thanks to extensive efforts devoted to elaborating the killing mechanisms of bacteria, it has been generally accepted that the abatement of bacteria may be a complicated process, involving oxidative damage of cell walls, membranes, enzymes and nucleic acids by the ROS and their stable products (Fig. 2.20) (Rincón and Pulgarin, 2007). In general, the photocatalytic bactericidal process begins with the accumulation of TiO_2 photocatalysis induced ROS on the bacterial cell wall, followed by the initial oxidative damage to the cell wall. After that, the oxidative damage continues to destroy the underlying cytoplasmic membrane, which gives rise to a high permeability. This enables intracellular contents to flow freely and thereby allows ROS to easily penetrate membrane-damaged cells. Subsequently, intracellular components, such as enzymes, amino acids and nucleic acids, are severely damaged. Finally, this process concludes with the death of bacterial cells (Huang et al., 2000; Lan et al., 2007; Benabbou et al., 2007).
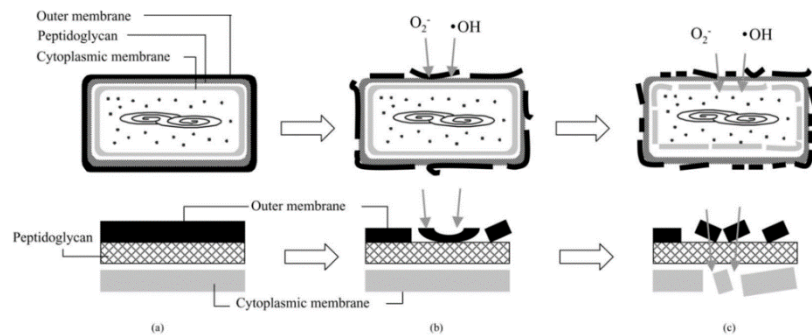
Figure 2.20 Schematic illustration of the process of *E. coli* photo-killing (Sunada et al, 2003)

Laboratory Investigation Until now, there is rather limited research work on the photocatalytic bacteria inactivation of TiO_2-based cementitious materials. One reason is that most of the cement-based materials have porous structures, which will trap the bacteria, applied on their surface, in the pores. This makes the washing out of bacteria from the samples in the immediate wake of tests extremely challenging. In this regard, the scarcely

carried out tests on the bactericidal activity were mainly done on cementitious materials with a dense structure, such as self-compacting mortars and ceramics. Studies revealed that 5% TiO_2-intermixed self-compacting architectural mortars had a negligible bactericidal ability despite possessing a good NO removal ability (Guo et al., 2012). In contrast, TiO_2-dip-coated samples displayed a satisfactory bactericidal ability, killing all the bacteria applied on their surface within 2 h (Guo et al., 2013). These studies clearly demonstrated that photocatalytic air-purifying activities were not directly related to photocatalytic bacteria killing behaviours, with the latter being a process involved complicated interplay between oxidation radicals (ROS) and various organic matters (the components of cell wall, membranes and enzymes).

Real-life Application There is growing interest in applying bactericidal cementitious materials in microbiologically sensitive environments, especially hospitals, kindergarten and elder care facilities, where bacteria and viruses contamination is undesirable and will have catastrophic consequences. The photocatalytic sterilizing cementitious materials hold great advantages over conventional chemical agents. Only light and oxygen are required to realize their sterilizing functions. More attractively, the TiO_2 incorporated surfaces of these cementitious materials are non-toxic, dispelling the concerns of causing environmental contamination (Fujishima et al., 2008).

A type of antibacterial tile has been successfully developed by coating ordinary tiles with TiO_2-Cu composites and installed on the floors and walls of an operating room in Japan. It was found that after only one hour, bacteria counts on the walls were reduced to negligible levels. Furthermore, the surrounding air also experienced a significant reduction in the number of bacteria. More importantly, compared with the spraying of disinfectants, the use of such photocatalytic sterilizing ceramics is more effective in the long run (Chen and Poon, 2009a). On the basis of these appealing advantages, TOTO Ltd. has marketed this type of ceramic and expanded its application into hotels and restaurants.

2.4.2.4 Anti-Fouling Property

Principle Biofouling represents one of the main sources of aesthetic deterioration of cement-based building materials. Although algae are more resistant to PCO than bacteria, TiO_2-assisted photocatalysis has been shown to be able to degrade algae (Linkous et al., 2000). Similar to the bactericidal process, PCO of algae begins with dismantling the cell membrane and cell wall and then moves on to compromise the organelle membranes, which takes a longer time to accomplish. This corresponds to a commonly observed delay in the visible colour change of the algae. However, when the protective wall and membranes are damaged, the degradation of algal pigments components (such as chlorophyll a) proceeds relatively faster at a later stage. Ultimately, the algae conclude their lives by losing the ability to harvest light energy to produce the building blocks underpinning the intact whole cells (Peller et al., 2007).

Laboratory Investigation Laboratory tests to investigate the strategies of using TiO_2-based cementitious materials to eliminate biofouling have been conducted broadly. Different experiment set-ups have been developed, but they almost all operate in an accelerated fouling manner for the purpose of saving time (Fig. 2.21). For example, using a circulating flow-through chamber, the fungicidal activity of TiO_2 incorporated tiles was examined under artificial light irradiation. Various fungal strains were cultured to contaminate the surface of the samples. It was found that only a small amount of tan-coloured fouling was spotted on the TiO_2 incorporated tiles, while the reference samples without TiO_2 suffered a moderate fouling of black, tan and red colours (Giannantonio et al., 2009). The anti-algae fouling ability of mortars containing TiO_2 and Fe^{3+}-doped TiO_2 was evaluated and compared with commercial biocides. After exposure to a mixed culture of different species of algae for 4 months, the mortars containing TiO_2 and Fe^{3+}-doped TiO_2 experienced 0% and 11.8% of algae growth ratios, respectively (Fonseca et al., 2010). Moreover, the strategies of using TiO_2-

incorporated white cement pastes and three different coatings (TiO$_2$-ethanol suspension, water repellent layers and a combination of the TiO$_2$-ethanol suspension and water repellent layers) covered aerated concrete samples in antifouling of algae have been investigated and compared. Using an accelerated algal growth experiment set-up and *Chlorella vulgaris* as a model algae specie, the algae fouling on the surface of all the samples was monitored by means of visual inspections, algal coverage (%) and human perception of the colour changes. The results showed that the commercially available TiO$_2$ containing cement based samples delivered the best performance, with no visible algal growth ($\Delta E \leq 0.2$) and no significant algal coverage (0.1%). Samples with water repellent experienced only very obvious colour changes ($3.0 \leq \Delta E \leq 6.0$). In stark contrast, significant colour changes ($\Delta E = 20$) occurred on both the reference samples (Maury-Ramirez et al., 2013).
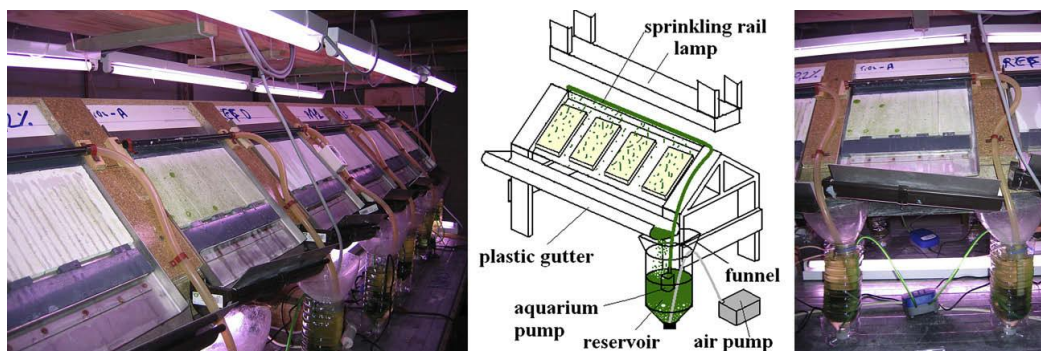
Figure 2.21 Modular setup used for the accelerated fouling of building materials by means of algae (Maury-Ramirez and De Belie, 2009)

Real-life Application When building materials are exposed to certain environments with a relatively high humidity, algal fouling becomes a nuisance (Fig. 2.22), which not only affects the aesthetic appearance but also can compromise the concrete's integrity by corrosion or physical degradation of hydration products at a later stage (De Belie, 2010). Traditionally, biocides and water repellents are employed to prevent algal from fixation and growth on building materials. However, these methods have their own limitations. For example, biocides need to be applied repeatedly and pose a health risk to the surrounding people

(Tiano, 2002). Water repellents can cause streaking when applied on aerated concrete (De Muynck et al., 2009).

Figure 2.22 Algal fouling of pavement blocks in Hong Kong

The application of photocatalytic building materials to combat the algal fouling problem is promising and attractive because of their environmentally-friendly nature. In Portugal, TiO_2 containing coatings were applied on 2 wall surfaces of the Palacio Nacional da Pena. After two weeks of exposure to atmospheric environments, the antifouling effect of the photocatalytic wall was evaluated by monitoring the colour changes. And satisfactory results have been obtained with respect to the degradation of lichens and other microorganisms. Despite the effectiveness observed in a short time frame, their long term efficiency and durability of the photocatalytic functions have yet to be determined (Fonseca et al., 2010). In Germany, roofing tiles coated with TiO_2 photocatalysts by employing the sol-gel technology were put into practical use in 6 different locations. After a service life of 6 years under outdoor conditions, it was found that the photocatalytic surfaces played a negligible role in affecting the phototrophic biofilms (Gladis and Schumann, 2011).

2.5 Summary

The benefits of developing and applying photocatalytic functional building materials have been well demonstrated. With only renewable solar light irradiation, photocatalytic functional cementitious materials are capable of a) self-cleaning dirt deposited on their surface with the

help of rain, b) purifying the neighbouring air by converting various air pollutants to harmless compounds, c) killing bacteria which pose health risks to humans and d) maintaining an aesthetically pleasant appearance by means of preventing algae and other biofoulings. As such, the costs of routine maintenance can be significantly reduced. Also, a more clean and healthy living environment is created. Moreover, the durability of cementitious materials is greatly enhanced, thus a longer service life can be expected.

However, the application of these value-added photocatalytic functional building materials is not without drawbacks. Normally, the cost of such building materials is very high compared with their conventional equivalent due to the relatively high price of TiO_2 photocatalysts. Thus, a higher initial investment is required. This limitation is compounded by the predominantly adopted intermixing method, which requires a large amount of TiO_2. Although applying TiO_2 coatings on the surface of building materials is a good alternative to bring down the cost, poor durability caused by weathering is a legitimate concern. Therefore, developing new adding methods to reduce the cost of photocatalytic functional building materials is in urgent need to broaden their practical applications. In addition, the influence of environmental factors, such as accumulation of dust and oil, on the performance of these photocatalytic functional products in real-life conditions deserves special attention.

<div align="right">

CHAPTER 3

Methodology

</div>

3.1 Introduction

This chapter mainly focuses on the experimental methods employed in the following parts of this thesis. First, information about the experimental materials is provided. Then, the procedures and methods for preparation of different types of photocatalytic specimens are presented. Afterwards, experimental set-ups and testing protocols concerning NO_x and xylene removal, RhB degradation, bacteria and algae killing, as well as the simulated weathering conditions, are described in detail. Finally, the methods adopted to determine the properties of various cement-based materials are furnished.

3.2 Materials

3.2.1 Photocatalysts

In all the experiments, a commercially available nano-TiO_2 powder (P25, Degussa) was used as the photocatalyst. The particle size of the TiO_2 was 20-50 nm, with a specific BET surface area of 50 ± 15 $m^2 \cdot g^{-1}$. In addition, a commercially available TiO_2 containing paint (PC-S7) was used to apply coatings on the surface of mortar samples. It was an aqueous dispersion (sol) of ultrafine anatase particles (specific surface area=300 $m^2 \cdot g^{-1}$). The TiO_2 content in the paint is about 10% (by weight) according to the information provided by the supplier.

3.2.2 Cementitious Materials

White cement (WC) (TAIHEIYO Cement Corp., Japan) and metakaolin (MK) (Maoming Kaolin Science and Technology CO., LTD.) were used as the cementitious materials to prepare the architectural mortar samples. MK was adopted to suppress the ASR because it

features a similar colour to WC. Table 3.1 provides the physical and chemical properties of WC and MK.

Table 3.1 Chemical compositions and physical properties of WC and MK

	WC	MK
Chemical compositions		
SiO_2	21.36	55.89
Al_2O_3	5.27	41.85
Fe_2O_3	0.2	0.68
CaO	67.49	-
MgO	1.14	-
K_2O	0.077	-
Na_2O	0.048	-
TiO_2	0.14	0.29
Sulphur content as SO_3	2.6	-
Loss in ignition	1.58	0.50
Physical properties		
Specific surface ($cm^2 \cdot g^{-1}$)	3660	15238

ASTM Type I Ordinary Portland cement (OPC, Green Island Cement Limited, Hong Kong) and fly ash (FA) were used as the cementitious materials to prepare the concrete surface layers. FA was added as a pozzolana to control the alkali-silica reaction (ASR) between the silica-rich glass cullet and the alkali in the cement. Their physical and chemical properties are listed in Table 3.2.

Table 3.2 Chemical compositions and physical properties of OPC and FA

	OPC	FA
Chemical composition		
SiO_2	22.18	56.79
Al_2O_3	5.95	28.21
Fe_2O_3	3.37	5.31
CaO	62.46	<3.00
MgO	1.56	5.21
K_2O	0.48	-
Na_2O	0.24	0.68
TiO_2	0.37	-
Sulphur content as SO_3	2.25	-
Loss in ignition	0.64	3.90
Physical properties		
Specific surface ($cm^2 \cdot g^{-1}$)	3660	4120

3.2.3 Aggregate

A fine natural river sand (mainly quartz sand) sourced from the Pearl River and crushed recycled glass (RG) derived from post-consumer beverage glass bottles were used as fine aggregates. The saturated surface dry density of the sand was 2650 kg·m^{-3}. The post-consumer beverage glass bottles were collected from a local eco-construction material company. The beverage glass bottles collected were mainly mixed coloured. The chemical compositions of the RG are given in Table 3.3. Prior to the experimental use, all the discarded glass bottles were washed and then crushed by a mechanical crusher, followed by sieving to a desired particle size. The typical particle size distribution of the river sand and RG used in the experiment are shown in Fig. 3.1.

Table 3.3 Chemical compositions of RG.

Chemical composition	Mixed coloured RG (ms%)
SiO_2	63.81
Al_2O_3	11.77
Fe_2O_3	0.26
CaO	5.56
MgO	1.57
K_2O	0.31
Na_2O	16.62
Cr_2O_3	0.04
MnO	0.01
CuO	-
TiO_2	0.04
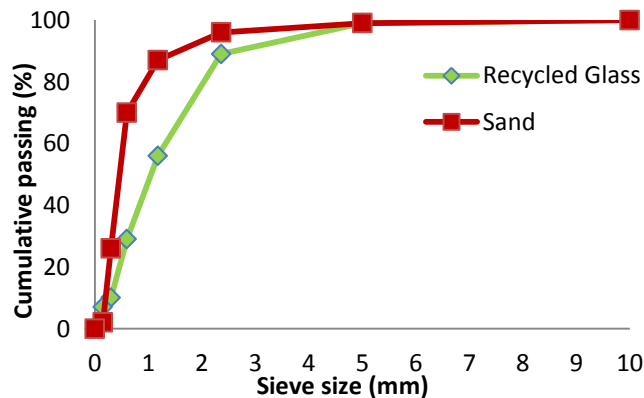
Figure 3.1 Sieve analysis of fine aggregates.

3.3 Sample Preparation

3.3.1 Fabrication of Self-Compacting Architectural Mortars

A self-compacting-based approach was selected to prepare the architectural cement mortar due to the high quality surfaces obtained using this method (De Schutter et al., 2008). To obtain this, a superplasticizer (ADVA 109, Grace Construction Products) was added to the mix until the mini-slump flow test indicated (25±1 cm) by EFNARC was obtained. Also, based on our previous feasibility study on the use of RG in architectural cement mortars, a mix proportion of 0.8:0.2:2.0:0.4 (WC: MK: fine aggregate: water) was used for preparing all samples (Ling et al., 2011).

All the constituents used for preparing the mortar samples were fed into a standard rotating pan mixer (RP100XD, Croker) with a capacity of 163 litres and a mixing rate of 16 revolutions per minute (rpm). Initially, all the dry components (WC, MK, fine aggregate and TiO_2) were mixed for about 3 min before water specified in the mix design (together with the superplasticizer premixed) was added. To ensure the homogeneity of the mix, the mechanical mixing was stopped after 3 min, and the constituents were further manually mixed using a steel trowel. After that, the mechanical mixing continued for 3 more min. Then, the fluidity of the freshly prepared mortar was evaluated using the mini-slump flow test as indicated above. All the samples were kept in the moulds in the moist room (at a temperature of 23.0±2.0 ℃ and a relative humidity of not less than 95%) for 24 h. Then, the samples were demoulded and immersed in saturated lime water in storage tanks (at a temperature of 23.0±2.0 ℃) until testing.

Three sets of samples were prepared to examine the effect of glass aggregate on the photocatalytic NO_x removal. The first group was prepared using recycled glass as the fine aggregate (100% Glass). The second group was prepared using a mixture of river sand and recycled glass (50% Glass & 50% Sand) as the fine aggregate. The third group was prepared

using only river sand (100% Sand) as the fine aggregate.

For each prepared mix proportion (in total 15 architectural mortar mixes were prepared), two cubes (10×10×10 cm) for compressive strength, two prisms (4×4×16 cm) for flexural strength, three prisms (2.5×2.5×28.5 cm) for alkali-silica-reaction expansion, two cubes (10×10×10 cm) for carbonation depth and a cylinder (dia.10 cm × height 20 cm) for the photocatalytic NO_x removal (three discs (Ø10 cm × 1 cm height) cut from the cylinder) and the permeable voids content were casted.

To assess the effect of the mixing rate on the properties of the prepared mortar, another electric mixer (CE-207XG, Fargo–Century Equipment Company Ltd.) with a smaller capacity (7 litres) and a significantly faster mixing rate (190 rpm) was used to prepare a second group of mortar samples (with the same mix design as previously described).

For the intermixing method, TiO_2 nanoparticles were added to the mortar samples in concentrations of 1.5, 3, 4 and 5% by weight of the cementitious phase. Also, samples without TiO_2 were prepared as reference.

For the coating approach, the samples were prepared by brushing the anatase aqueous dispersion (PC-S7) in 3 layers (dried at room temperature and humidity for approx. 15 min between applying successive layers) onto the prepared reference architectural mortars (without TiO_2). On one hand, the adopted coating procedures are able to render homogeneously distributed films on the substrate surface (easily observed by naked eyes). On the other hand, since the photocatalytic activity is heavily dependent on the outer layer (which is directly exposed to light irradiation), applying more TiO_2 coatings does not necessarily lead to a proportional increase in photocatalytic efficiency (proven by pre-conditioning tests).

3.3.2 Fabrication of Cement Pastes

All the cement paste samples were prepared with a constant water-to-cement ratio of 0.4.

Two different dosages of nano-TiO_2 (2% and 5% by cement weight) as an addition to the cement/water mixture were used. Blank samples without TiO_2 addition were also made for comparison. All the proportioned powder materials were first mixed uniformly for about 5 min using a mechanical mixer. After that, water was added. A smooth and well blended paste was produced by further mixing for another 5 min. The paste was then cast into Petri dishes (Ø7.5×2.0 cm). The Petri dishes were vibrated by a vibrating table to ensure thorough compaction. The samples were then allowed to cure in an environmental chamber at 25 °C and 95% RH for 24 h. After that, the hardened pastes were removed from the Petri dishes and placed back into the same chamber at the same conditions until testing.

Dry mixtures of the nano-TiO_2 (2% and 5% by cement weight) particles and anhydrous cement (without the addition of water) were also prepared. To investigate the effect of Fe_2O_3 (Sigma-Aldrich 99.999%, trace metal basis) on the photocatalytic NO_x removal, four different dosages of Fe_2O_3 (0%, 2%, 5% and 10% by WC weight) were added as a replacement of WC to the 2% TiO_2 blended WC dry mixtures. 40 g of the uniformly blended dry mixtures were weighted and then put into the Petri dishes for the photocatalytic NO_x removal experiment.

For the other characterization experiments (Diffuse Reflectance UV-Vis Spectroscopy Analysis, Electrochemical Impedance Spectroscopy, Photoluminescence Spectra), the dry mixtures were also adopted. TiO_2 and Fe_2O_3 were added and the dosages were varied accordingly to the sensitivity of different characterization equipment.

3.3.3 Fabrication of Surface Layers

The surface layers were fabricated in the laboratory in steel moulds with an internal dimension of 200×100×5 mm. Based on our previous study (Guo and Poon, 2013), the mix proportions (by mass) for the concrete surface layers were 0.75:0.25:3.0:0.3 (OPC: FA: RG: water). The procedures for the preparation of the concrete surface layers were as follows.

First, all the proportioned materials were mixed uniformly for about 5 min using a mechanical mixer. For each concrete surface layer, 250 g well-mixed materials were weighted. Then, the steel moulds were over filled with the mixed materials and hand compacted, followed by further compressed twice using a compression machine at a rate of 500 kN·min^{-1}, firstly to 500 kN and secondly to 600 kN. After one day, the surface layers were removed from their moulds and were tightly wrapped by plastic films for curing until testing.

For the intermixing method, the nano-TiO$_2$ was added at 5% by cementitious materials weight to the cement mortar mixture (Intermixed-Type 1). The nano-TiO$_2$ powders were directly and intimately intermixed with the cementitious materials during sample casting.

To prepare the TiO$_2$ sprayed samples, a suspension of ethanol (VWR International S.A.S.) and P25 (30 g·L^{-1}) was prepared. The surface layers were first sprayed with the TiO$_2$-ethanol suspension 20 times, followed by mechanical compaction, and for another 20 times after the compaction (SP-Type 2). All the spraying was performed within 10 min after the surface layers were manually or mechanically compacted.

To prepare the nano-TiO$_2$ dip-coated concrete surface layers (DC-Type 3), the surface layers without TiO$_2$ after 28 days of curing were immersed (dipped) into the prepared suspension (which was the same as in the spray method) for 5 min, followed by oven-drying at 60 °C for 120 min.

The processes of three TiO$_2$-adding methods (intermixing, spray-coating and dip-coating) are schematically illustrated in Fig. 3.2.
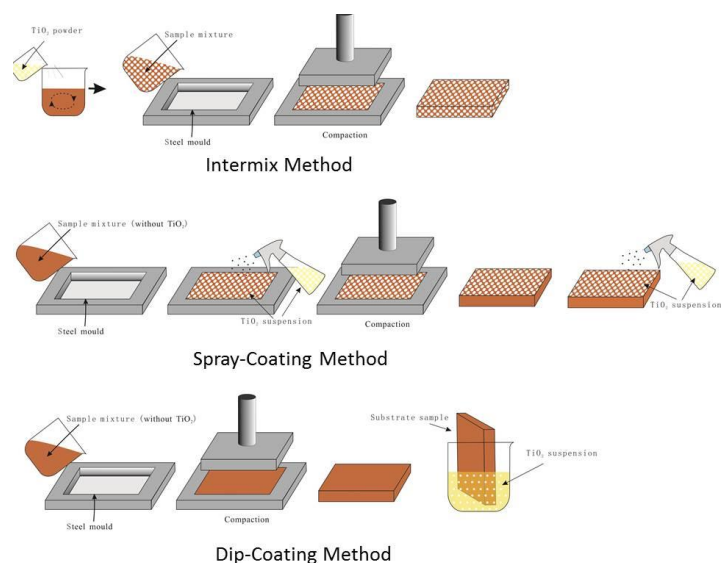
Figure 3.2 Schematic diagram of nano-TiO$_2$ intermix, spray-coating and dip-coating methods

3.4 Photocatalytic Removal of NO$_x$ and Xylene

3.4.1 Experimental Set-Up

A continuous flow reactor (with dimensions of 300 mm long, 150 mm wide and 100 mm high) was developed in accordance with the specifications of JIS R1701-1 with modifications to house the testing samples. The reactor was completely sealed with no detectable leakage. A schematic diagram of the experimental setup is shown in Fig. 3.3. Except for different test series where NO flow rates, initial NO concentration, UV light intensities, five light sources (Table 3.4) and relative humidity were variables, respectively, the experimental conditions were set as the following: All the tests were carried out at ambient temperature (25±3 ℃) and pressure. The flow rate (3 L·min^{-1}) and initial concentration (1000±50 ppb NO and 200±50 ppb xylene) of the testing gas were achieved by tuning two flow controllers. The NO$_x$ concentration was constantly recorded by a chemiluminescence NO$_x$ analyser (Model 42c, Thermo Environmental Instruments Inc.). The real-time xylene concentration was measured by a total VOC analyser (PPBRAE Model PGM-7240, RAE System Inc.). Two UV-A fluorescent lamps (2×F8T5 BLB, HRK) were positioned parallel to each other on the glass

cover of the reactor to provide UV radiation to obtain a required light intensity of 2 W·m^{-2}, measured by a UV light meter (LT Lutron, Digital Instruments) calibrated at 340 nm, at the centre of the reactor by adjusting the distance between the UV lamps and the reactor, while the relative humidity (RH) in the reactor was controlled at 30±5% by passing the zero air streams through a humidification chamber.
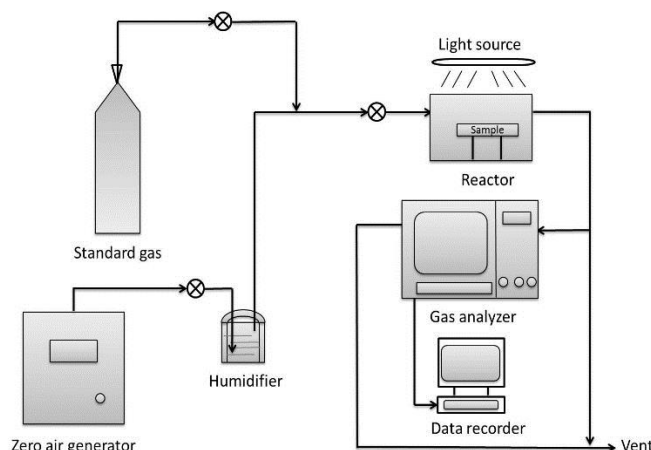
Figure 3.3. Schematic diagram of gaseous pollutants removal equipment

Table 3.4 Five different lamps used for photocatalytic NO$_x$ degradation

Lamp type	Description	Spectrum
SL (Solar light)	1 halogen photo optic lamp, QUADX 3000, BOEWNS, UK	100<λ(nm)<700
UVA	2 × F8T5 BLB, HRK	340<λ(nm)<410
LED	7 strips, Yes International Company	405<λ(nm)<410
VL (Visible light)	1 halogen photo optic lamp with a UV light filter, which can filter out the lights below 400 nm	400<λ(nm)<700
FL (Fluorescent light)	2 × YZ08 T5, NVC	400<λ(nm)<800

3.4.2 Testing Protocol

Prior to all photocatalytic conversion processes, the testing gas stream was allowed to pass through the reactor in the absence of the light radiation for at least half an hour to obtain the desired RH as well as gas-solid adsorption-desorption equilibrium. When the concentration of the gaseous pollutant reached equilibrium in the reactor, the lamps were turned on and the

photocatalytic degradation was allowed to go on for 30 min. The calculation of the NO_x removal rate is shown below:

$$Q_{NOx} = \frac{\left(\frac{f}{22.4}\right)\{\int([NO]_0 - [NO])dt - \int([NO_2] - [NO_2]_0)dt\}}{A \times T}$$

Equation 3.1

where Q_{NOx} ($\mu mol \cdot m^{-2} \cdot h$) is the amount of nitric oxides removed by the test sample, $[NO]_0$ and $[NO_2]_0$ (ppm) are the inlet concentration of nitrogen monoxide and nitrogen dioxide, respectively, $[NO]$ and $[NO_2]$ (ppm) are the outlet concentration of nitrogen monoxide and nitrogen dioxide, respectively, t (min) is the time of removal operation, f ($L \cdot min^{-1}$) is the flow rate converted into that at the standard state (0 °C, 1.013 kPa), A (m^2) is the surface area of cement paste samples, T (0.5 h for all experiments) is the duration of the photocatalytic process, and 22.4 represents that the volume of 1 mole ideal gas at the standard state is 22.4 L (ideal gas law).

On the other hand, the NO_x removal ratio was presented according to the following equation:

$$NO_x \text{ removal ratio} = \frac{([NO]_0 + [NO_2]_0) - ([NO] + [NO_2])}{[NO]_0 + [NO_2]_0}$$

Equation 3.2

where $[NO]_0$ and $[NO_2]_0$ represent the inlet concentration of nitrogen monoxide and nitrogen dioxide, respectively, and $[NO]$ and $[NO_2]$ represent the outlet concentration of nitrogen monoxide and nitrogen dioxide, respectively.

For the xylene removal, the removal rate (%) was presented according to the following equation:

Xylene removal rate (%) = ([xylene]$_{inlet}$-[xylene]$_{outlet}$)/[xylene]$_{inlet}$×100%   Equation 3.3

where [xylene]$_{inlet}$ represents the concentration of xylene in the feeding stream and [xylene]$_{outlet}$ is the concentration of xylene in the outlet stream.

3.5 Photocatalytic Degradation of RhB

3.5.1 Determination of Ideal RhB Volume and Concentration
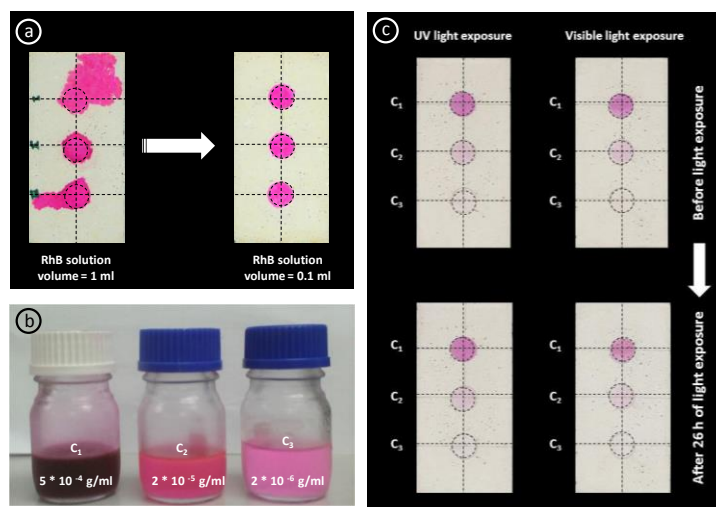
Figure 3.4 Determination of the optimal RhB solution volume (a) and concentration (b and c).

Rhodamine b (RhB) ([9-(2-carboxyphenyl)-6-diethylamino-3-xanthenylidene]-diethylammonium chloride) was selected as an organic dye model to simulate air particulate pollutants because its molecule structure is similar to some airborne particulate compounds such as polycyclic aromatic hydrocarbons (PAHs) (Rout et al., 2009; Folli et al., 2012; Krishnan et al., 2013a). Prior to the evaluation of the self-cleaning potential, the required volume and concentration of RhB to be applied on the sample surface were determined (Fig. 3.4). 0.1 mL of RhB solution with a concentration of 5×10^{-4} g·mL^{-1} was found to be adequate (Fig. 3.4), and it was applied evenly on 3 standardized positions (5 cm^2 e.a.) on the mortar specimen surfaces and allowed to oven-dry (60 ℃) overnight. The RhB contaminated sample was then exposed to UV-A irradiation under laboratory conditions (T=25 ℃ and RH=50%), which were provided by UV-A lamps (2×F8T5 BLB, HRK). During the UV-A irradiation, the UV-A intensity was maintained between 310-350 µW·cm^{-2}, as indicated by a UV light meter (LT Lutron, Digital Instruments) calibrated at 340 nm.

3.5.2 Testing Protocol

The colour changes of the dye before and after the light irradiation were measured by a portable sphere spectrophotometer (SP60, X-Rite). The readings were expressed with L^*, a^* and b^* colorimetric coordinated in the CIE LAB system (Fig. 2.13).

As can be seen in Fig.2.13, (L^*) plots the lightness of luminance from white to black, (a^*) represents values between red and green, and (b^*) does the same with values between blue and yellow. Analysis of the RhB degradation was then based on the comparison of the colour parameter a^* before ($a^*(0h)$) and after 4h ($a^*(4h)$) and 26h ($a^*(26h)$) of UV light irradiation. These RhB removal efficiencies (R_4 and R_{26}) can be calculated as indicated in Equations 3.4 and 3.5. Finally, the material is considered as photocatalytic if $R_4 > 20\%$ and $R_{26} > 50\%$ (Cassar et al., 2007).

$$R_4(\%) = \left[\left(a^*(0h) - a^*(4h) \right) \times a^*(0h)^{-1} \right] \times 100\% \qquad \text{Equation 3.4}$$

$$R_{26}(\%) = \left[\left(a^*(0h) - a^*(26h) \right) \times a^*(0h)^{-1} \right] \times 100\% \qquad \text{Equation 3.5}$$

3.6 Photocatalytic Killing of Bacteria

3.6.1 Bacterial Strains and Culture Conditions

A UV-resistant *E. coli* K12 was used as the test strain in this study, which is a gram-negative bacterium widely selected as a model microorganism in many photocatalytic bactericidal experiments. *E. coli* K12 was sub-cultured and maintained on nutrient agar plates. To prepare the bacterial cultures for the experiment, single colonies were isolated from the nutrient broth agar plate cultures and used to inoculate 50 ml of the nutrient broth liquid media (pH 7) in a 250 ml flask. Then the flask was incubated at 37 °C for 18 h in an orbital incubator set at 150 rpm. To eliminate broth medium, the cells were harvested by centrifugation at 4000 rpm for 5 min. After this, the treated cells were washed, re-suspended and diluted to the targeted concentration of about 1×10^5 colony forming units (CFU)/ml in sterilized 0.9% (w/v) sodium

chloride solution. All the equipment and materials were autoclaved at 120 °C for 15 min before the experiment to ensure sterility.

3.6.2 Testing Protocol

The experimental set-up for photocatalytic inactivation of *E. coli* K12 is shown in Fig. 3.5. 1 mL of *E. coli* K12 cell suspension was pipetted onto each of the prepared samples, which were then placed in sterilized Petri dishes to prevent drying. The Petri dishes with the testing sample were subject to illumination by the same UV-A lamps used in the NO_x removal experiments. The light intensity striking the surface of testing samples was 2 $W \cdot m^{-2}$. The cell suspension was collected by washing the sample with 20 mL 0.9% sodium chloride solution at different time intervals of 30, 60, 90 and 120 min, respectively, after the irradiation. Then serial dilutions of the collected cells suspension were appropriately performed, and 100 µL of diluted suspension was spread on the nutrient agar plate and incubated at 37 °C for 18 h. Three replicated plates were used for each incubation to verify the reproducibility of the results. The loss of viability was examined by the viable count of the colony forming units on the plates. In all the experiments, negative control tests under conditions of darkness and positive controls were carried out simultaneously.
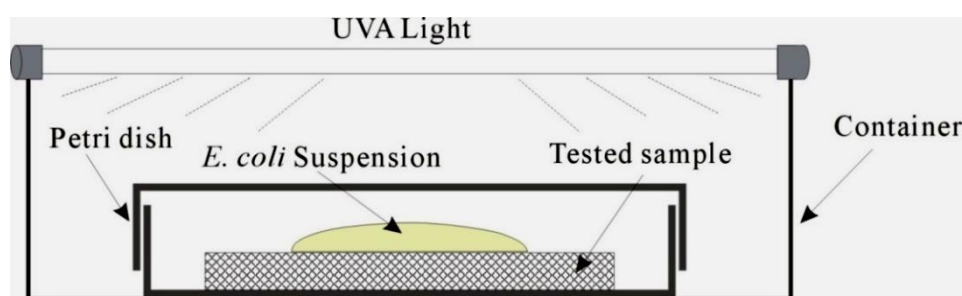
Figure 3.5 Schematic diagram of bacterial inactivation experimental set up

3.7 Photocatalytic Killing of Algae

3.7.1 Algae Strains and Culture Conditions

Figure 3.6 Algae cultures of *chlorella vulgaris fo. viridis* in Bold Basal Medium with 3-fold

Nitrogen and Vitamins

Chlorella vulgaris fo. viridis was selected as the model algae species due to its representativeness and relatively simple liquid culture preparation method (Fig. 3.6). The strain was obtained from the culture collection of algae and protozoa (CCAP) from Dunstaffnage Marine Laboratory (Scotland, UK) (accession number CCA 211/12). Batch cultures of the algae were grown under sterile conditions in Erlenmeyer containing 1 L of growth medium for freshwater algae (Bold Basal Medium with 3-fold Nitrogen and Vitamins). The Erlenmeyer were continuously aerated by means of aquarium pumps (9901, Sonic) and exposed to fluorescent lamps (T514W, Aqua Gem) on a shaker (Stuart Scientific) at 75 rpm. For the preparation of 1 L of the growth medium, 10 mL of $NaNO_3$, $CaCl_2 2H_2O$, $MgSO_4 7H_2O$, $K_2HPO_4 3H_2O$, KH_2PO_4, $NaCl$, 1 mL of vitamin B_1 (thiaminhydrochloride solution) and B_{12} (cyanocobalamin solution) and 6 mL of a trace element solution ($FeCl_3 6H_2O$, $MnCl_2 4H_2O$, $ZnCl_2$, $CoCl_2 6H_2O$ and $Na_2MoO_4 2H_2O$) were added (De Muynck et al., 2009).

3.7.2 Experimental Set-Up

The accelerated algae fouling test set-up is provided in Fig. 3.7. It is consisted of three

inclined (45º) and independent PVC compartments where samples were placed and subjected to two daily (every 12 h) alternate wet cycles (algae suspension 6.5×10^8 cells·L^{-1}) lasting 1.5 h. As algae are photosynthetic microorganisms, their growth is also stimulated by creating 12 h day and night regimes, which started simultaneously with the run-off periods. The day regimes were created by a combination of fluorescent lamps (T5 14W, Aqua Gem) that were specially designed to assist algae growth. Irradiation peaks of the lamps were at 440, 550 and 610 nm. In addition, UV-A lamps (F8T5 BLB, HRK) were used to activate the photocatalytic action. The irradiation level at the centre of the specimens reached 350 ± 10 µW·cm^{-2}. On the other hand, as darkness triggers other cell activities, both the light sources (fluorescent and UV-A) were switched off for 12 h each day.

Figure 3.7 Accelerated algae fouling test set-up

3.7.3 Testing Protocol

Apart from visual inspection, two quantitative methods, which are based on the CIE Lab space (section 3.5), were used to evaluate the algae fouling activity. First, the extent of the algae fouling was measured by means of image analysis. Second, due to the presence of chlorophyll, the extent of algae fouling was also related with the green colour intensity of the colonized area. Thus, the colour changes on the sample surface were monitored and analysed by a colorimetric measurement. All the reported data for the accelerated algae fouling test are

the means obtained from 3 samples

For the image analysis method, the images from all the specimens were obtained with the use of a scanner LiDE 110 (Canon, Japan). These images were subsequently processed by means of an Image J 1.38x software. The quantification of the fouled area was based on threshold analysis from the b^* coordinate (blue to yellow axis) from the CIE Lab colour space. Fig. 3.8 shows the image analysis of one sample. The pixels with b^* values below 138 on a scale of 0-256 were considered as unfouled area (changed to black pixels), while those with b^* values above 138 were regarded as fouled area (changed to white pixels). The total amount of black and white pixels was then calculated by means of the 'analyse, histogram' function for each sample. From the latter, the percentage of fouled area was calculated as indicated in Equation 3.6.

Fouled area (%) = (white pixels/(white pixels+black pixels)) × 100%   Equation 3.6
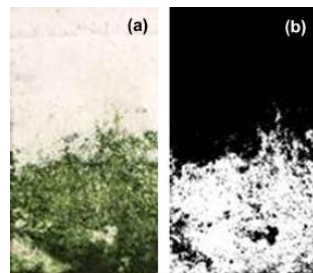
Figure 3.8 Image analysis of a significantly fouled paste sample before (a) and after (b) thresholding (Maury-Ramirez et al., 2013)

The colorimetric measurements were performed by means of a colorimeter (SP60, X-Rite) to examine the colour changes of the samples. For each sample, three measurements were taken at standardized positions in the upper, middle and lower parts of the samples before and during the accelerated algae fouling test. In order to avoid the influence of humidity, the surface of the testing samples were allowed to dry for approx. 2 h at room temperature before testing, and the CIE Lab colour values were obtained. A colour change parameter (ΔE) was calculated as indicated in Equation 3.7.

$$\Delta E = (\Delta L^2 + \Delta a^2 + \Delta b^2)^{1/2}$$

<div align="right">Equation 3.7</div>

Where $\Delta L = L_t^* - L_0^*$; $\Delta a = a_t^* - a_0^*$; $\Delta b = b_t^* - b_0^*$ with L_t^*, a_t^*, b_t^* being color values at specific week (t) after the start of the fouling experiment and L_0^*, a_0^*, b_0^* being colour values at the start of the test (samples not fouled). Based on computer simulations that estimate the human perception of the color changes (ΔE) after the aesthetic rehabilitation of architectural concrete, the produced colour changes on the test samples were assessed by following the parameters indicated in Table 3.5 (Zhan, 2005).

<div align="center">Table 3.5 Human perception of the colour changes after aesthetic rehabilitation of architectural concrete.</div>

Colour change (ΔE)	Human perception
0.0-0.2	Not visible
0.2-0.5	Very slight
0.5-1.5	Slight
1.5-3.0	Obvious
3.0-6.0	Very obvious
6.0-12.0	Large
≥ 12	Very large

3.8 Weathering Conditions

In order to determine the effect of weathering on the photocatalytic activity of various types of samples, different weathering processes were developed in the laboratory and applied on the tested samples.

3.8.1 Simulated Façade Weathering

The lab-simulated façade weathering process (Fig. 3.9) mimics the weathering process caused by rain water and sunlight on a building material applied vertically at outdoors. The test set-up was used in the algae fouling test (section 3.7.2). Here, in the façade weathering simulation, the algae solutions were replaced by tap water. The wet condition was imposed on each compartment by pumping 1.5 L of tap water during 12 h by means of an aquarium pump

(New-Jet 400, Aquarium Systems-Newa). On the other hand, the dry condition was applied by simply switching off the pumps for the following 12 h. The day and night conditions were coordinated respectively with the dry and rain conditions and each lasted also 12 h. For the day condition, light irradiation was supplied by three UV-A (3×F8T5 BLB, HRK) and two visible lamps (T514W, Aqua Gem). The UV-A intensity striking on the surface of photocatalytic self-compacting architectural mortars was 350 ± 10 $\mu W \cdot cm^{-2}$. The duration of the coordinated 'rain/dry' and 'day/night' cycles was 2 weeks. Considering the simulated 'rain' conditions (290 mm·h^{-1}) selected for operating the test set-up on the one hand and the Hong Kong average rainfall (2315 mm·year^{-1}) on the other hand, the weathering process represents approximately 20 years of weathering. Although other factors, such as UV exposure, do exert influences on the deterioration of the samples, their contributions were found less significant than the dry-wet cycles. For example, only UV radiation (up to 1800 h) caused no observable physical degradation of TiO_2 nano-coating, while wet/dry cycles resulted in a certain degradation of the nano-coating (Graniani et al., 2014). Thus, a rough estimation of weathering years in real conditions in Hong Kong was only based on the volume of rainfall.
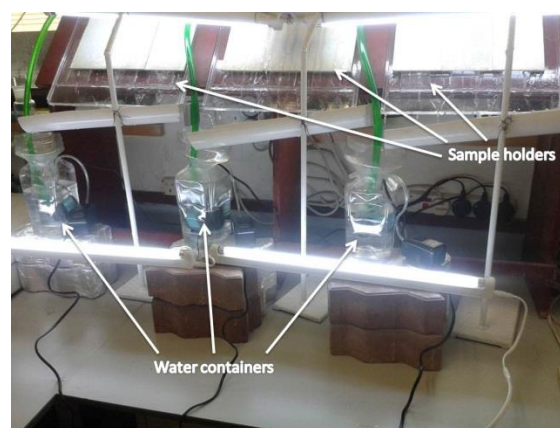
Figure 3.9 Weathering test set-up and operating conditions (UV-A intensity=350 ± 10 $\mu W \cdot cm^{-2}$; Rain water intensity=290 mm·h^{-1})

3.8.2 Accelerated Carbonation

To evaluate the resistance of the samples to carbonation, the international standard method ISO/DIS 1920-12 was followed. The accelerated carbonation was carried out in a carbonation chamber (Yue Fat Engineering and Oven Works) with 4 % concentration (20 ℃ and 60% relative humidity). The carbonation reaction was allowed to go on for 70 d before the samples were taken for subsequent photocatalytic tests.

3.8.3 Abrasion

To evaluate and compare the resistance of the Intermixed-Type 1, SP-Type 2 and DC-Type 3 concrete surface layers to weathering, a harsh abrasion action was applied to the surface of the testing specimens. A concrete slab with a dimension of 200×100×60 mm which weighed 2,850 g was used to apply the abrasion load. The abrasion was applied by means of an abrasive paper (grade: Cw 220-2c) which was firmly attached on the surface of the concrete slab. The surface layer to be tested was first positioned by putting it into a steel mould. Then, the slab with the abrasive paper was placed on the surface of the samples. The slab with the attached abrasive paper was pushed back and forth from one end to the other end of the surface layer horizontally (no extra weight was added except the weight of the slab). After the prescribed number of abrasion, the sample was re-tested for its change in photocatalytic activity. A schematic diagram of the abrasion setup is provided in Fig. 3.10.
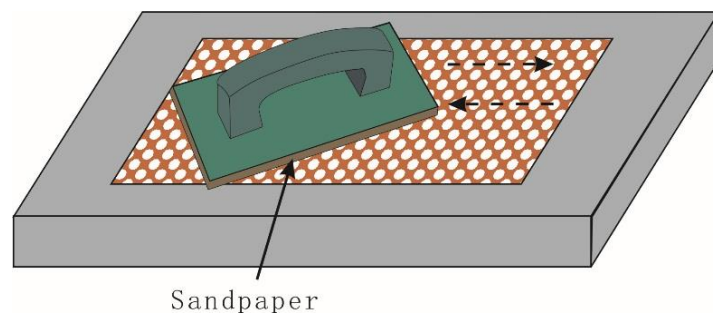
Figure 3.10 Schematic diagram of abrasion action experimental set-up

3.8.4 Dust Accumulation and Oil Contamination

The effectiveness of the NO_x removal capacity of the Intermixed-Type 1 and SP-Type 2 concrete surface layers after subjected to dust accumulation and oil impregnation was determined. After which, the samples were subjected to a myriad of cleansing processes, and the recovery of their NO_x removal capacity was then evaluated.

3.8.4.1 Dust Accumulation and Cleansing Processes

A fine dust (ISO 12103-1 A2) provided by Powder Technology Inc was employed in order to simulate the effect of natural dust accumulation. Fig. 3.11 describes the grading size distribution of dust particles (the data was provided by Powder Technology Inc.).
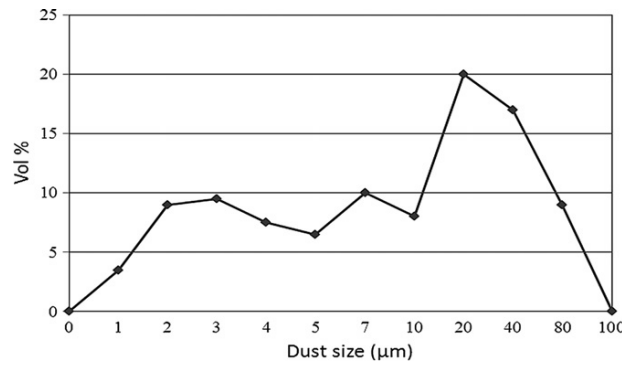
Figure 3.11 Volume dust particle distribution

The specific weight of the dust was 2.65 g·cm^{-3}, and the chemical compositions were determined to be basically SiO_2 and Al_2O_3. The compositions of the dust (by weight) are given in Table 3.6.

Table 3.6 Chemical compositions of dust

Component	% in weight	Component	% in weight
SiO_2	68-76	CaO	2-5
Al_2O_3	10-15	MgO	1-2
Fe_2O_3	2-5	TiO_2	0.5-1
Na_2O	2-4	K_2O	2-5

The photocatalytic effectiveness of concrete surface layers could be affected by dust accumulation on their surface. In the laboratory, a chamber designed to simulate the real application situation was used. The test chamber (1×0.6×0.6 m) was made with ESD acrylic

plates which were both transparent and antistatic. The test dust was injected by the dust generator (RBG 1000, PALAS) into the test chamber and mixed with air by means of a fan. Dust was deposited, slowly and naturally, on the surface of the samples, which were positioned in the centre of the chamber (Fig. 3.12).
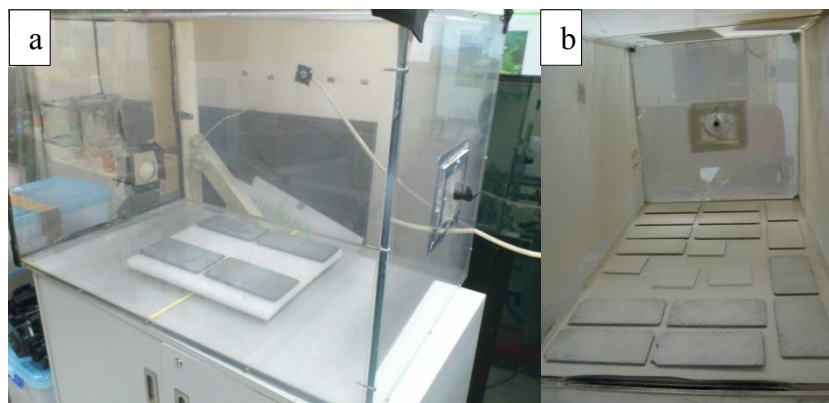
Figure 3.12 a) Dust chamber and b) Dust accumulation on the surface of samples in the chamber

The amounts of dusts accumulated on both the surfaces of the Intermixed-Type 1 and SP-Type 2 samples were 0, 10, 18 and 37 $g \cdot m^{-2}$. Fig. 3.12b shows several samples subjected to the dust accumulation process. Fig.3.13 shows 10 and 37 $g \cdot m^{-2}$ of dust accumulation on the sample surfaces. The NO_x removal capacity of Intermixed-Type 1 and SP-Type 2 samples with different weight of dust accumulation on their surfaces was immediately evaluated. Then, cleansing processes were carried out in order to recover the NO_x removal ability of the samples. Two cleansing processes were applied on each sample. First, slow flowing tap water, with an approximately flow rate of 6.25 $cm^3 \cdot s^{-1}$, was applied to the surface of the samples. Second, besides the water cleansing (under the same condition), an electric brush was also used to clean the samples' surface. Immediately after the cleansing process, all the samples were oven-dried (60 ℃ for 24 h) until testing. The photocatalytic activity of each sample was evaluated and the obtained results were compared to those of the reference samples (without dust accumulation).

Figure 3.13 Left, 10 g and right, 37 g of dust were accumulated per m^2 of surface

3.8.4.2 Oil Accumulation and Cleansing Processes

A synthetic motor oil of 15W-40 viscosity (Castrol GTX Diesel 15W-40, Castrol Limited) was employed to impregnate the surfaces of Intermixed-Type 1 and SP-Type 2 samples. It is mainly composed of poly-alpha-olefin, poly-internal-olefins and esters. The surfaces of the concrete surface layers were impregnated using two types of oil-solvent mixtures separately. First, a low viscosity oil-solvent mixture consisting of 50% weight of oil and 50% weight of ethanol (with ratio of 1:1) was prepared. This low viscosity mixture was then applied on the samples in a dose of 200 g per m^2 of concrete surface. Second, 400 g of undiluted motor oil per m^2 of concrete surface was also used to contaminate the surface of the samples. A 3 mL pipette dropper was employed, and the oil-solvents were distributed drop by drop in order to guarantee their homogeneous accumulation on the surface. 5 pipettes were applied to disperse all the oil-solvents on each concrete sample of a fixed area (20×10 cm^2). The degradation of NO$_x$ of the Intermixed-Type 1 and SP-Type 2 samples after oil accumulation was determined. Then, several cleansing processes were used to try to rejuvenate the samples. The oil contaminated samples were cleaned by separately adding to the surfaces two oil removing products (an alkaline industrial detergent and water or an organic solvent (n-hexane)). For the cleansing process using the n-hexane solution, the spray SP-Type 2 samples were cleaned by means of adding the n-hexane solvent to the surface and submerging the samples in hexane for another 12 h (named as cleaned–hexane-2).

3.9 Determination of Properties of Cementitious Materials

3.9.1 Compressive Strength

The compressive strength tests were performed according to the ASTM C109 after curing the samples under water a certain period. The specimens (2 repetitions) were tested in a compression machine (3000 kN, Matest) under a controlled loading rate of 0.6 MPa per second. Then, when the maximum load was reached, the value was recorded. Finally, the compressive strength (MPa) was calculated by dividing the maximum load (N) by the measured loaded area (mm^2) of the cube (Equation 3.8).

$$f_m = P/A \hspace{6cm} \text{Equation 3.8}$$

Where f_m represents the compressive strength (MPa), P is the total maximum load (N), and A is the area of loaded surface (mm^2).

3.9.2 Flexural Strength

The flexural strength test was conducted as indicated in the ASTM C348 after certain days of curing the samples under water. For each mix, two prisms (4×4×16 cm) were used. In this case, samples were tested in a universal testing machine (100 kN, Testometric) under a central line load while simply supported over a span of 12 cm. The samples were then loaded at a controlled displacement rate of 0.1 mm per min until failure. The flexural strength (S_f, MPa) can be calculated using Equation 3.9:

$$S_f = 0.0028 \ P \hspace{6cm} \text{Equation 3.9}$$

Where S_f is the flexural strength (MPa), and P is the total maximum load (N).

3.9.3 Permeable Voids Content

In order to determine the permeable voids content of the architectural samples, the method described in the ASTM C 642-06 was followed. Using an automatic abrasive cutter (Delta, Buehler) at a cutting rate of 5 mm·s^{-1}, three cylindrical specimens (dia. 10 cm × height 5 cm)

were obtained from a cylinder (dia. 10 cm × height 20 cm). Then, specimens were oven-dried at 105 °C for not less than 24 h until a constant weight was achieved. The weight obtained in this stage was the mass of the oven-dried sample in air (A). The specimens were then immersed in water at 21°C for not less than 48 h until a constant weight was achieved. Afterwards, the samples were boiled in water for 5 h. Then, the mass (B) of surface-dry samples in air after boiling and immersion was obtained. Finally, by suspending the samples with a wire and immersing them in water, the apparent mass of samples in water after immersion and boiling (C) was obtained. So, the permeable voids (%) of the samples could be obtained by using Equation 3.10.

$$Permeable\ voids\ (\%) = (B - A) \times (B - C)^{-1} \times 100 \qquad \text{Equation 3.10}$$

3.9.4 Expansion due to Alkali-Silica-Reaction (ASR)

Using two mortar bar samples (2.5×2.5×28.5 cm), the evaluation of the expansions caused by the alkali-silica-reaction (ASR) in the architectural mortars was conducted following the accelerated bar method which is described in the ASTM C1260. In this method, by immersing the mortar bar samples in a hot sodium hydroxide (NaOH) water solution (80 °C) during 14 d, the ASR reaction was enhanced. As initial measurement (zero reading), expansions of the samples were taken after immersing them in a hot water bath (80 °C) during 24 h. Expansion measurements were then taken three to four times during 14 d by taking the samples out (max. 15 s) of the NaOH water solution. Finally, the difference between the zero reading of one specimen and the reading at each period was calculated as the expansion of the specimen for that period.

3.9.5 Carbonation Depth

For the evaluation of the resistance to carbonation of the architectural mortar samples, the international standard method ISO/DIS 1920-12 was followed. To accelerate the carbonation process, two opposite but parallel faces from the cubic samples (10×10×10 cm) were exposed

to gaseous CO_2 in a carbonation chamber with 4% concentration (20 ℃ and 60% relative humidity), while the other four faces were sealed with an acrylic waterproof membrane (Hi-Tech 600). Prior to this exposure period, the samples were cured in water for 28 d and pre-conditioned at room conditions for another 14 d. The carbonation reaction was allowed to go on for 70 d before the samples were taken out of the CO_2 chamber for the determination of the carbonation depth by fracturing them (in transversal direction to the CO_2 flow) and spraying the fractured surface with a phenolphthalein solution.

3.9.6 Scanning Electron Microscopy and Energy Dispersive X-Ray Spectroscopy Analyses (SEM-EDX)

The samples from the powder agglomerates observed in the hardened architectural mortars and from the concrete surface layers were analysed by means of scanning electron microscopy (SEM) and energy dispersive X-ray spectroscopy (EDX) analyses. For these analyses (by element weight), a SEM JEOL model JSM-6490 at an accelerated voltage of 15 kV was used. The analytic time was 15 min for each EDX scan.

3.9.7 Quantitative X-Ray diffraction Analysis (QXRD)

The components of the photocatalytic cement pastes were determined by a high resolution powered X-ray diffractometer (XRD, Rigaku, Smartlab) using an internal standard method. Prior to the XRD measurement, samples were first crushed into small pieces and then ground in an agate mortar for about 20 min. For QXRD analysis, CaF_2 (449717-25G, Merck, Germany) was used as an internal standard to assist in the quantification of the amorphous phases. 0.800 g of ground powder was thoroughly mixed with 0.200 g of CaF_2, and the mixture was subsequently passed through a 74 μm sieve to obtain a uniformly mixed powder. The step-scanned XRD pattern measurements of each powder sample were performed using a Rigaku Smartlab diffractometer with a Cu $K\alpha_{1,2}$ X-ray radiation source (45 kV and 200 mA). The 2θ scanning range was 10~80º, and the step size was 0.02º with a scan speed of 1 s per

step. Qualitative phase identifications were executed using the PDXL software, supported by the Powder Diffraction File (PDF) database of the International Centre for Diffraction Data (ICDD PDF-2, Release 2010). The quantitative analysis was carried out using the Reference Intensity Ratio (RIR) method. As the system may contain amorphous or poorly crystalline content, a refinement method using 20% CaF_2 as the internal standard was adopted to quantify such amorphous or poorly crystalline content in the sample.

3.9.8 Diffuse Reflectance UV-Vis Spectroscopy Analysis

To assess the light absorption capacity of the different samples, diffuse reflectance UV-Vis spectroscopy analysis was carried out. The UV-Vis diffuse reflectance spectra were collected on a Varian Cary 100 Scan UV-Vis system equipped with a Labsphere diffuse reflectance accessory to obtain the reflectance spectra of the testing samples over a range of 200-800 nm. $BaSO_4$ (Labsphere USRS-99-010) was employed as a reflectance standard. The spectra were converted from reflection to absorbance by the Kubelka-Munk method.

3.9.9 Electrochemical Impedance Spectroscopy (EIS)

To evaluate the efficiency of the charge separation and transportation of different samples, EIS was measured to give a direct indication of the charge transfer resistance on the inter-surface of the TiO_2 particles and their surrounding environments. Prior to the EIS measurements, the film electrodes from the P25 and dry mixtures (containing P25, different types of cement and different dosages of Fe_2O_3) were fabricated by spin-coating the samples on a slide of conductive glass (fluorine-doped SnO_2, FTO). Square slides (50×50 mm^2) of FTO (Sigma-Aldrich, 15Ω/square) were ultrasonically cleaned in acetone, ethanol and deionized water for 30 min respectively and then dried at 60 ℃ in an oven. Coating solutions were prepared by ultrasonically dispersing 2.5 g of the sample in 100 mL of ethanol with further addition of 2.5 g glycerol. The obtained solutions were then spin-coated on the FTO glass slides. After that, the coated electrode was calcined at 450 ℃ for 2 h to burn off the

organics to achieve good electronic contact between the particles. X-Ray diffraction (XRD) analysis was performed on the 450℃ calcined sample and compared to that of the mixtures of Fe_2O_3 and TiO_2 to make sure there was no reaction under such conditions. As can be seen from Fig. 3.14, there was no discernible difference between the XRD patterns of the Fe_2O_3 and TiO_2 mixtures calcined at 450℃ and without any treatment, indicating that no reaction occurred between Fe_2O_3 and TiO_2.
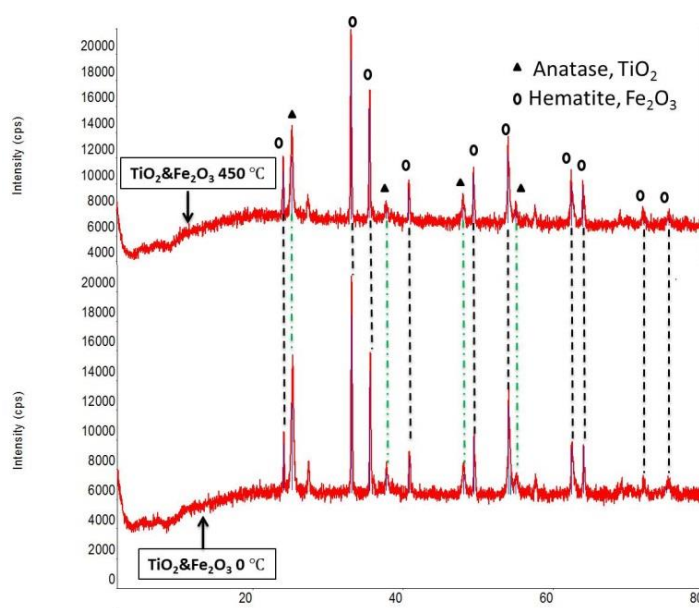
Figure 3.14 XRD patterns of mixtures of Fe_2O_3 and TiO_2 (1:1) calcined at 450℃ and without any treatment

The EIS measurements were conducted using an electrochemical workstation (Autolab PGSTAT302, Netherlands). Under an open circuit condition, a three-electrode system was adopted. The resultant electrode served as the working electrode, with a platinum wire as the counter electrode and a Ag/AgCl (saturated KCl) electrode as the reference electrode, which was performed in the presence of a 2.5 mM $K_3[Fe(CN)_6]$/$K_4[Fe(CN)_6]$ (1:1) mixture as a redox probe in 0.1 M KCl solution. The frequency range was from 100 kHz to 10 MHz. The EIS data was simulated and fitted by using Nova Version 1.7 (AutoLab, Netherlands).

3.9.10 Photoluminescence Spectra (PL)

To investigate the amount of electron-hole pairs that can be excited by photons, the photoluminescence (PL) spectra were recorded. The PL intensity at 420 nm indirectly reflects the number of photo-excited electron-hole pairs because the separated pairs will recombine to emit radiative light, which was collected and analysed by the spectrophotometer. The photoluminescence (PL) spectra were measured at room temperature using an Edinburgh FLSP920 spectrophotometer.

Combined Use of Recycled Glass and TiO$_2$ in Architectural Mortars

4.1 Introduction

Previous research work has demonstrated that incorporating glass in cementitious materials may facilitate light access to TiO$_2$. In this chapter, the combined use of recycled glass as a fine aggregate and TiO$_2$ nano-particles as an added catalyst was evaluated as a strategy to enhance the air-purifying potential of architectural mortars. The photocatalytic activities of the mortars were evaluated by assessing the NO$_x$ degradation under UV light irradiation. Furthermore, the combined use of recycled glass and TiO$_2$ on the mechanical (indicated by compressive and flexural strengths) and durability (indicated by ASR expansion and carbonation depth) properties of the architectural mortar samples were also investigated.

4.2 Consistency of Fresh Architectural Mortar Mixes

In agreement with the EFNARC, all measured diameters of the mini-slump flow were between 24 and 26 cm. It was observed that the amount of superplasticizer required to obtain the same consistency needed to be increased with the increase of TiO$_2$ content. For example, when increasing the TiO$_2$ content from 0 to 5% in the samples using glass as the fine aggregate, the superplasticizer dosage was required to increase from 2.3 to 3.2%. However, when the recycled glass was used as the fine aggregate instead of river sand, less superplasticizer was required. Overall, these results are consistent with our previous ones (Chen et al., 2012). When these nanoparticles are intermixed in the cement-based materials, they become potential nucleation sites for cement hydration products (Fig. 2.11) (Chen et al.,

2011). On the other hand, using recycled glass instead of river sand as the fine aggregate reduced the amount of superplasticizer needed to obtain the same consistency as glass particles are bigger and absorb less water than that of the sand particles (Ling et al., 2011).

4.3 Mechanical Properties of Architectural Mortars

The mechanical properties indicated by the compressive and flexural strengths are presented in Fig. 4.1 and Fig. 4.2. In Fig. 4.1, it is clear that using recycled glass instead of river sand resulted in a reduction of about 17% in compressive strength. This is most probably due to the brittleness and poor geometry of the glass aggregates used (Topçu and Canbaz, 2004). Furthermore, a gradual reduction of compressive strength was also observed when the TiO_2 content was increased from 0 to 5%.
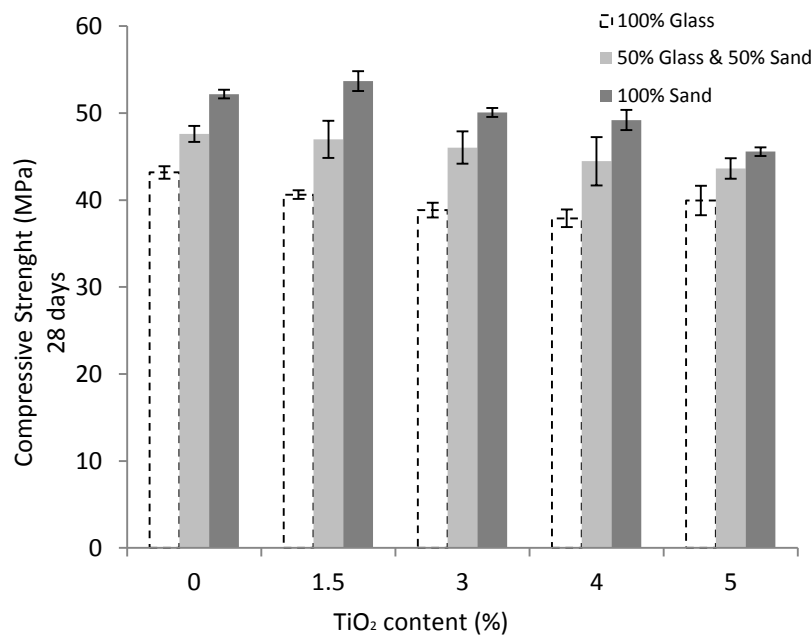
Figure 4.1 Compressive strength of architectural mortars added with TiO_2 (from 0 to 5%) and that use recycled glass, recycled glass & sand or sand as fine aggregate, respectively

As expected, a similar trend to those observed in compressive strengths was observed in relation to the flexural strengths (Fig. 4.2). Using recycled glass instead of river sand as fine aggregate resulted in a reduction of about 39% in the flexural strength. This significant

reduction was mainly due to the poor adhesion between the glass aggregate surfaces and the cement paste. Similar to the compressive strength, a gradual reduction was also observed when the TiO_2 content was increased from 0 to 5% in all the studied mortars.
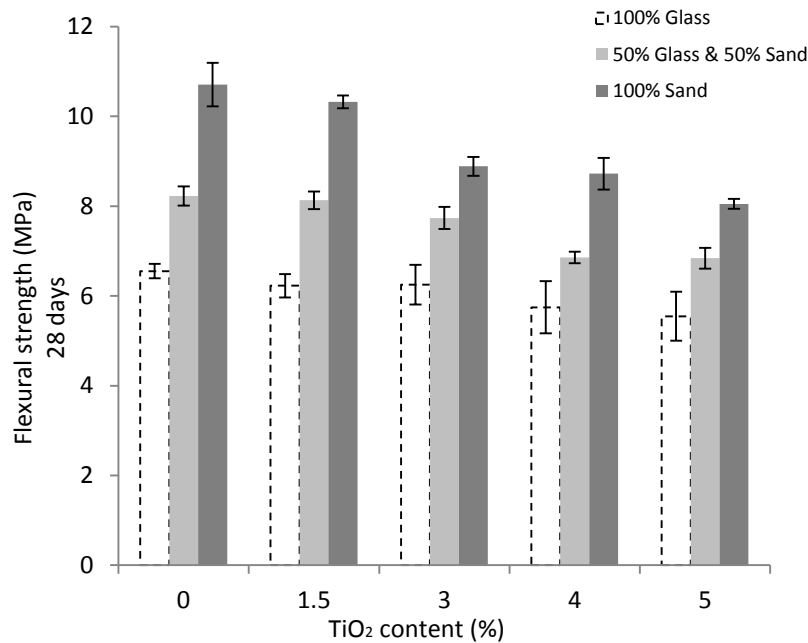
Figure 4.2 Flexural strength of architectural mortars added with TiO_2 (from 0 to 5%) and that use recycled glass, recycled glass & sand or sand as fine aggregate, respectively

The formation of powder agglomerates of several millimetres in size (Fig. 4.3 a and b) seemed to be responsible for the reduced mechanical properties of the mortar samples containing TiO_2 nanoparticles. These porous powdery agglomerates comprising TiO_2, unhydrated white cement and metakaolin particles (as identified by SEM-EDX analyses, Table 4.1) acted as points of weakness when the mortar samples were subject to the compressive stress. This phenomenon is also indirectly revealed by the increasing trend of the permeable void content observed when the TiO_2 content was increased from 0 to 5% in the prepared samples (Fig. 4.4).
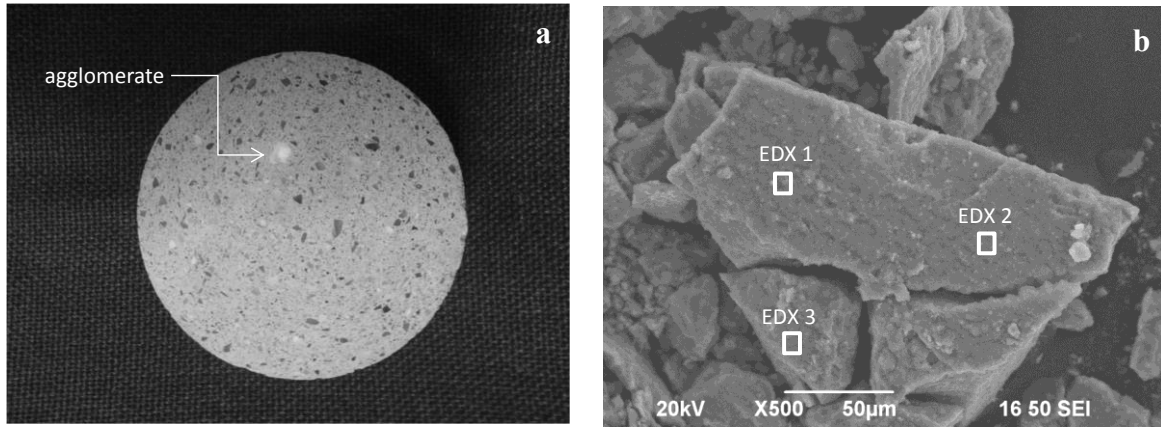
Figure 4.3 Powder agglomerates formed by TiO_2 and non-hydrated metakaolin and white cement: (a) Picture taken from architectural mortar sample (dia. 10 cm × height 5 cm) using recycled glass and sand as aggregate and adding 5% TiO_2 and (b) SEM picture of the powder agglomerate and location of EDX analyses (Table 4. 1)

Table 4.1 Chemical elements[a] detected by EDX analyses which are present in the agglomerate (Fig. 4.3b) (Chemical elements of non-hydrated metakaolin and white cement samples are presented for comparison)

Element	Agglomerate		White Cement		Metakaolin		TiO_2	
	average	SD	average	SD	average	SD	average	SD
O	56.0	1.2	47.6	10.6	57.7	3.5	43.9	4.3
Si	2.1	1.1	8.1	4.0	22.4	1.3		
Ca	29.6	4.8	51.4	29.5	-	-		
Ti	11.2	1.9	-	-	-	-	56.1	4.3
Mg	2.1	-	1.2	-	-	-		
Al	1.3	-	6.4	7.3	19.5	1.7		
K	-	-	-	-	1.9	-		

(a): element contents by weight (%) are averages calculated from minimum 3 EDX analyses.
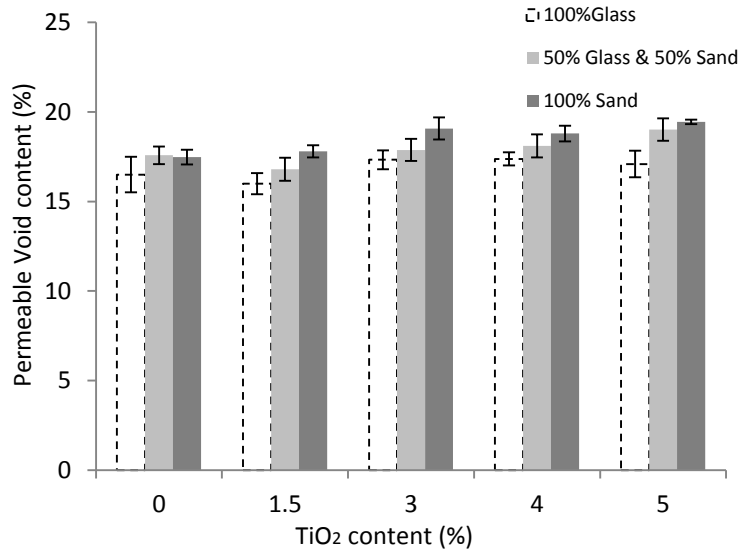
Figure 4.4 Permeable void content (%) of architectural mortars added with TiO_2 (from 0 to

5%) and that use recycled glass, recycled glass & sand or sand as fine aggregate, respectively

Moreover, the use of a high mixing rate had been demonstrated to be able to avoid the

agglomerate formation. In Fig. 4.5, the compressive strength tests performed on the mortar

samples prepared using a faster mixer (190 rpm) showed that there was no significant

difference in the compressive strengths between the samples with or without TiO_2. Moreover,

at 28 days of curing these mortar samples showed a typical compressive strength of about 50

MPa, which was higher than the equivalent group of samples with the same mix design but

prepared with the rotating pan mixer with a much lower mixing rate (16 rpm).

So, this means the extent of how the nanoparticles can be dispersed plays an important role in

affecting the performance of these novel materials, and the energy needed for particle de-

agglomeration is relatively high due to the high surface energies of the nanoparticles

(Seipenbusch et al., 2007). Further systematic research considering different mixing rates,

steps and duration should be performed to determine the optimal conditions to prepare these

novel architectural mortars.
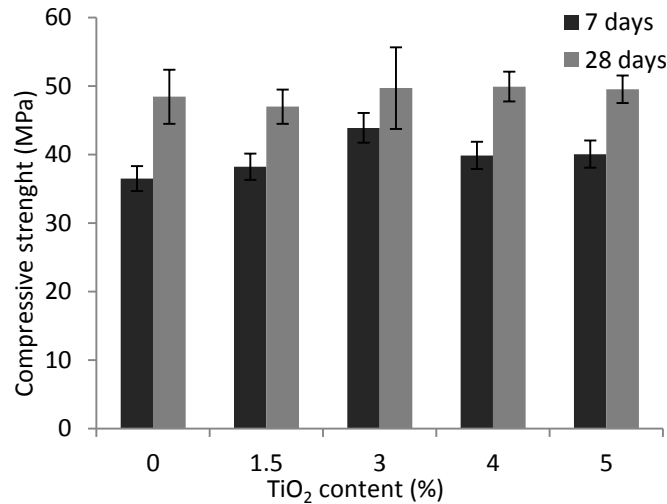
Figure 4.5 Compressive strength of architectural mortar samples using recycled glass & sand as fine aggregate and TiO_2 as added catalyst (from 0 to 5%) after 7 and 28 curing days, respectively

4.4 Durability of Architectural Mortars

Based on the potential application of these building materials, their durability properties were evaluated based on accelerated testing for measuring ASR expansions and carbonation depths.

The ASR test results are shown in Fig. 4.6 a, b and c. In all cases, the biggest expansions measured (0.03-0.04%) were below the permissible limit (0.1%) indicated by the ASTM C1260. The low expansion was possible by the addition of very fine siliceous materials such as metakaolin which neutralized the excessive alkalinity of cement with silicic acid by voluntary provoking a controlled pozzolanic reaction at the early stage of the cement setting (Terrence et al., 2000). However, slightly bigger expansions were observed when recycled glass was used in combination with an increasing content of TiO_2. This might be probably due to the presence of agglomerates (Fig. 4.3), which increased slightly the permeability (Fig. 4.4). Moreover, the insignificant ASR expansions reported here (less than 0.04%) were an important achievement considering that expansions of up to 1% (tested at similar conditions)

were registered on mortar samples prepared by partially (35%) replacing sand by recycled glass derived from pharmaceutical products, tableware production, giftware and home decoration items (Saccani and Bignozzi, 2010).
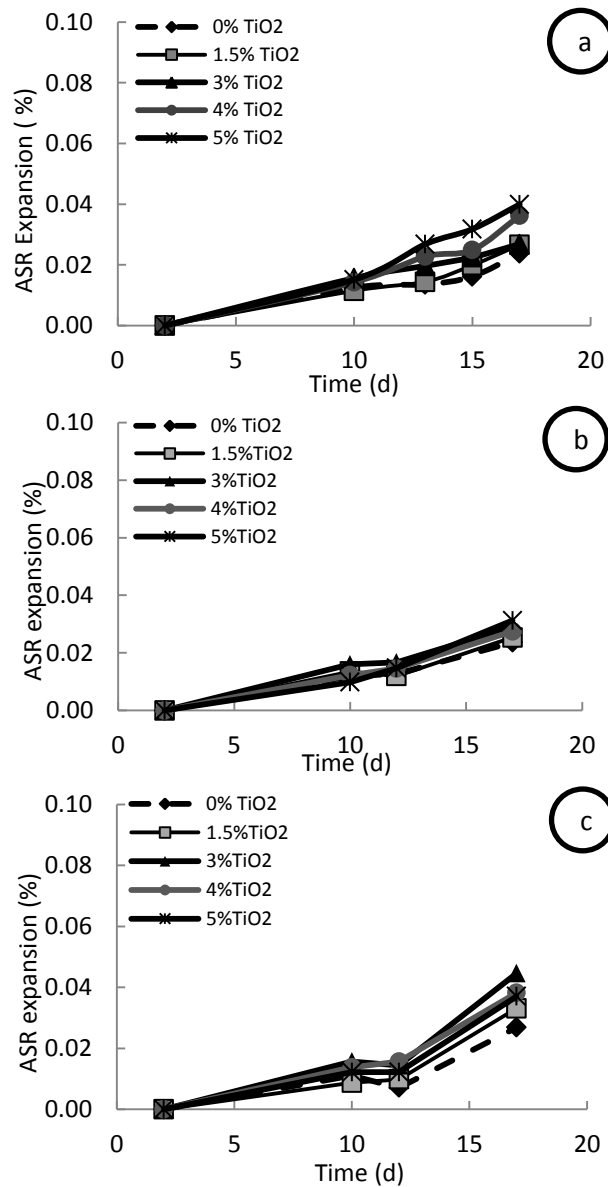
Figure 4.6 Expansions due to the alkali-silica-reaction produced during the test ASTM C 1260-07 in architectural mortars added with TiO_2 (from 0 to 5%) and that use recycled glass (a), recycled glass & sand (b) or sand (c) as fine aggregate

Although carbonation itself did not cause deterioration of the architectural mortars containing glass and TiO_2 nanoparticles, this phenomenon had important effects on the photocatalytic

activity. After 70 days enhanced carbonation as indicated in the ISO/DIS 1920-12, the carbonation depths (mm) of the architectural mortar samples are presented in Fig. 4.7. First, the results obtained from mortar samples without the photocatalyst (0% TiO_2) indicated that carbonation depth was significantly increased (7 times) by the complete replacement of river sand by recycled glass. Second, increasing the TiO_2 content up to 5% reduced the difference in the carbonation depth of the mortar samples using only recycled fine glass (100% Glass) and only river sand (100% Sand). In this case, the carbonation depth of the samples using recycled fine glass (5% TiO_2) was only 30% bigger than that of the corresponding samples using river sand. This might be due to the increase in permeable void content that facilitated CO_2 diffusion during the exposure period. However, recent experiments conducted at similar accelerated laboratory carbontation conditions (70 days) and using concrete samples containing 0, 2.5 and 5% TiO_2 evidenced higher carbonation depths (around 10 mm) (Diamanti et al., 2013).
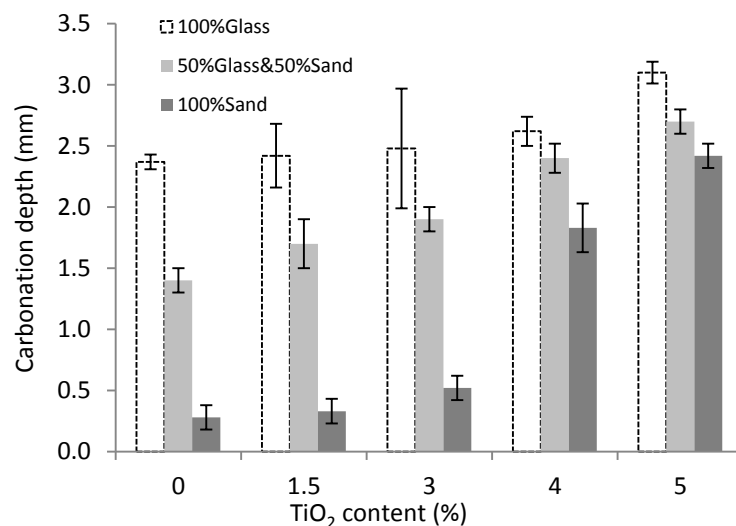
Figure 4.7 Carbonation depths of architectural mortars added with TiO_2 (from 0 to 5%) and that use, respectively, recycled glass, recycled glass & sand or sand as fine aggregate

4.5 Air-Purifying Potential of Architectural Mortar
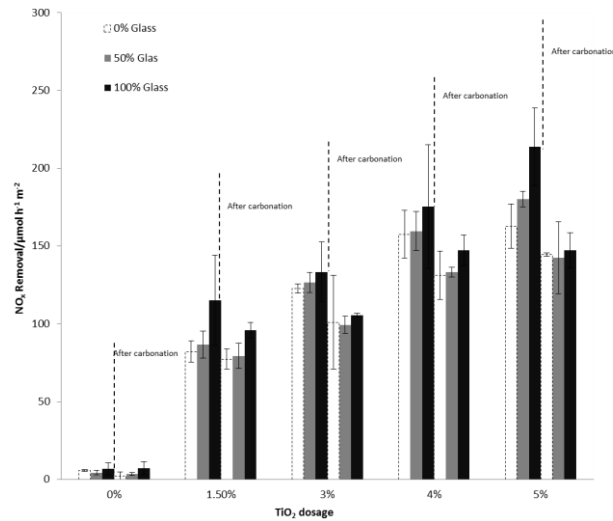
Figure 4.8 NO_x removal rates of different architectural mortars before and after carbonation

The air-purifying potentials (indicated by the NO_x removal rates) of the studied architectural mortar samples before and after carbonation (70 days) are presented in Fig. 4.8. In general, mortars samples using recycled glass and added with the highest TiO_2 contents showed the highest NO_x removal rates. However, a slight decrease in the air purifying potential was observed after the samples were carbonated. The best case which was achieved by the mortar samples containing 5% TiO_2 and using recycled glass as the fine aggregate showed NO_x removal rates of approximately 213 and 147 $\mu mol \cdot m^{-2} \cdot h^{-1}$ before and after carbonation, respectively. This reduction of about 30% after carbonation might be due to the formation of calcium carbonate ($CaCO_3$) crystals in the pores of the samples, which reduced the access of gaseous NO_x and light to the sample surface (Neville, 2011). In the literature, reductions up to 60% in atrazine degradation have been also reported after carbonation (2 months) using cement containing 10% TiO_2 (Lackhoff et al., 2003). Similarly, about 10% reduction in the degradation of RhB has been observed when concrete samples containing 5% TiO_2 were carbonated (Diamanti et al., 2013). Overall, the NO_x removal rates of the glass mortar samples containing 5% TiO_2 both before and after carbonation (213 and 147 $\mu mol \cdot m^{-2} \cdot h^{-1}$)

were significantly higher than those reported in previous works (Table 4.2). The reason to obtain these higher NO/NO_x removal rates may be associated with the increase in porosity and the presence of TiO_2 catalyst based agglomerates, which increased the potentially active TiO_2 surface area (region with access to UV-A irradiation and gaseous NO_x).

Table 4.2 NO removal rates and test conditions previously reported with cementitious materials using recycled glass as aggregate and TiO_2 as added catalyst.

Material	Cement	TiO_2 concentration & (origin)	Recycled glass	Pollutant (Inlet conc. & flow)	Operating conditions	Elimination rates ($mg \cdot m^{-2} \cdot h^{-1}$)	Reference
concrete surface layers	OPC	2, 5 & 8% (Degussa P25)	transparent recycled glass	NO (1000 ppb, 6 $L \cdot min^{-1}$)	10% RH, UV-A	2-5.	Poon and Cheung, 2006
concrete surface layers	OPC	12.5% (Ke Xiang Chemical)	2 clear, light and dark green, brown	NO (1000 ppb, 3 $L \cdot min^{-1}$)	25 °C, 50% RH, UV-A (10 $W \cdot m^{-2}$)	1-3.	Chen and Poon, 2009b
concrete surface layers	OPC	5 & 10% TiO_2 (Degussa P25)	-	NO (400 ppb, 3 $L \cdot min^{-1}$)	25 °C, 50% RH, UV-A (10 $W \cdot m^{-2}$)	3.7-4.1[a]	Chen et al., 2011
self-compacting glass mortars	WC	2 & 5% TiO_2 (Degussa P25)	light green, transparent glass	NO (1000 ppb, 3 $L \cdot min^{-1}$)	25 °C, 50% RH, UV-A (10 $W \cdot m^{-2}$)	1.5-2.5.	Guo et al., 2012
self-compacting glass mortars	WC	5% TiO_2 (Degussa P25)	light green	NO (1000 ppb, 3 $L \cdot min^{-1}$)	25 °C, 50% RH, UV-A (10 $W \cdot m^{-2}$)	2.5	Guo et al., 2013

(a): 80-90 $\mu NO_x mol \cdot m^{-2} \cdot h^{-1}$ are equivalent to 3.7-4.1 $mgNO_x \cdot m^{-2} \cdot h^{-1}$

4.6 Summary

In this chapter, the successful use of recycled glass as the fine aggregate and TiO_2 as added photocatalyst for increasing the air purification potential of architectural mortars was described. Removal rates of NO_x around 213 and 147 $\mu mol \cdot m^{-2} \cdot h^{-1}$ were obtained with the architectural mortar samples containing 5% TiO_2 and using 100% recycled glass as fine aggregate before and after carbonation, respectively. These removal rates were 80% higher than those reported previously for similar materials.

Moreover, although during sample preparation formation of agglomerates (several mm in diameter), which comprised TiO_2, unhydrated white cement and metakaolin, caused significant reductions in the mechanical and durability properties of the architectural mortars, the use of a significantly higher mixing rate (190 rpm) during the sample preparation has

been identified as a possible solution to minimize this problem. However, a more systematic research considering different mixing rates and duration should be performed for determining the optimal sample preparation parameters for enhancing both the photocatalytic and mechanical properties of the mortars.

Versatile Photocatalytic Functions of Architectural Mortars and Their Inter-Relationship

5.1 Introduction

Interests in the combined use of TiO_2 photocatalyts with cementitious materials to produce functional cement based photocatalytic products (PCP) have attracted increasing research attention. However, an effective method to obtain a high photocatalytic efficiency, thus multiple photocatalytic functions, is in strong demand. This chapter investigated the strategy of directly applying a TiO_2 containing paint on the surface of SCAM. Their photocatalytic activities in terms of NO_x and xylene removal, RhB degradation, bacteria inactivation and algae killing were studied and compared with 5% TiO_2 intermixed samples. Also, the effects of light resources (UVA and Sunlight) and weathering (façade weathering and carbonation) on the corresponding photocatalytic behaviour were thoroughly examined.

5.2 Effects of Light Resources on Photocatalytic NO_x Removal

The results of the photocatalytic NO_x removal test of SCAM samples coated with the TiO_2 containing paint (PC-S7) and intermixed with 5% TiO_2 (P25) under two different lighting irradiation conditions are shown in Fig. 5.1. It is evident that PC-S7 coated SCAM samples displayed a significantly higher NO_x removal efficiency than 5% TiO_2-intermixed samples under both UV-A and Sunlight irradiation conditions. This can be possibly explained by the fact that the TiO_2 particle sizes in the PC-S7 paint are ultra-fine (specific surface area=300 $m^2 \cdot g^{-1}$) compared with P25 (50±15 $m^2 \cdot g^{-1}$), meaning that larger surface areas of the active TiO_2 could be exposed to light irradiation for the PC-S7 coated samples. In addition, the

amount of TiO_2 in the paint (10% by weight of paint) was much higher than that added by the intermixing method (5% by weight of binder). For both the PC-S7 coated and 5% TiO_2-intermixed samples, a slight reduction in photocatalytic NO_x conversion was observed under the Sunlight irradiation condition compared with that under the UV-A irradiation condition. It is worth noting that the photocatalytic NO_x removal efficiency of PC-S7 under UV-A was comparable to that of TiO_2-dip-coated samples prepared in our previously studies (Chen et al., 2011; Guo et al., 2013). This is understandable considering that TiO_2-mediated photocatalysis is mainly a surface reaction, which relies heavily on the exposure of more TiO_2 particles on the surface of the host samples to the pollutants. However, compared with the TiO_2-dip-coating method, the PC-S7-brush-coating method is more advantageous in two respects. First, from a practical perspective, the PC-S7-coated samples require simpler preparing procedures and thus are more cost-effective. Second, the bonding between the TiO_2 particles and the substrates (the SCAM samples) is more robust for the PC-S7-coated SCAM. Such robustness is well reflected by a high weathering resistance ability, which will be discussed in detail in the following section. Whereas, the TiO_2-dip-coated samples were susceptible to losing their surface-coated TiO_2 particles (Guo et al., 2013).
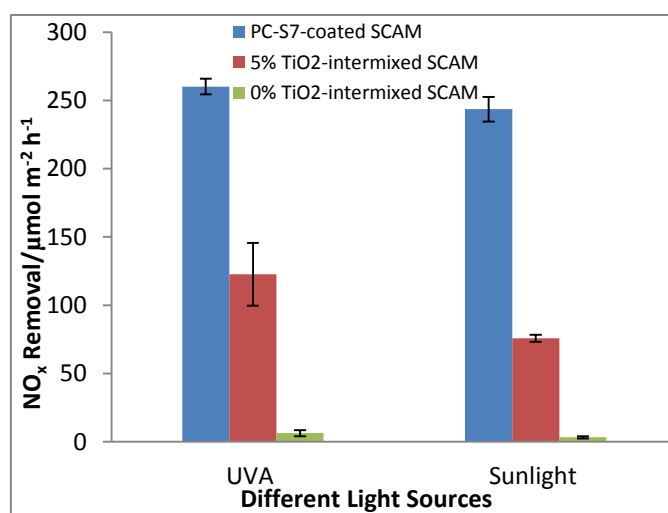
Figure 5.1 Photocatalytic NO_x removal on architectural mortar samples (PC-S7-coated and 5% TiO_2-intermixed) under UV-A and Sunlight irradiation conditions

91

5.3 Effects of Light Resources on Photocatalytic Xylene Removal

Xylene is a typical volatile organic compound (VOC), which can be commonly found in vehicle exhausts. As an organic compound, it is more difficult to be degraded compared with inorganic air pollutants such as NO_x (Chen et al., 2011). Therefore, the xylene degradation ability is a good indication of the photocatalytic efficiency of TiO_2 containing PCPs. Fig. 5.2 presents the photocatalytic xylene removal performance of PC-S7-coated and 5% TiO_2-intermixed SCAM samples under UV-A and Sunlight irradiation conditions. Similar to the photocatalytic NO_x removal, the PC-S7 coated samples possessed a considerably higher photocatalytic xylene removal efficiency under both UV-A and Sunlight irradiation conditions. For example, approximately 77% of xylene was eliminated when the PC-S7 coated SCAM was put under UV-A irradiation. In stark contrast, the 5% TiO_2-intermixed SCAM samples almost totally lost the photocatalytic xylene removal ability (nearly 0%). Apparently, for the 5% TiO_2-intermixed SCAM, a photocatalytic NO_x removal activity did not translate into a photocatalytic xylene removal activity. This finding was in good agreement with a previous study which found that under the same conditions, despite an effective degradation of NO_x, the photocatalytic conversion of toluene was not able to be achieved (Chen et al., 2011). Taken together, all the results highlight a higher requirement in the photocatalytic efficiency to obtain a satisfactory xylene degradation. Like toluene, xylene is an aromatic hydrocarbon, which consists of a benzene ring with two methyl substituents. Due to the chemical stability of aromatic rings, they are rather recalcitrant to be degraded (Bozinovski et al., 2014). Thus, compared with the NO_x removal, the xylene degradation requires a considerably higher photocatalytic activity. However, for less complex VOCs, such as formaldehyde, 5% TiO_2 in the samples was found to be sufficient to deliver a satisfactory degradation activity (Aïssa et al, 2011). The establishment of a quantitative relationship between these two photocatalytic degradation processes in the future study is needed.
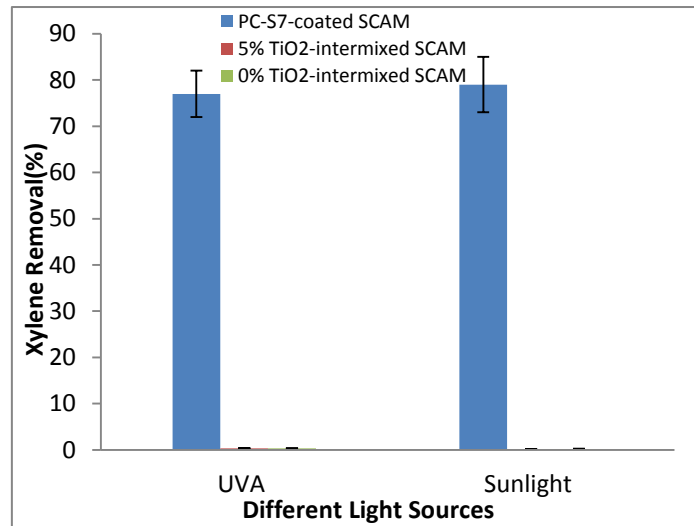
Figure 5.2 Photocatalytic xylene removal on architectural mortar samples (PC-S7-coated and 5% TiO$_2$-intermixed) under UV-A and Sunlight irradiation conditions

It is noteworthy that there was only a negligible difference in both photocatalytic NO$_x$ and xylene removal for all the samples under either UV-A or Sunlight irradiation. In this study, the UV-A intensity striking on the surface of the samples was around 2 W·m^{-2}. Such an UV-A intensity can be normally detected in a moderate sunny day. This finding demonstrated that PC-S7-coated SCAM products held great promise for outdoor applications.

5.4 Effects of Weathering on Photocatalytic RhB Degradation

5.4.1 Effect of Façade Weathering

RhB removal efficiencies on architectural mortar samples under UV-A irradiation before and after the application of a façade weathering process are shown in Fig. 5.3. Before subject to the weathering condition, the PC-S7-coated samples achieved a satisfactory RhB removal performance, with both R$_4$ (51.4%) and R$_{26}$ (63.6%) larger than the photocatalytic boundaries (R$_4$>20% and R$_{26}$>50%) (Cassar et al., 2007). In contrast, the 5% TiO$_2$-intermixed samples experienced significantly lower RhB removal efficiencies (R$_4$=4.7% and R$_{26}$=12.5%) under the same testing conditions, indicating that the intermixing method adversely impaired the

photocatalytic performance. This observed reduction in RhB removal is mainly due to the encapsulation of the intermixed TiO_2 particles by the accumulation of surrounding hydration products. Therefore, compared to the PC-S7-coated samples, the 5% TiO_2-intermixed samples are less exposed to the photons and the dye (RhB). Previous evaluation of the photocatalytic RhB removal under UV-A irradiation (1.5-2.5 mW·cm^{-2}) on white cement pastes intermixed with TiO_2 (0, 5, 10 and 15% on a weight basis) found that only samples containing 15% TiO_2 were nearly satisfactory (R_4=33.9% and R_{26}=45.8%) to be considered as photocatalytic materials (Aïssa et al, 2011).
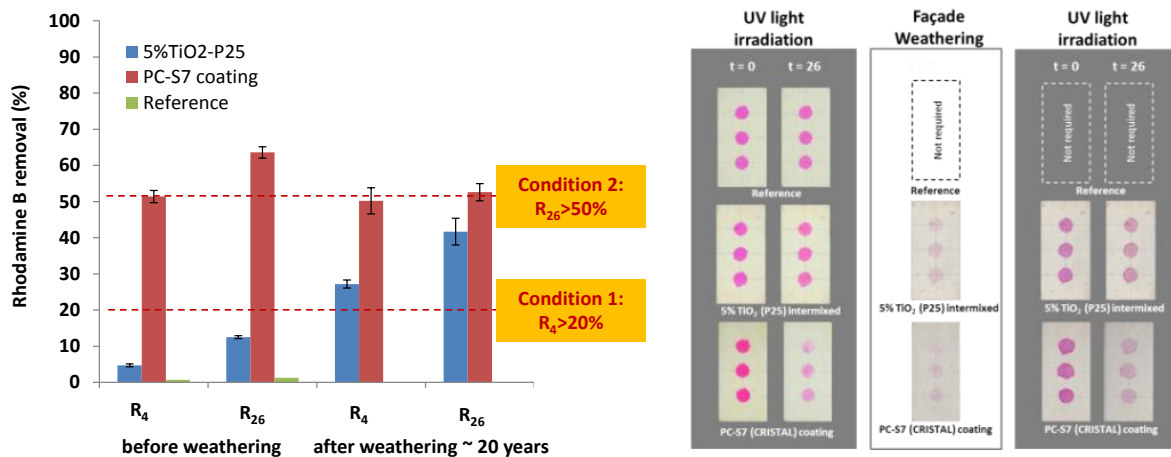
Figure 5.3 Photocatalytic RhB removal of mortar samples (PC-S7-coated and 5% TiO_2-intermixed) under UV-A irradiation before and after the application of an accelerated facade weathering process

Taken together, it seems that although the solid mass layer can form a stable support to protect the TiO_2 particles against abrasion or erosion, they may also unfavourably weaken the photocatalytic activity. This explanation was supported by a previous study which proposed that when nano-particles were embedded in cement-based materials, they could become potential nucleation sites for cement hydration products. As the hydration reaction proceeded, the hydration products (such as calcium silicate hydrate and calcium hydroxide) gradually bonded the individual TiO_2 together, forming a dense coating on the TiO_2 surface (Maury-

Ramirez et al., 2010). As for the PC-S7-coated samples, the ultra-fine particle size of TiO_2 in the paint directly translates into a much larger surface area, meaning an extended exposure to light irradiation for the active TiO_2 particles. In addition, the content of TiO_2 in the paint (10% by weight of paint) is much higher than that added by the intermixing method (5% by weight of binder). This, coupled with the fact that the coating method gives the coated TiO_2 particles much easier access to light irradiation, helps explain the above observed relatively higher RhB removal efficiencies possessed by the PC-S7-coated mortar.

It is well known that rain and wind will cause a significant detachment of the coatings on the surface of substrate materials (Goei and Lim, 2014). Thus, it is necessary to evaluate the weathering resistant ability of the developed photocatalytic products to justify their viable potential for real applications. After exposure to the façade weathering process, the PC-S7-coated samples still displayed higher RhB removal efficiencies (R_4=50.2% and R_{26}=52.6%), which satisfied the boundaries (R_4>20% and R_{26}>50%) to be considered as photocatalytic materials. On the other hand, the 5% TiO_2-intermixed samples experienced a significant improvement in the RhB removal efficiencies (R_4=27.2% and R_{26}=43.5%) after the application of the weathering process, although still not enough to satisfy the photocatalytic boundaries. It is highly likely that the weathering process helped to expose more TiO_2 particles to the photons and RhB, resulting in a higher photocatalytic RhB degradation efficiency. Thus, existing texturing surface treatments might be a good option for enhancing the photocatalytic activity of such materials. Similar results have been reported by a previous study in which an increase of about 30% and 70% on the RhB removal efficiencies R_4 and R_{26}, respectively, was observed on the 5% TiO_2-intermixed mortar samples, which were previously abraded with sand paper (P150–ISO/FEPA Grit designation) (Chen et al., 2009). It seems that TiO_2 particles do not tend to appear on the casting surface due to a lower density compared to the other cementitious materials used to prepare the architectural mortars.

5.4.2 Effect of Carbonation Weathering
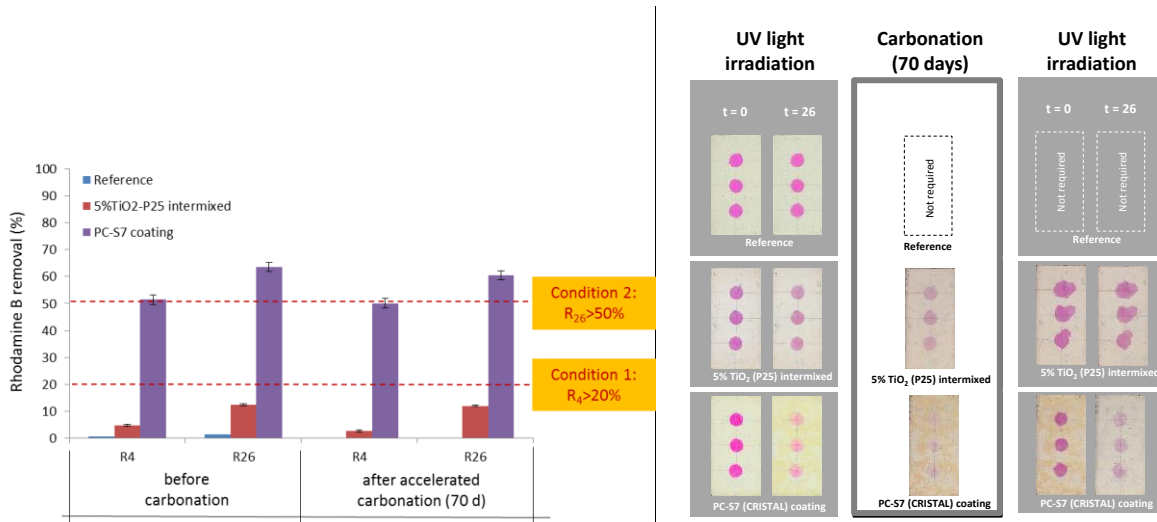
Figure 5.4 Photocatalytic RhB removal of mortar samples (PC-S7-coated and 5% TiO$_2$-intermixed) under UV-A irradiation before and after the application of an accelerated carbonation process

In the natural environments, carbonation of cementitious materials represents another concern about the long term durability of the self-cleaning ability of the architectural mortar samples. It is a slow process occurring between calcium hydroxide in the cement paste and carbon dioxide from the air (Huang et al., 2000). RhB removal efficiencies of different architectural mortar samples under UV-A irradiation both before and after the application of the accelerated carbonation weathering process are shown in Fig. 5.4. For the 5% TiO$_2$-intermixed samples, a slight reduction in RhB degradation was observed after undergoing the accelerated carbonation process. For example, the RhB removal efficiency of the 5% TiO$_2$-intermixed sample just after 4 h of UV-A light irradiation was reduced by about 45% due to the effect of carbonation. Apparently, the formation of tiny calcium carbonate (CaCO$_3$) crystals from the carbonation reaction adversely affects the contact between the RhB molecules and the surface TiO$_2$ particles. Consequently, the photocatalytic reaction is slowed down. Similar phenomena have been observed in previous studies. Reductions up to 60% in

atrazine degradation for 10% TiO_2-intermixed samples have been reported after two months of carbonation (Rincón and Pulgarin, 2007). As the carbonation can only occur between the calcium hydroxide (CH) in the substrate and CO_2 in the air, no obvious difference in RhB degradation was found in the PC-S7-coated samples before and after the carbonation process.

5.5 Photocatalytic Inactivation of Bacteria (*E. coli* K12)

Based on its above superior photocatalytic performance, the anti-bacteria activity of the PC-S7-coated SCAM was further studied and compared to that of the 5% TiO_2-intermixed sample. UVA was used as the light irradiation source.
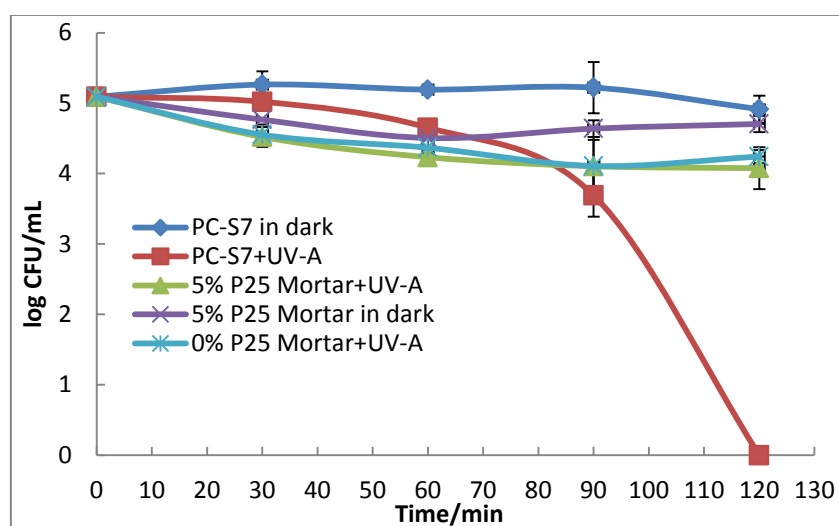
Figure 5.5 Photocatalytic inactivation of *E. Coli* K12 on architectural mortar samples (PC-S7-coated and 5% TiO_2-intermixed) under UV-A irradiation and in dark

The photocatalytic bactericidal results of the PC-S7-coated and TiO_2-intermixed SCAM samples both under UVA irradiation and in the dark are illustrated in Fig. 5.5. Without UV-A irradiation (in the dark), no detectable photocatalytic bactericidal effects on *E. coli* occurred on both the PC-S7-coated and 5% TiO_2-intermixed SCAM samples. UVA irradiation of the 0% TiO_2-intermixed SCAM also failed to deliver any detectable bacteria killing activity. Moreover, UVA irradiation of the 5% TiO_2-intermixed SCAM resulted in only a slight reduction in the concentration of *E. coli*, dropping from approximately 10^5 at the beginning to

10^4 CFU·mL^{-1} in the end. This finding was consistent with the results in our previous study (Guo et al., 2012). In contrast, the concentration of *E. coli* on the surface of the PC-S7-coated SCAM began to decrease when undergoing 60 min of UVA irradiation. After exposure to 120 min of UVA irradiation, *E. coli* was completely killed.

Our previous study has demonstrated that photocatalytic NO_x degradation and bactericidal activity are not strongly correlated with each other, and a photocatalytic NO_x degradation activity does not necessarily mean a photocatalytic bactericidal activity. Whereas, a similar study conducted by another research group found that an apparent correlation between photocatalytic decomposition of formaldehyde and inactivation of *E. coli* and established an analogy method to closely relate the formaldehyde removal to the bacterial inactivation (Chen et al., 2009). Taking into consideration the results from the current study, it seems that the photocatalytic bactericidal activity is more closely related with the photocatalytic activity of decomposing organic matter (such as xylene and RhB), but the photocatalytic NO_x removal activity cannot always be translated into either a photocatalytic organic matter degradation or a bacterial inactivation. This is understandable because it has been well known that the inactivation of bacteria is a more complex process. Oxidative damages of the cell wall and membrane, the enzymes and nucleic acids, which are mainly composed of organic compounds, are often involved in such a complicated bactericidal process (Huang et al., 2000; Rincón and Pulgarin, 2007; Lan et al., 2007; Benabbou et al., 2007).

5.6 Photocatalytic Removal of Algae (*Chlorella Vulgaris*)

Figure 5.6 illustrates the algal fouling (*Chlorella vulgaris*) results on the architectural mortar samples. After 8 testing weeks of accelerated algae fouling, both the 5% TiO_2-intermixed and the PC-S7-coated samples experienced 'slight' colour changes ($\Delta E < 1.5$) and displayed small fouled areas (fouled area<1%). And there was no obvious difference between these two types

of TiO_2 containing samples. These values ($\Delta E<1.5$ and fouled area<1%) were smaller than those observed on the reference samples ($6<\Delta E<12$; fouled area=5%). However, it should be pointed out that the magnitude of algal fouling on the reference samples was substantially smaller than those commonly observed on other cementitious materials such as autoclaved aerated concrete (Maury-Ramirez et al., 2013), indicating that the developed architectural mortar in this study had a rather low bioreceptivity (the potential of a material to be colonized by living organisms). Such a low bioreceptivity is closely associated with both the low porosity (17 ± 2%) and the small roughness (6.7 ± 0.5 µm) of the prepared architectural mortar samples.
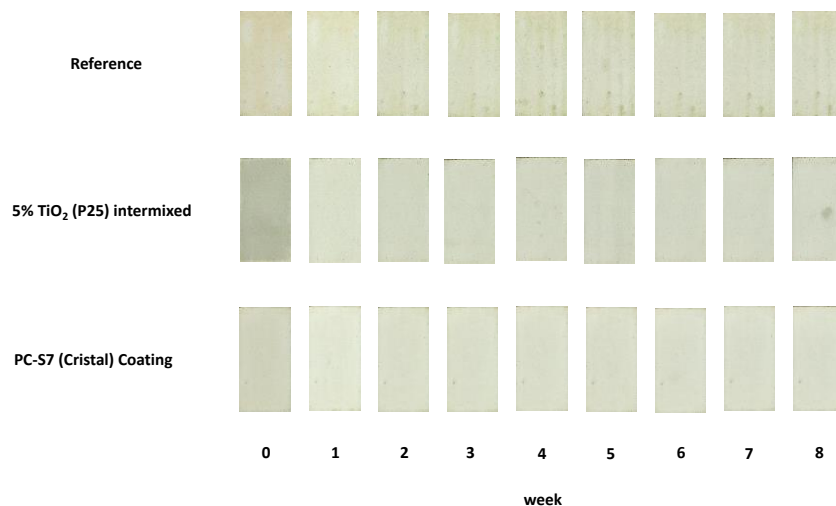
Figure 5.6 Accelerated algae fouling produced during 8 weeks on architectural mortar samples using an in-house built water run-off test set-up

5.7 Summary

In this chapter, an attempt was made to evaluate the performance of applying a TiO_2 containing paint (PC-S7) on the surface of self-compacting architectural mortars as an alternative strategy to obtain highly efficient PCPs. It was found that compared with the 5% TiO_2-intermixed SCAM, the PC-S7-coated SCAM displayed a considerably higher

photocatalytic NO_x removal efficiency. The PC-S7-coated SCAM also successfully achieved a relatively higher efficiency in both photocatalytic xylene removal and RhB degradation, while the 5% TiO_2-intermixed SCAM failed to degrade both xylene and RhB. Moreover, the PC-S7-coated SCAM achieved a total inactivation of *E. coli* after 120 min of UVA irradiation, whereas, a negligible *E. coli* killing activity was observed for the 5% TiO_2-intermixed SCAM. The superior photocatalytic activities exhibited by the PC-S7-coated samples derived mainly from the ultra-fine particle size (specific surface area=300 $m^2 \cdot g^{-1}$) and a relatively higher content (10% by weight of paint) of anatase TiO_2 particles in the paint. It seems that the photocatalytic bactericidal activity of the samples was more closely related with the photocatalytic degradation ability of the organic matter (xylene and RhB). Therefore, the photocatalytic NO_x removal activity of a sample cannot necessarily be translated into either the photocatalytic organic matter degradation or bactericidal activities. But for the anti-algae fouling activity, the porosity and roughness of the sample surface played a more prominent role than the photocatalytic activity.

More importantly, the PC-S7-coated samples also garnered a robust weathering-resistant ability, reflected by an almost unchanged ability to photocatalytic degrade RhB after exposure to a facade weathering process (representing a usage period of about 20 years under Hong Kong weather conditions), as well as an accelerated carbonation process. The overall results well demonstrated that the TiO_2 coated SCAM product can be used as an attracting product for both indoor and outdoor applications in urban environments. They are able to display several attractive functions such as air-purifying, self-cleaning, antibacterial activity and anti-algae fouling. These value-added functions can not only provide a more pleasant living condition for the urban residents but also significantly reduce the cost of routine maintenance.

Influence of Cement Types on NO$_x$ Removal and the Underlying Mechanisms

6.1 Introduction

Our previous studies showed photocatalytic cementitious materials prepared with white cement (WC) had a superior photocatalytic NO$_x$ removal performance than those prepared with ordinary Portland cement (OPC). However, the mechanisms involved still remain unclear. This chapter presents experimental results on the search for the underlying mechanisms. Considering that iron oxide is the major chemical compound that distinguishes OPC and WC, the role it plays in both the light absorption and charge separation processes was examined. Specifically, attention was focused on assessing whether the presence of a competing or synergic effect between the light absorption process and electron-hole separation activity gives WC an overall better photocatalytic performance.

6.2 Effect of Cement Types on Photocatalytic NO$_x$ Conversion

As expected, the P25-incorporated WC pastes exhibited a higher photocatalytic NO$_x$ removal rate than their OPC counterparts regardless of TiO$_2$ dosages and curing ages (Fig. 6.1). The NO$_x$ removal rate of TiO$_2$-incorporated WC pastes after 1 day of curing was approximately twice of that of the P25-incorporated OPC pastes at the same curing age. As the curing age increased, all the samples suffered a significant loss in the NO$_x$ removal efficiency. This reduction is attributed to the denser microstructure incurred by the gradual increment and accumulation of hydration products with the increasing curing age (Brandt, 2009; Chen et al., 2011).
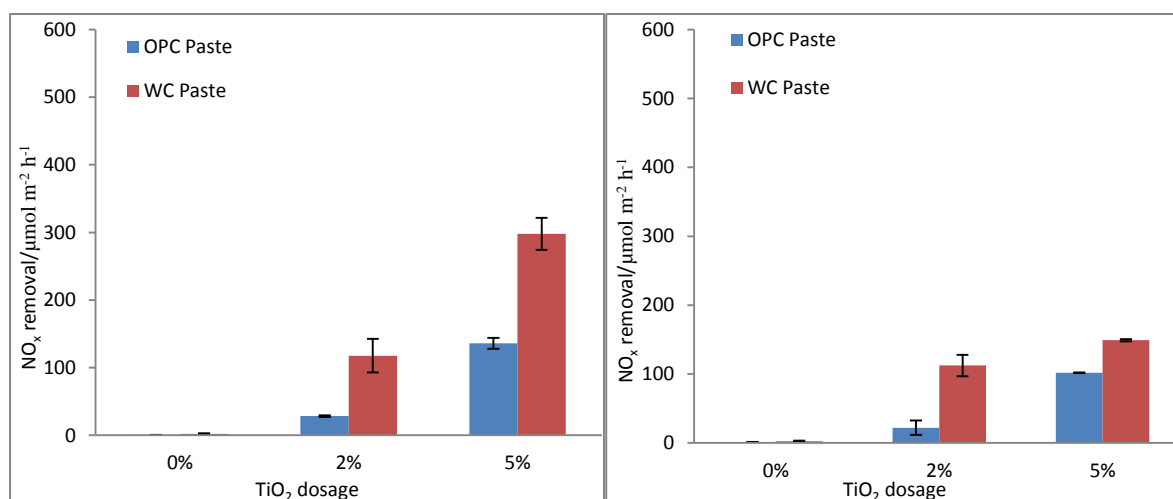
Figure 6.1 Photocatalytic NO_x removal performance of TiO_2 incorporated cement pastes hydrated at 1 (Left) and 28 (Right) days

The above results indicated that curing age did not change the trend of NO_x removal ability of the P25-incorporated WC and OPC pastes. To further examine if the accumulation of the different cement hydration products is the root cause of such observed differences, the NO_x removal performance of the WC and OPC dry mixtures blended with TiO_2 nanoparticles and without the addition of water was evaluated and compared. The results showed that TiO_2 containing WC dry mixtures outperformed OPC dry mixtures in NO_x removal as well (Fig. 6.2). But it should be noted that the difference in the removal rate between the WC and OPC dry mixtures was smaller than that between the WC and OPC hydrated pastes. It seems that although the hydration reaction did exert a certain influence on the photocatalytic activity, it was not the decisive factor that caused the fundamental difference in the photocatalytic activity. This was strongly corroborated by the XRD patterns of the TiO_2 containing pastes after the hydration process (Fig. 6.3 and Fig. 6.4). Typical anatase TiO_2 peaks can be clearly observed in both the WC and OPC hydrated pastes. More importantly, the QXRD analysis revealed that no obvious changes in the amount of TiO_2 were evident for either the WC pastes (1.4 wt.%) or the OPC pastes (1.1 wt.%), indicating that the TiO_2 was chemically inert in the pastes after the hydration process (Table 6.1). This observation, coupled with the findings

from a previous study that the amount of $Ca(OH)_2$ (CH), a hydration product of normal cement hydration, found in the pastes was also not affected by the addition of TiO_2, ruled out the possibility that the difference in the hydration processes between WC and OPC was the root cause of the difference in the observed photocatalytic activity (Chen et al., 2011). Therefore, the cement dry mixtures mixed with different dosages of P25 were used for further analysis.
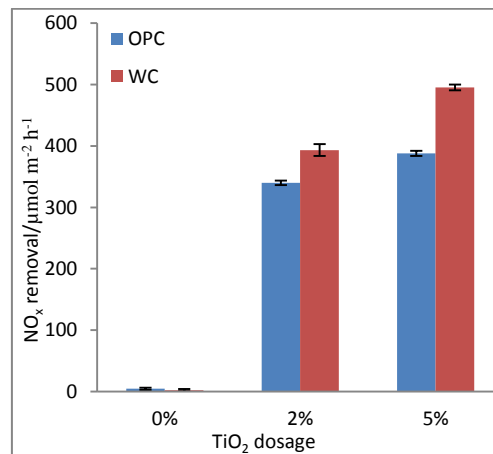
Figure 6.2 Photocatalytic NO_x removal performance of different cement dry mixtures mixed with TiO_2
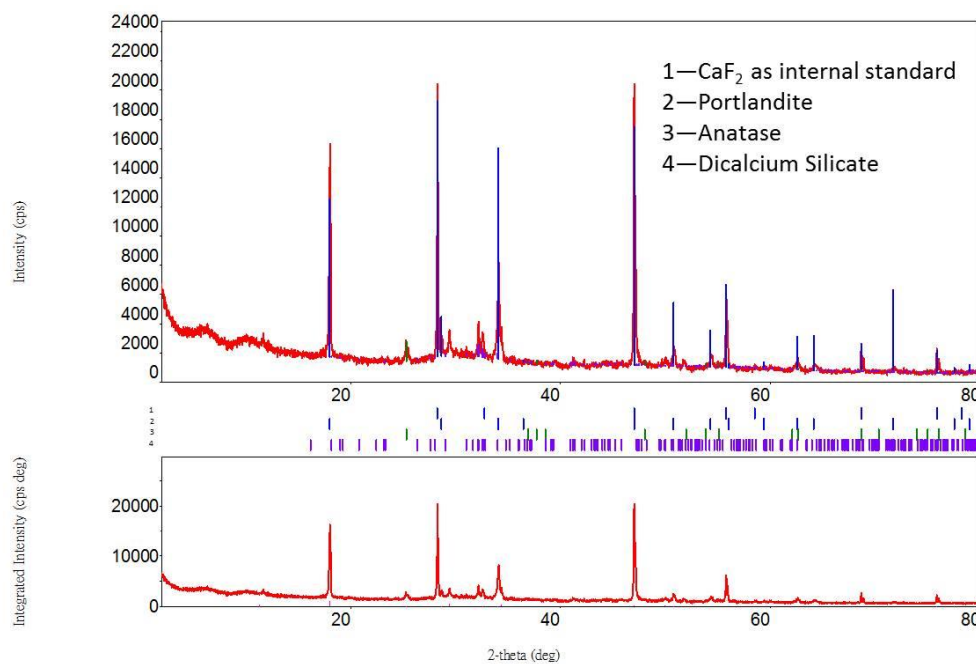
Figure 6.3 XRD patterns of OPC_10% P25 paste hydrated at 28 days
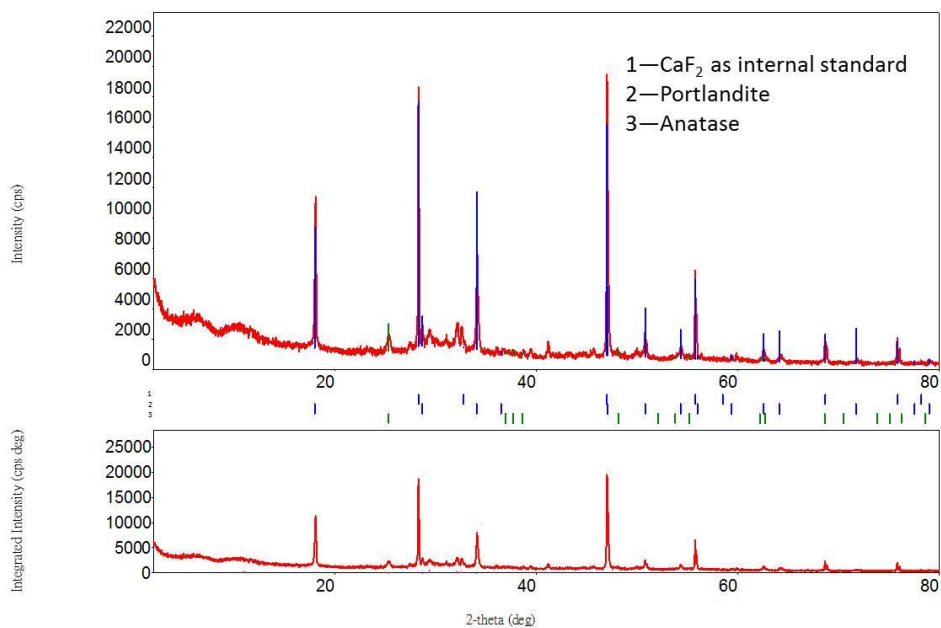
Figure 6.4 XRD patterns of WC_10% P25 paste hydrated at 28 days

Table 6.1 The results of qualitative and quantitative XRD analyses for OPC and WC pastes

with 10% TiO$_2$

Phases	OPC Pastes (wt.%)	WC Pastes (wt.%)
Fluorite	20	20
Anatase	1.1	1.4
Portlandite	14.5	16
Dicalcium silicate	5.6	-
Amorphous	58.8	62.6

Careful examination of the chemical compositions of WC revealed that the contents of iron oxide and transition metals in WC are rather low due to the use of materials that contain very little iron oxide and impurities (Table 6.2) in WC production (Neville, 2011). On the other hand, iron oxide is the principal compound that gives OPC a grey colour. Such a difference between WC and OPC raises a question of whether iron oxide and transition metals play a pivotal role in causing the corresponding difference in the photocatalytic NO$_x$ removal abilities.

Table 6.2 Physical properties and chemical compositions of OPC and WC

	OPC	WC
Physical properties		
Density (kg·m^{-3})	2960	3088
Specific Surface (cm^2·g^{-1})	3820	3660
Chemical compositions (Mass%)		
SiO$_2$	22.18	21.36
Al$_2$O$_3$	5.95	5.27
Fe$_2$O$_3$	3.37	0.2
CaO	62.46	67.49
MgO	1.56	1.14
K$_2$O	0.48	0.077
Na$_2$O	0.24	0.048
TiO$_2$	0.37	0.14
Sulphur Content as SO$_3$	2.25	2.6
Loss in ignition	0.64	1.58
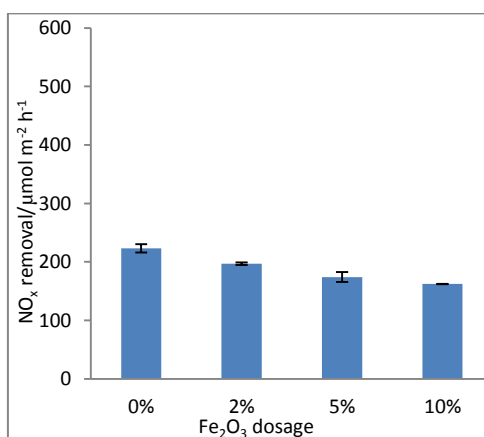
Figure 6.5 Photocatalytic NO$_x$ removal performance of WC dry mixtures with the addition of different dosages of Fe$_2$O$_3$

To answer this question, different dosages (2%, 5% and 10% by WC weight) of iron oxide (Fe$_2$O$_3$) were added as a replacement of WC to the WC/P25 (P25 at 2% by WC weight) dry mixtures, and their consequent photocatalytic NO$_x$ removal performance was investigated (Fig. 6.5). The results clearly showed that there was a descending trend of photocatalytic NO$_x$ removal rate with an increase in the Fe$_2$O$_3$ dosage. This explicitly demonstrated that the

presence of Fe_2O_3 was mainly responsible for the observed reduction in the photocatalytic NO_x removal ability in the dry mixtures of OPC and P25.

6.3 Light Absorption

The light harvest of TiO_2 directly determines the generation of electron-hole pairs and is thus of vital importance for its photocatalytic performance (Fox and Dulay, 1993). It is necessary to study the potential interference of the local environments surrounding the TiO_2 particles to the light harvesting activity of TiO_2. The measured UV-Vis diffuse reflectance spectra (DRS) of the samples are given in Fig. 6.6. The TiO_2 displayed mainly UV light absorption ranging from 200 to 400 nm, which have been well documented (Hong et al., 2011; Lu et al., 2012; Pathakoti et al., 2013). Within this wavelength range, the OPC pastes exhibited a higher light absorption capacity in comparison with the WC pastes. The same was true for the dry OPC and WC, though both had a higher optical absorption ability than their respective cement pastes counterparts. It is noted that there is an inverse relationship between the light absorption ability and the NO_x removal activity for all the samples. In other words, a lower light absorption ability of the neighbouring cement or cement paste leads to an enhancement in the photocatalytic activity. It is possible that when certain amounts of light strike the P25-blended samples, a fraction of the incident light would be absorbed by the cement or cement pastes surrounding the TiO_2 particles. Therefore, compared with OPC, WC tends to absorb less UV light and is able to reflect more light to the TiO_2 particles, resulting in a higher photocatalytic activity.

In order to investigate if a higher light absorption ability of OPC is due to the presence of Fe_2O_3, different dosages of Fe_2O_3 were added to the dry WC, and their impact on the subsequent optical absorption was evaluated. The results demonstrated that an increase in the Fe_2O_3 dosage was accompanied by an increase in the UV light absorption. Thus, it is very

likely that the relative abundance of Fe_2O_3 in OPC contributes to the elevated light absorption ability when compared with WC. It should also be noted that the influence of Fe_2O_3 on the light absorption activity mirrored its impact on the NO_x removal activity.
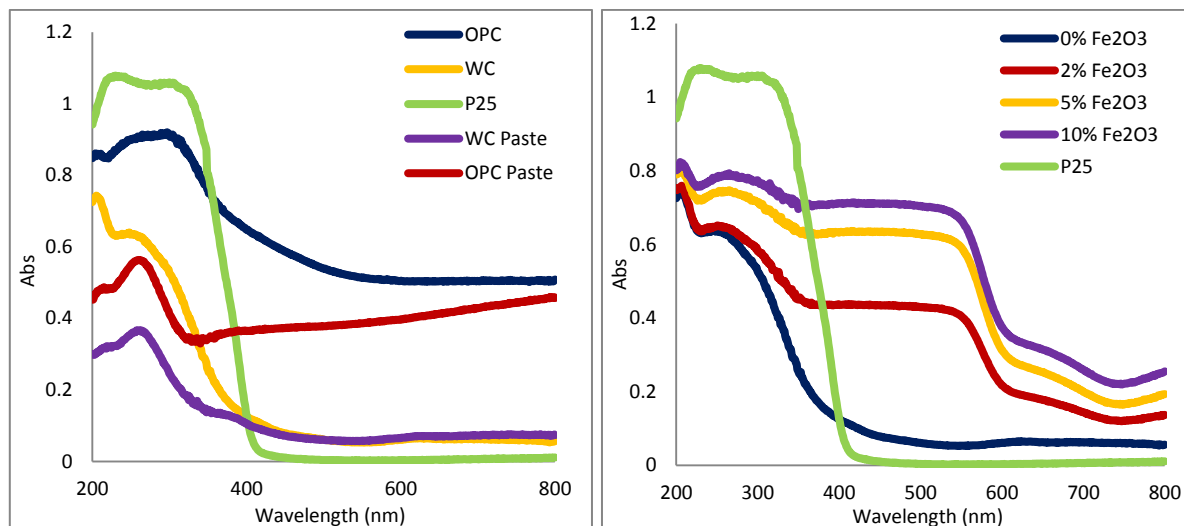
Figure 6.6 UV-Vis diffuse reflectance spectra of difference samples

Taken together, the above results corroborate the hypothesis that a distinctive disparity in the light absorption characteristic between OPC and WC is translated into the difference in photocatalytic activity. Fe_2O_3 in OPC is mainly responsible for its higher light absorption ability. It also illuminates a nuanced scenario for the influence of OPC on the light transport pathway in comparison with that of different coloured glass aggregates. For the glass aggregates, the light absorption behaviour could not only reduce the reflection of light to the surrounding TiO_2 particles, but also limit the amount of light that penetrates through the glass cullet to reach the deeper part of TiO_2 (Chen and Poon, 2009b). As for the OPC, a stronger light absorbance by Fe_2O_3 only compromises the fraction that otherwise could be reflected to the neighbouring TiO_2. The mechanism deduced from this study may apply to the case of photocatalytic variations induced by different coloured pigments (Diamanti et al., 2013; Guo and Poon, 2013).

6.4 Charge Separation

The charge separation efficiency is another important factor that is closely related to the photocatalytic activity (Hoffmann et al., 1995). The EIS measurements could give relevant information on the surface charge separation resistance of P25-blended samples (Zhang et al., 2010). The size of the semicircle in the plot is positively related to the resistance of the tested sample's surface to the charge separation and propagation. It can be clearly seen from Fig. 6.7 that the WC/P25 (5% by cement weight) dry mixtures showed a relatively shorter semicircle in the plot, which reflected a lower resistance in both solid state interface layer and the charge transfer on the surface. In stark contrast, the semicircle for the OPC/P25 mixtures was much bigger. Apparently, an expanded semicircle corresponded to a significant increase in the solid state interface layer resistance. Thus, for the WC/P25 mixtures, the electron-hole pairs could be more easily transported to the surface, and an effective charge separation can be subsequently accomplished. The successfully separated electrons and holes are expected to engage in a cascade of redox reactions. For a given amount of incident photons, an increase in efficient charge separation means a proportional decrease in electron-hole recombination. Thereby, a higher efficiency in the photocatalytic activity could be achieved. The results from the EIS measurements also corresponded well with that from the photocatalytic NO_x removal performance.

The role of Fe_2O_3 plays in OPC was once again confirmed in the charge separation process. Adding Fe_2O_3 to the dry WC led to an increase in the size of the semicircle, suggesting that its presence in OPC could impede the separation of electron-hole pairs. This influence was also mirrored by the changes in the photocatalytic NO_x removal efficiency. Compared with the more obvious difference in the semicircle size between the WC/P25 and OPC/P25 mixtures, however, the size changes in the semicircle incurred by the addition of Fe_2O_3 in WC were less evident. The semicircle of the 5% Fe_2O_3 (by cement weight) containing WC

was almost identical to that of the plain WC. It seems that the presence of Fe_2O_3 in OPC alone could not contribute to such a big difference in the charge separation efficiency between WC and OPC. Thus, it is highly likely that the presence of other transition metals in OPC could also play an importance role in increasing the resistance to the charge separation and transportation on the surface of TiO_2. The exact mechanisms by which Fe_2O_3 and other transition metals achieve this are not clear, but it is possible that they could create acceptor or donor surface centres that provide convenient recombination sites for the charge pairs (Allen et al., 2008; Chen and Poon, 2009c).
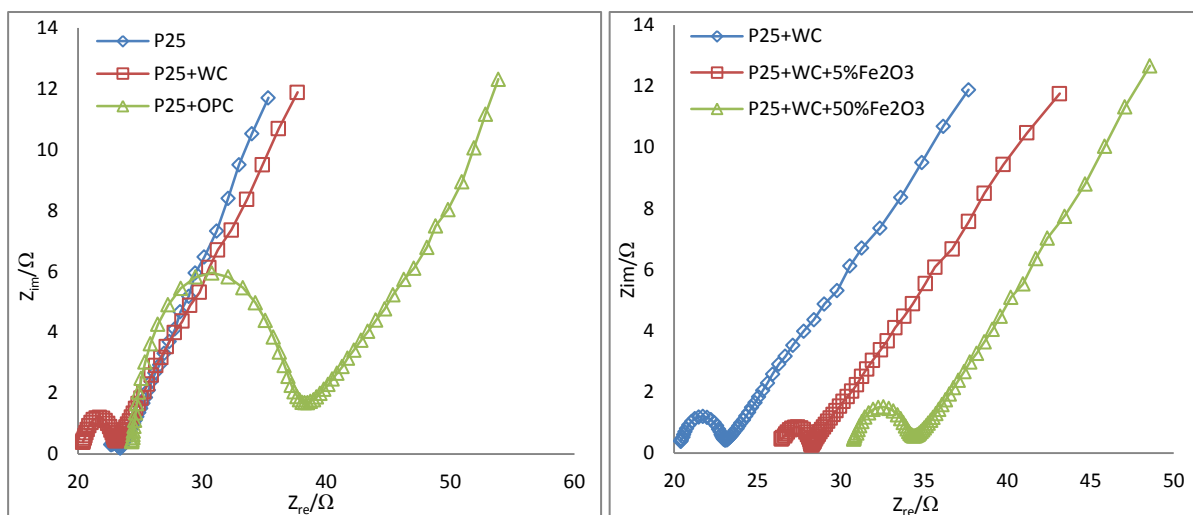
Figure 6.7 EIS changes of different samples

6.5 Overall Electron-Hole Pairs Generated and Separated

The overall electron-hole pairs that can be generated and separated by the absorption of photons are indirectly determined by means of the PL analysis. The PL spectra of different samples under an excitation wavelength of 260 nm at room temperature are summarised in Fig. 6.8. The PL emission intensity of the peak appearing at 420 nm is an indicator of the radioactive recombination of photo-excited electron-hole pairs (Kubacka et al., 2009; Pei and Leung, 2013). Under the experimental conditions in the current study where no oxygen or water molecules were provided (the sample holders were tightly sealed), the photon-excited

electron-hole pairs cannot participate in the redox reactions and will eventually recombine to emit radioactive light. Therefore, a higher PL intensity meant a larger amount of electron-hole pairs that can be excited and separated. From the PL spectra, it is apparent that the OPC/P25 (1:1) displayed the lowest PL intensity at 420 nm, while the WC/P25 (1:1) exhibited a higher one, which was only lower than that of the pure P25 sample. This provides concrete evidence that a lower light absorption and a more efficient charge separation combine to give the WC/P25 mixtures an overall more generated electron-hole pairs, which are directly reflected by the observed higher NO_x removal efficiency.

When Fe_2O_3 was introduced to the WC/P25 mixture, the PL intensity at 420 nm decreased in a Fe_2O_3 dosage-dependent manner. For example, the 100% Fe_2O_3 blended P25 mixture (WC was total replaced by Fe_2O_3) showed a greatly diminished PL intensity at 420 nm, reflecting an overall dramatic adverse effect of Fe_2O_3 on the generation of photon-excited electron-hole pairs. Taking into consideration the limited role Fe_2O_3 played in the charge separation, it is reasonable to posit that its strong ability to absorb more light (especially UV light) may be mainly responsible for its impairment on the photocatalytic activity.
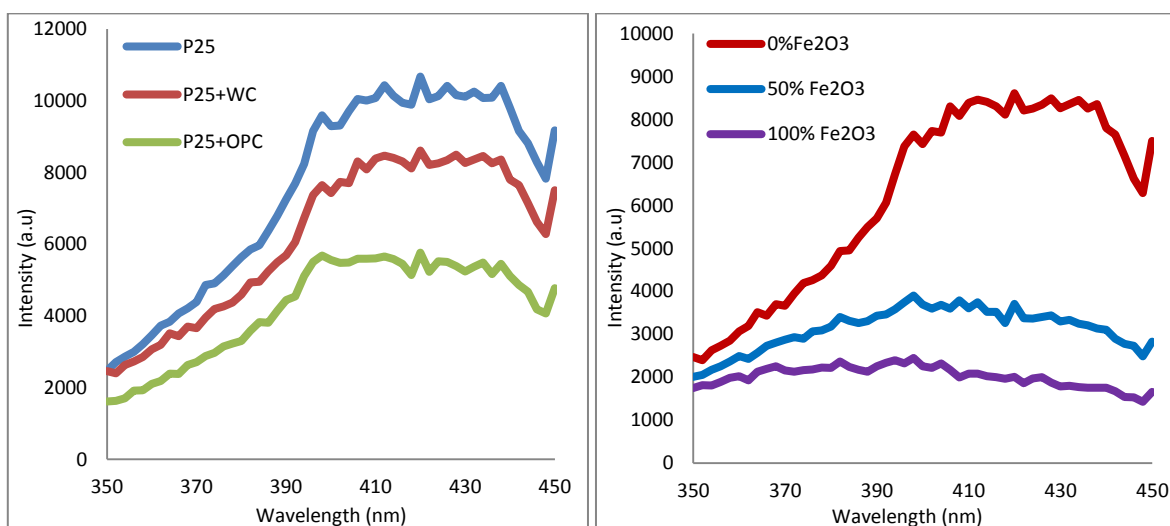
Figure 6.8 Room temperature PL spectra of the samples under excitation wavelength 260 nm

6.6 Mechanisms

Typically, TiO_2-mediated photocatalysis is mainly a three-stage process. In the first stage, electron-hole pairs can be generated upon absorption of photons with energies equal to or larger than the TiO_2 band gap. Since the photons come from the light sources (especially UV light), the access to the light irradiation is of great importance. In the following stage, the generated electron-hole pairs could either recombine to emit heat or further separate and migrate to the TiO_2 surface to participate in the subsequent redox reactions. In this process, an efficient charge separation means an elevated photocatalytic activity. The third stage involves the consumption of the separated electron-hole pairs either directly by absorbed pollutants or via chain reactions. The efficiency of the photocatalytic performance relies heavily on the first two stages. When TiO_2 is surrounded by foreign particles, its photocatalytic efficiency will be inevitably influenced by any interference in the first two stages. The observed difference in the photocatalytic NO_x removal between TiO_2-blended WC and OPC mixtures is exactly derived from their distinct behaviours in the first two vital stages (Fig. 6.9).

Compared with WC, OPC displays a much higher light absorption ability (reflected by a high DRS within the range of 200 to 400 nm). As a result, less light would be reflected to the neighbouring TiO_2 surface. With less light irradiation accessible, fewer electron-hole pairs can be generated. Even if the same amounts of light do strike on the surface of TiO_2, a stronger charge transfer resistance (reflected by a bigger semicircle in the plot of EIS) incurred by OPC encourages more electron-hole pairs to recombine rather than separate and migrate to the TiO_2 surface. These two adverse effects of OPC combine to render the OPC/TiO_2 mixtures a poor photocatalytic performance, which is directly reflected by a lower photocatalytic NO_x removal efficiency and indirectly reflected by a weaker PL intensity at 420 nm. A relative abundance of Fe_2O_3 in OPC as opposed to WC is mainly responsible for

the inferior photocatalytic behaviour. This conclusion is substantiated by the observations that all the differences between OPC and WC are mirrored by the corresponding changes incurred by the addition of Fe_2O_3 in WC.
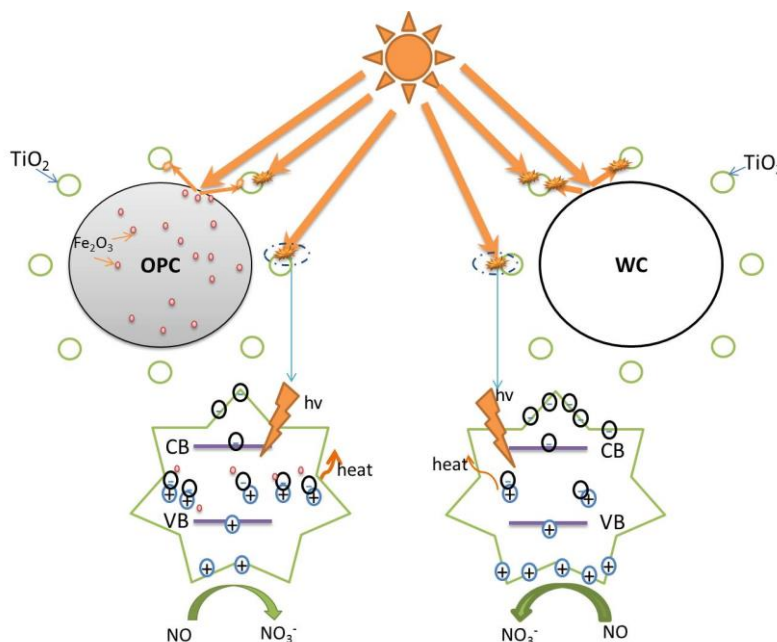
Figure 6.9 Illustration of mechanisms governing the photocatalytic difference between WC/P25 and OPC/P25 mixtures

6.7 Summary

This chapter provided the first study to provide plausible explanations to the interesting phenomenon that WC is superior to OPC in boosting TiO_2-mediated photocatalysis. Findings from this study may not only deepen our understanding of the potential interactions between TiO_2 and different types of cement, but could also shed light on other relevant phenomena, such as different coloured pigments induced variations in the photocatalytic activity of TiO_2. More importantly, the current study offers justification and incentives to further promote and expand the application of products fabricated with WC and TiO_2 photocatalysts. A more wide adoption of photocatalytic WC materials could effectively address the air pollution problems in the urban environments in an environmentally-friendly manner.

Development of Novel TiO$_2$ Incorporation Method and Influence of Experimental Factors on NO$_x$ Removal

7.1 Introduction

In this chapter, a novel method was developed to incorporate nano-TiO$_2$ into concrete surface layers (SP-Type 2). A comprehensive comparison was made with the traditional intermix (Intermixed-Type 1) and dip-coating methods (DC-Type 3). Afterwards, the SP-Type 2 and Intermixed-Type 1 samples were selected to study the effects of a wide variety of experimental factors, including NO flow rates, initial NO concentrations, UV light intensities, types of light source and relative humidity, on the photocatalytic NO$_x$ conversion. The NO$_x$ removal rate and the NO$_x$ removal ratio were calculated as two indicators to give a more comprehensive picture of the samples' NO$_x$ removal performance.

7.2 Comprehensive Comparison of Different TiO$_2$ Incorporation Methods

The photocatalytic NO$_x$ removal performance and abrasion resistant ability of samples prepared by the novel method were studied and compared with the intermixing and dip-coating methods. The results showed that the TiO$_2$-dip-coated samples (DC-Type 3) had the highest NO$_x$ removal rate before undergoing the weathering condition (Fig. 7.1), followed by the samples prepared by the spray method (SP-Type 2) and the intermixing method (Intermixed-Type 1). After 500 times of abrasion action, however, the DC-Type 3 samples suffered a significant loss in the photocatalytic NO$_x$ removal ability (a 35% reduction in photocatalytic NO$_x$ removal rate). This can be explained by the fact that there is almost no binding between the dip-coated TiO$_2$ particles and the surrounding cementitious materials,

and the TiO_2 particles on the surface are more susceptible to the abrasion action. For the Intermixed-Type 1 samples, they had the lowest NO_x removal ability before the abrasion action, and this was consistent with the findings of our previous studies (Guo and Poon, 2013). But no obvious change in the photocatalytic activity was observed after the samples were subjected to the abrasion action. This is understandable considering that the intermixed TiO_2 particles were almost uniformly distributed in the different layers of the cementitious matrix. Before subject to abrasion action, the SP-Type 2 sample showed a much higher NO_x removal rate than the Intermixed-Type 1 sample. Such a high NO_x removal efficiency was only slightly lower than that of the DC-Type 3 sample. After the abrasion action, the SP-Type 2 sample still retained a high NO_x removal ability, which was even higher than that of the DC-Type 3 sample (Fig. 7.2), displaying a robust resistance to weathering. Overall, the SP-Type 2 performed better than both the Intermixed-Type 1 and DC-Type 3 samples when taking into consideration of both the NO_x removal efficiency and weathering tolerance.

To explain the superior performance of the SP-Type 2 samples, it should be pointed out that the spray coating of nano-TiO_2 was carried out both before and after the execution of the mechanical compaction during the sample fabrication process. It seemed that those TiO_2 particles sprayed before the compaction would have more intimate contact with the surrounding cementitious materials when the compaction was applied. As the hydration reaction progressed, most of these TiO_2 particles were closely bounded to the hydration products, contributing to a robust weathering resistance (reflected by a high photocatalytic NO_x removal ability after undergoing the abrasion condition). It should be also noted that the prepared surface layers were rich in different sizes of pores. These pores could accommodate a large part of sprayed-on TiO_2 particles. Apparently, the TiO_2 particles nestling in the pores were well protected from the abrasion action. Thus, a major fraction of TiO_2 particles could remain in the pores when undergoing the harsh abrasion action. On the other hand, those TiO_2

particles sprayed on after the compaction were only relatively loosely associated with the surrounding cementitious materials, resulting in a high photocatalytic activity (reflected by the observed high photocatalytic NO_x removal ability before undergoing the abrasion condition).
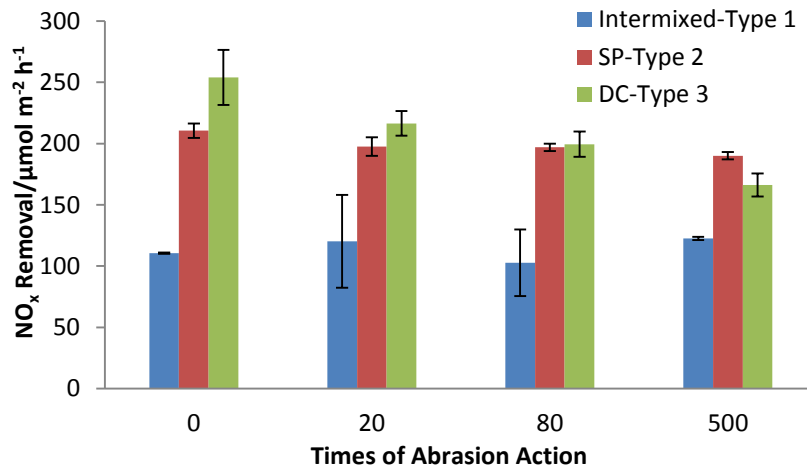
Figure 7.1 Comparison of NO_x removal rate by concrete surface layers subjected to abrasion conditions
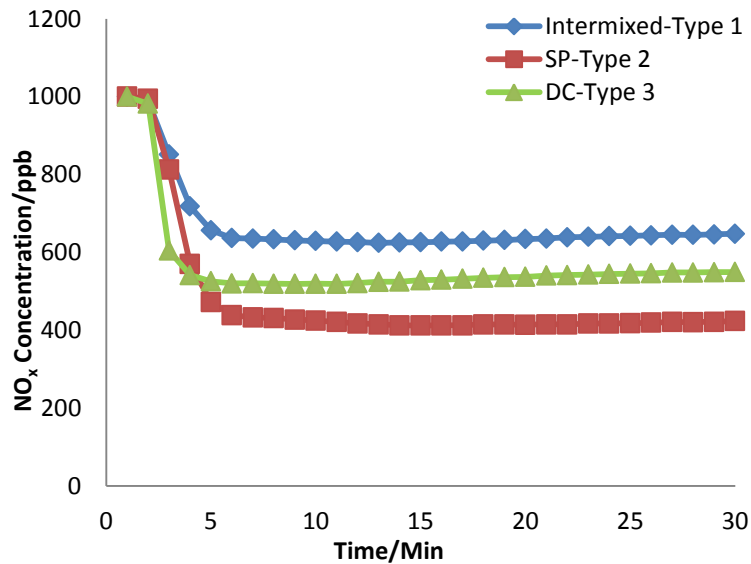
Figure 7.2 Comparison of NO_x removal rate by concrete surface layers after undergoing 500 times of abrasion action
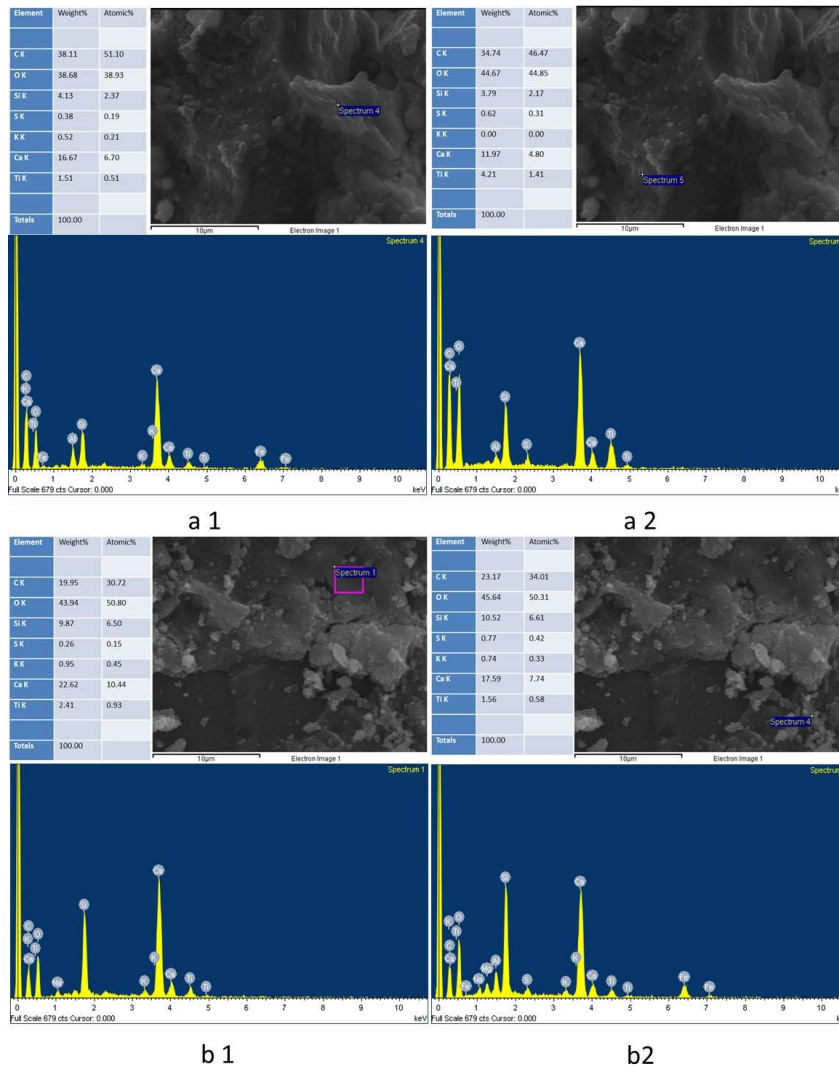
Figure 7.3 SEM-EDX analysis of TiO_2 concentrations on the surface of Intermixed-Type 1 concrete surface layers before (a 1 and a 2) and after (b 1 and b 2) exposure to 500 times of abrasion

The above assumption was well corroborated by the results from the SEM-EDX analysis. The TiO_2 content on the surface of the Intermixed-Type 1 samples was approximately 2.8% by weight without exposure to abrasion (Fig. 7.3. a 1 and a 2). After undergoing 500 times of the abrasion action, the TiO_2 contents were about 2.0% by weight (Fig. 7.3. b 1 and b 2). These results corresponded well with the observed photocatalytic NO_x degradation. As for the SP-Type 2 samples, the abrasion action caused a much higher loss of TiO_2 particles, dropping from 37.5% by weight (Fig. 7.4. a 1 and a 2) to 12.2% by weight (Fig. 7.4. b 1 and b 2). But

the results show the TiO$_2$ contents remaining on the surface of the SP-Type 2 samples were still much higher than that on the surface of the Intermixed-Type 1 samples, corresponding to a higher photocatalytic NO$_x$ removal rate observed above. However, the biggest loss (a reduction of 86%) of TiO$_2$ as a result of the abrasion action was observed on the DC-Type 3 sample (Fig. 7.5). Although the DC-Type 3 sample possessed the highest TiO$_2$ content on its surface (50.29% by weight (Fig. 7.5. a 1 and a 2)), it was reduced to only about 6.69% by weight after 500 times of abrasion action (Fig. 7.5. b 1 and b 2).
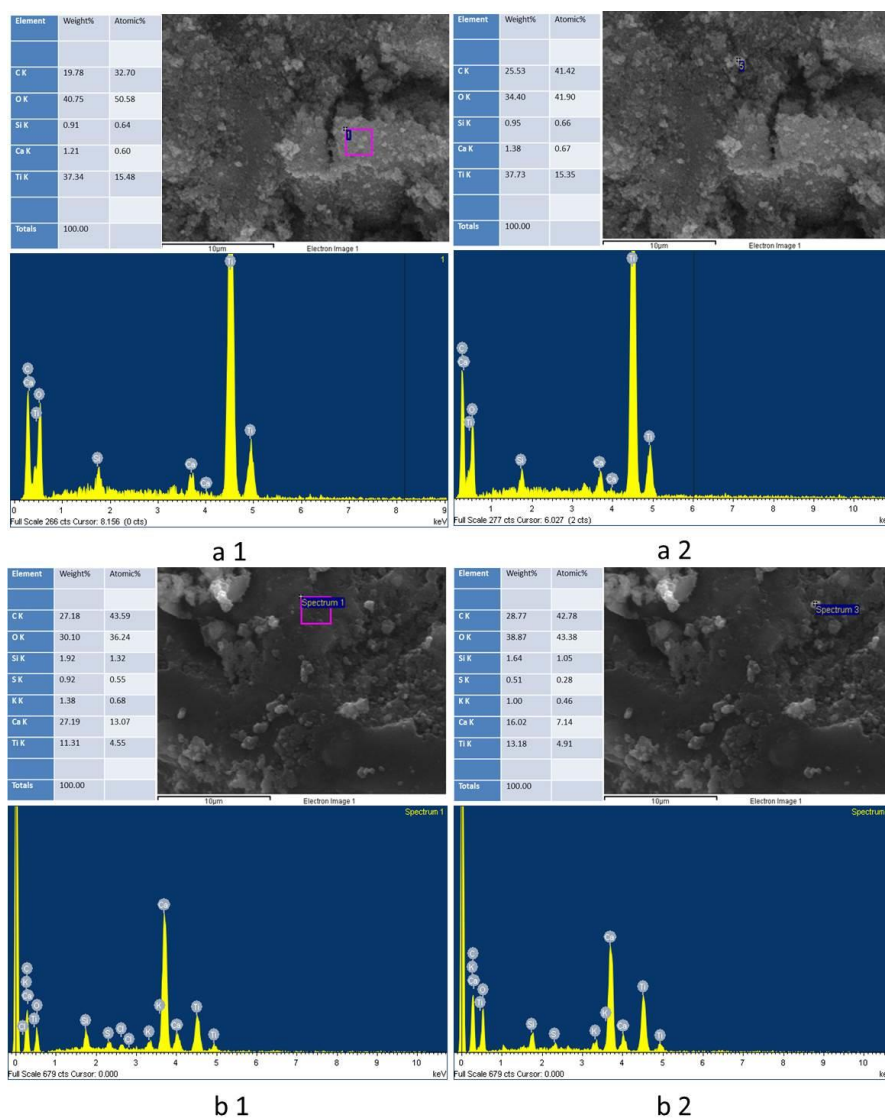
Figure 7.4 SEM-EDX analysis of TiO$_2$ concentrations on the surface of SP-Type 2 concrete surface layers before (a 1 and a 2) and after (b 1 and b 2) exposure to 500 times of abrasion
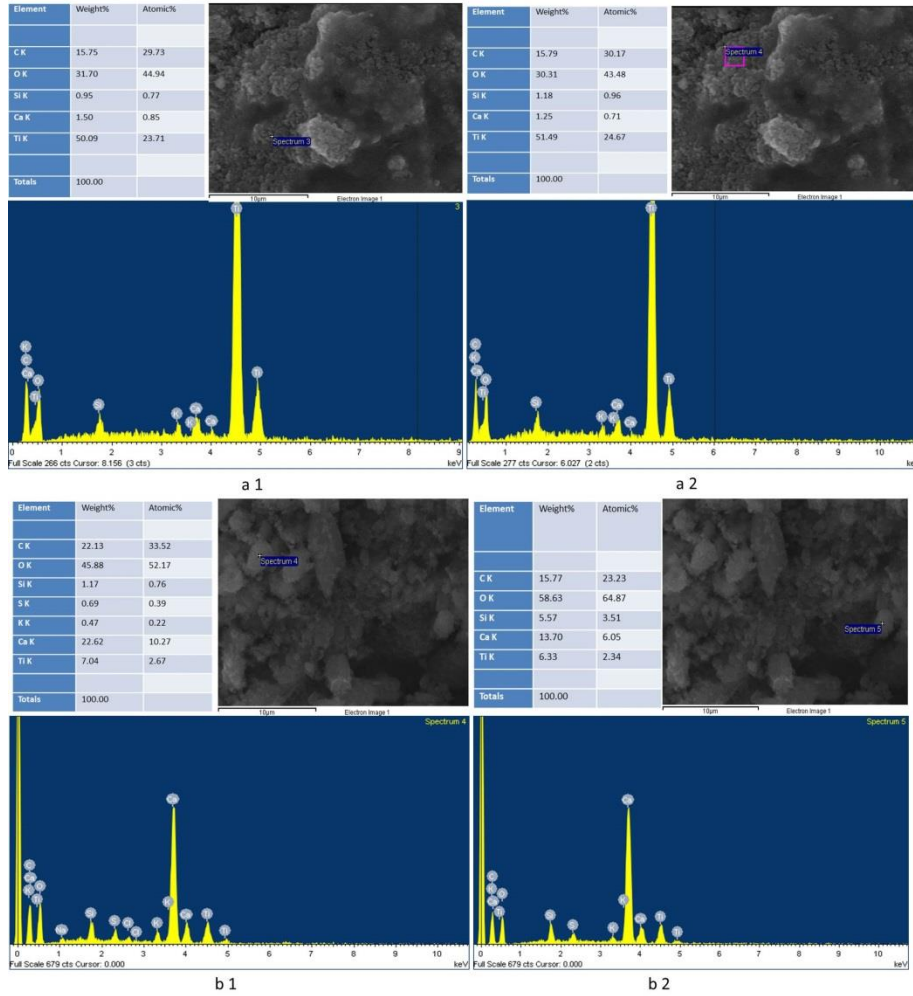
Figure 7.5 SEM-EDX analysis of TiO_2 concentrations on the surface of DC-Type 3 concrete surface layers before (a 1 and a 2) and after (b 1 and b 2) exposure to 500 times of abrasion

Table 7.1 gives a rough estimation of the efficiency and the material cost of TiO_2 for producing the photocatalytic NO_x removal concrete surface layers prepared by the three different TiO_2 incorporating methods. It can be seen that the cost of the spray method (SP-Type 2) was significantly lower (almost three times lower) than that of the intermixing method (Intermixed-Type 1); whereas, the photocatalytic NO_x removal efficiency of the concrete surface layers prepared by this method was much higher than that of the Intermixed-Type 1 samples. And after 500 times of abrasion action, samples prepared by the spray method still retained a high NO_x removal efficiency, which was significantly higher than that of samples fabricated by the intermixing method.

Table 7.1 Comparison of TiO$_2$ costs and efficiency in photocatalytic NO$_x$ removal of concrete surface layers prepared by three different TiO$_2$ adding methods

Incorporating method	Amount of TiO$_2$ (kg·m^{-3})	NO$_x$ removal rate on 28th day without weathering (µmol·m^{-2}·h^{-1})	NO$_x$ removal rate on 28th day after 500 times of abrasion (µmol·m^{-2}·h^{-1})
Intermix method	21.8	110.5	122.5
Spray method	7.5	210.5	190.0
Dip-coating Method	-	254.1	166.2

7.3 Effect of NO Flow Rate

Based on the above results, the SP-Type 2 and Intermixed-Type 1 samples were selected and compared to further investigate the effects of various experimental factors on the photocatalytic NO$_x$ removal activity. Figure 7.6 shows the effect of NO flow rate on the photocatalytic removal of NO$_x$ by the two sets of concrete surface layers under UV irradiation. The NO flow rate was varied from 0.5 to 9 L·min^{-1}. For both the Intermixed-Type 1 and SP-Type 2 samples, the NO$_x$ removal rate increased with an increase in the NO flow rate. On the contrary, the NO$_x$ removal ratio was negatively related to the NO flow rate (Fig. 7.7). These seemingly conflicting observations are probably due to the following reasons. A higher NO flow rate means a lower retention time. Therefore, the NO gas streams have less contact time with the TiO$_2$ particles, resulting in a lower photocatalytic NO$_x$ removal ratio. However, a higher NO flow rate also means that more NO gas will flow through the surface of the samples within a given time, compensating for a reduced NO$_x$ removal ratio. The combined results (a competing effect) are an increased NO$_x$ removal rate with increasing the NO flow rate. The findings in this study were not in agreement with several previous studies which found that mass transfer played a pivotal role in the photocatalytic reaction (Alberici and Jardim, 1997; Noguchi et al., 1998; Mohseni and David, 2003). When the reaction is

mass transfer controlled, the degradation rate of the reactants increases with decreasing residence time. As the contact time further decreases, the photocatalytic degradation rate changes from mass transfer control to reaction kinetic control. As a result, the degradation rate increases with the increase of residence time.
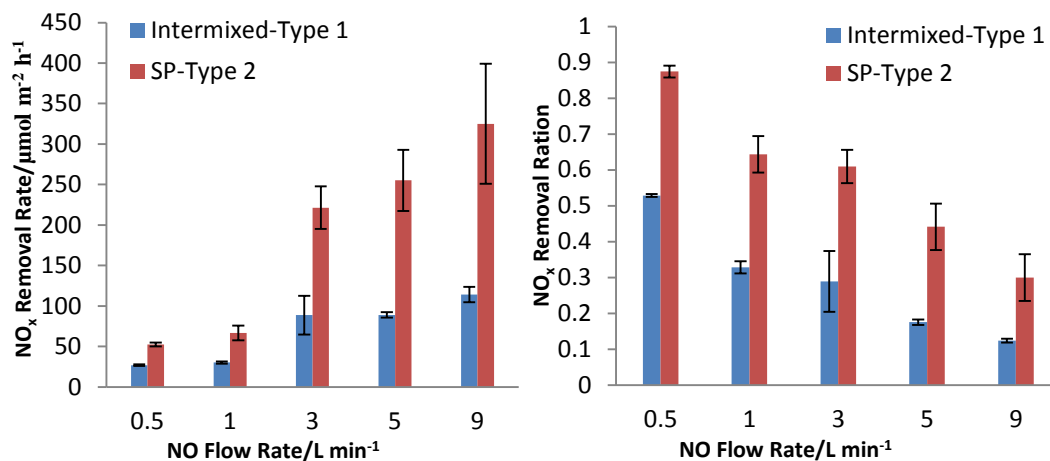
Figure 7.6 NO_x removal rate and ratio by concrete surface layers at different NO flow rates
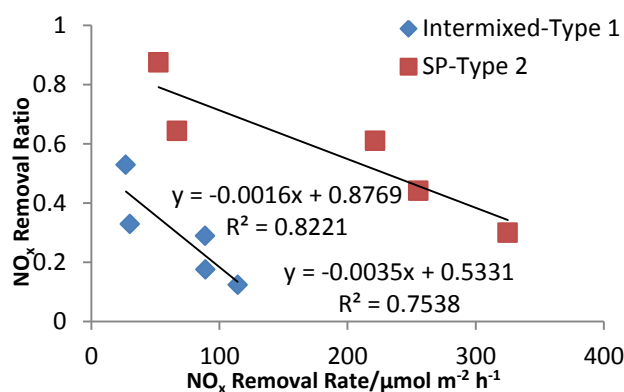
Figure 7.7 Relationships between NO_x removal ratio and NO_x removal rate at different NO flow rates

It is also noteworthy that the SP-Type 2 was superior to the Intermixed-Type 1 in terms of both NO_x removal rate and NO_x removal ratio. Apparently, the spraying-coating method could bestow more TiO_2 particles on the surface of the prepared samples. Thus, most of the TiO_2 particles have easy access to the UV light irradiation and can be activated to give a better NO_x removal performance.

120

7.4 Effect of Initial NO Concentration

The effect of the initial NO concentration on the NO_x removal of concrete surface layers is shown in Fig. 7.8. Compared to the Intermixed-Type 1 samples, the SP-Type 2 samples displayed both a higher NO_x removal rate and a higher NO_x removal ratio under all conditions. Similar to the NO flow rate, the initial NO concentration (at the studied range of 0.15-2 ppm) had a positive impact on the NO_x removal rate on the two sets of samples. In addition, an inverse relationship between the NO_x removal ratio and the initial NO concentration was also observed (Fig. 7.9). When the initial NO concentration increases, more NO gas molecules compete for the same amount of TiO_2 particles available for the photocatalytic reaction. Due to the continuous flow through experimental condition, a decrease in NO_x removal ratio occurred. On the other hand, an increase in the initial NO concentration means an increase in the total amount of NO flowing through the surface of the samples within a given time. Even though there is a decrease in the NO_x removal ratio, within the same period, the cumulative total amount of converted NO still increases (the overall outcome of the competing effect), leading to an increase in the NO_x removal rate.

The results were consistent with that of several previous studies. It was found that the reaction rate of ethylene was positively correlated with an increase in the inlet concentration from 10 to 260 ppmv (Obee and Hay, 1997). Similarly, the photocatalytic degradation rates of volatile organic compounds (VOCs) including TCE, acetone and methanol were observed to increase with increasing initial concentrations from 0.005 to 0.020 $mol \cdot m^{-3}$ (Kim and Hong, 2002). Furthermore, other studies reported that when the initial concentration of pollutants was lower than a certain level, an increased photocatalytic reaction rate was recorded with an increase in the initial concentration. When the initial pollutant concentration was relatively high, an opposite trend occurred due to the deactivation of the photocatalysts (Noguchi et al., 1998; Mohseni and David, 2003). In the present study, such an optimal concentration was not

observed within the investigated initial concentration range.
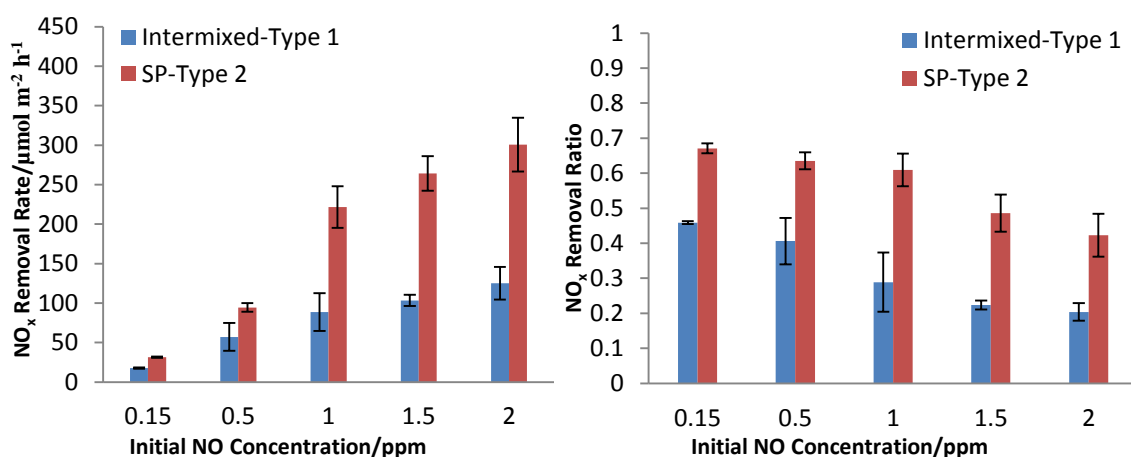
Figure 7.8 NO_x removal rate and ratio by concrete surface layers at different initial NO
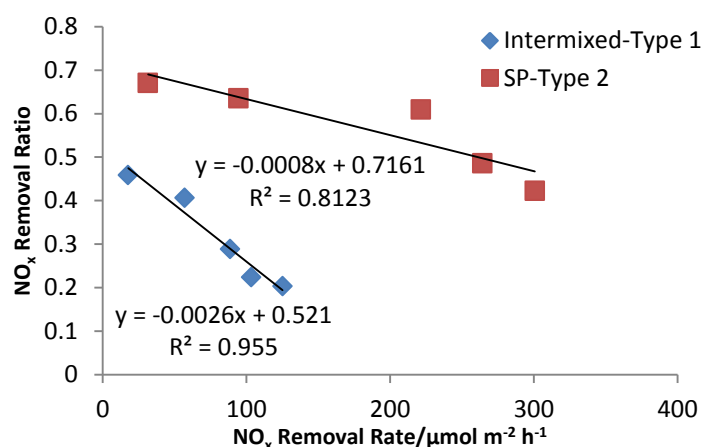
concentrations

Figure 7.9 Relationships between NO_x removal ratio and NO_x removal rate at different initial

NO concentrations

The findings from this study have, so far, demonstrated that the NO_x removal rate and NO_x

removal ratio are not always positively related to each other. Either of them alone does not

necessarily guarantee an effective reflection of the photocatalytic efficiency of the tested

samples. Thus, it is better to use both of them to give a complementing indication of the

photocatalytic behaviour of a particular material, especially when the retention time of the

gaseous pollutants in the photocatalytic reactor acts as a defining factor.

7.5 Effect of UVA Intensity

The UV light intensity is one of the most important governing factors in the photocatalytic NO_x conversion reaction. The test results of the effect of the UV light intensity on the photocatalytic NO_x removal of the concrete surface layers are provided in Fig. 7.10. It is clear that for all the samples, the NO_x removal rate gradually increased with increasing UV intensity from 0.3 to 3 $W \cdot m^{-2}$. At the lower UV light intensity range (from 0.3 to 2 $W \cdot m^{-2}$), there was a much more significant increase in the NO_x removal rate with an increase in the UV intensity. However, when the UV light intensity was raised from 2 to 3 $W \cdot m^{-2}$, the NO_x removal rate increased at a much lower rate. Unlike the NO flow rate and the initial NO concentration, the UV light intensity exerted a similar impact on both the NO_x removal rate and the NO_x removal ratio. In other words, they are positively correlated to each other for both the Intermixed-Type 1 and SP-Type 2 samples (Fig. 7.11). This is understandable because the change of the UV light intensity did not change the total amount of NO gas flowing through the reactor within a given time.

Previous studies also demonstrated similar impacts of the UV light intensity on the degradation rate of different air pollutants. For example, the reaction rate of photo-assisted degradation of ethylene by the TiO_2 photocatalyst linearly increased with increasing light intensity (Yamazaki et al., 1999). It was also reported that increasing light intensity positively enhanced the reaction rate of TCE, 1-butanol and 1-butylamine (Wang et al., 1998; Benoit-Marquie et al., 2000; Puddu et al., 2010). All these results clearly demonstrated that the UV light intensity played a positive role in a wide variety of photocatalytic activities.
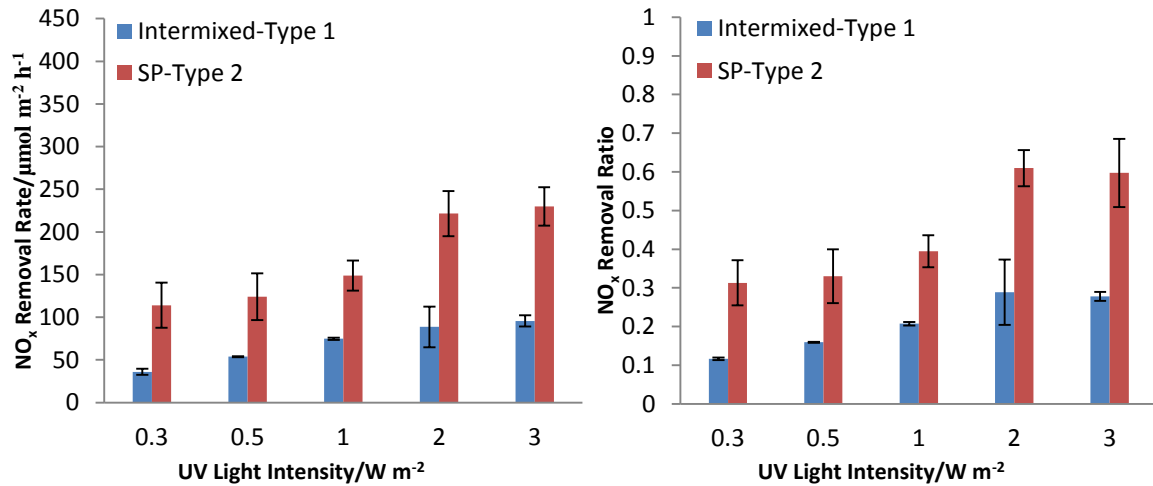
Figure 7.10 NO_x removal rate and ratio by concrete surface layers at different intensities of

UVA light irradiation
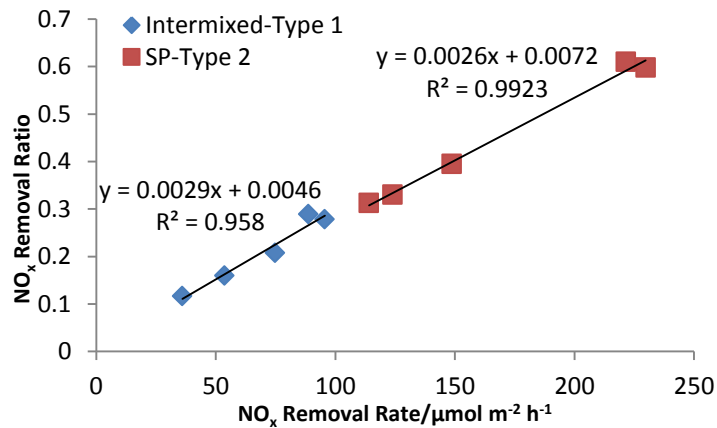
Figure 7.11 Relationships between NO_x removal ratio and NO_x removal rate at different

intensities of UVA light irradiation

7.6 Effect of Relative Humidity

Humidity plays a vital role in the photocatalytic degradation of gaseous pollutants because

several important radicals involved in the photocatalytic reactions, such as $^{\cdot}OH$ and $HO_2^{\cdot}$, are

derived from water vapour. Therefore, it is necessary to investigate the impact of humidity on

the photocatalytic NO_x degradation. Fig. 7.12 displays the effect of relative humidity on the

photocatalytic NO_x conversion of the Intermixed-Type 1 and SP-Type 2 samples. For all the

samples, both the NO_x removal rate and the NO_x removal ratio first increased (from 10% to

25%), reached a peak (at 25%) and then decreased (from 25% to 80%) as the relative humidity continued to increase. It should be noted that the NO_x removal rate of all the samples at 10% RH was higher than that at 60% RH. Under different RH circumstances, a positive relationship between the NO_x removal rate and the NO_x removal ratio was observed again (Fig. 7.13). It is apparent that when the retention time of the gaseous pollutants in the photocatalytic reactor is not a variant, the two indicators correspond well to each other. In such cases, either of them is sufficient enough to give an accurate indication of the photocatalytic behaviour.
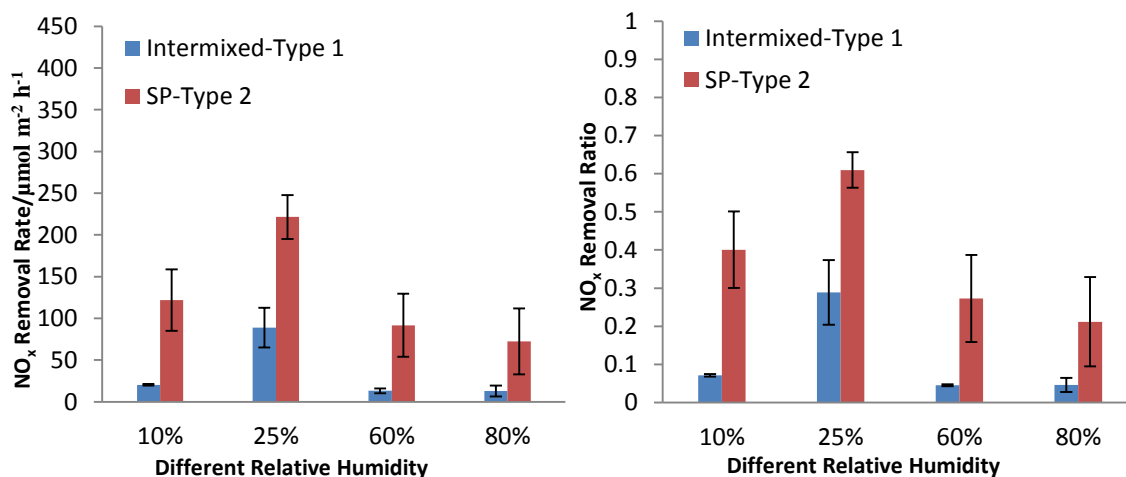
Figure 7.12 NO_x removal rate and ratio by concrete surface layers at different relative humidity
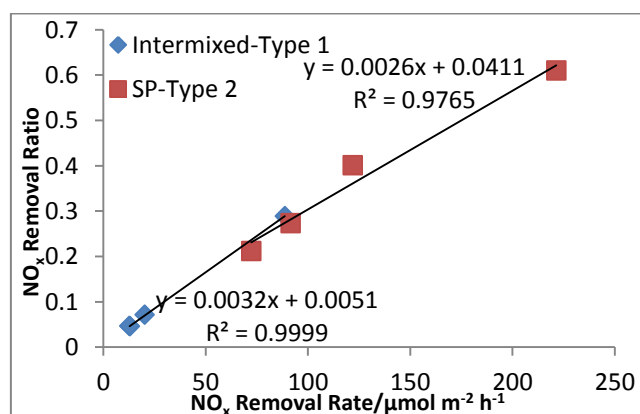
Figure 7.13 Relationships between NO_x removal ratio and NO_x removal rate at different relative humidity

125

These findings are consistent with that of the previous studies which also found that the photocatalytic degradation rate of air pollutants increased to a peak with increasing RH and then decreased gradually (Obee and Brown, 1995; Demeestere et al., 2005). Although the previous studies pointed out that the number of hydroxyl radicals generated on the surface of the photocatalysts was proportional to the adsorbed water molecules under UV irradiation, the effects of RH levels on the photocatalytic degradation rate were more complex (Boonstra and Mutsares, 1975). It is highly likely that at a lower RH, increasing humidity levels led to the generation of more hydroxyl radicals, which could be subsequently utilized by the TiO_2 to degrade more air pollutants, hence resulting in the observed increase in the NO_x degradation rate. However, when there was excess water vapour, the light blocking effect of the water vapour became more dominant as the water layers began to accumulate on the surface of the photocatalyst and adversely decreased the NO_x degradation rate (Ballari et al., 2011). Moreover, at a high relative humidity a competition between NO and water molecules will also come into play.

7.7 Effect of Spectra of Light Sources

Five different light sources were used in this study to examine the effect of different light spectra on the photocatalytic NO_x removal efficiency (Table 3.4). As shown in Fig. 7.14, the NO_x degradation rate and NO_x removal ratio of both the Intermixed-Type 1 and the SP-Type 2 samples were much higher under irradiation of UV-A than the other light sources (expect for SL, under which a comparable NO_x removal rate was obtained). It is also noteworthy that a relatively high NO_x removal efficiency was attained under LED irradiation (wavelength between 405 and 410 nm). Apparently, higher NO_x degradations were recorded for light irradiation near the UV range. The results suggest that a satisfactory photocatalytic NO_x removal performance can be expected when the TiO_2 containing concrete surface layers are

used under outdoor conditions. But the effectiveness of indoor applications is limited.
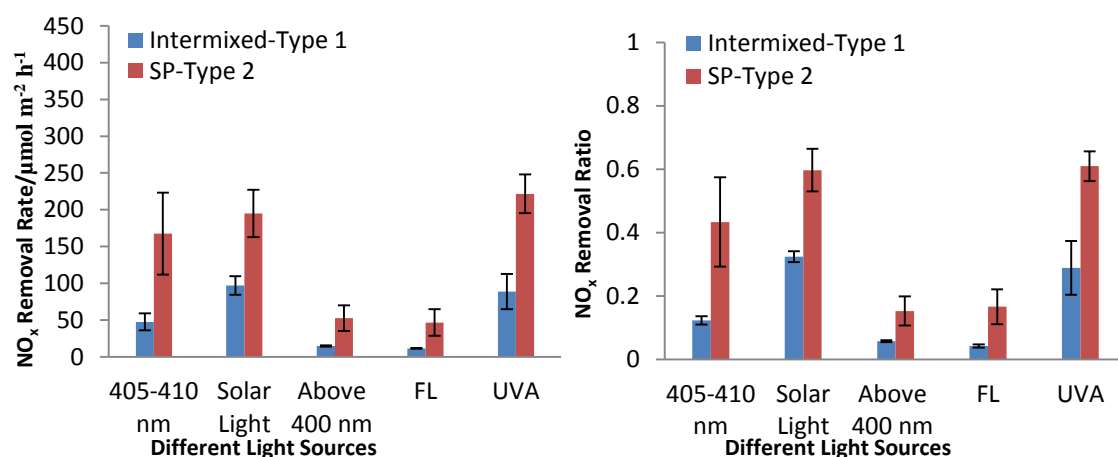
Figure 7.14 NO$_x$ removal rate and ratio by concrete surface layers at different spectra of lights irradiation

7.8 Summary

This chapter developed a novel method to produce photocatalytic concrete surface layers with a high efficiency and a low cost. Such designed products were found to hold various advantages over those prepared both by the intermixing and dip-coating methods. And thereafter, the effects of different experimental factors on the photocatalytic NO$_x$ removal performance of the Intermixed-Type 1 and SP-Type 2 concrete surface layers were thoroughly investigated. It has been clearly demonstrated that the SP-Type 2 samples outperformed the Intermixed-Type 1 samples in terms of photocatalytic NO$_x$ degradation under all the investigated conditions. Both the NO flow rate and initial NO concentration had a positive impact on the NO$_x$ removal rate but a negative influence on the NO$_x$ removal ratio. The UV light intensity had a positive relationship with both the NO$_x$ removal rate and the NO$_x$ removal ratio, while the NO$_x$ removal efficiency first increased, reached a peak, and then decreased with increasing the relative humidity. The photocatalytic activity of the TiO$_2$ containing concrete surface layers was most effective under UV irradiation, but a comparable NO$_x$ removal rate was also observed under SL irradiation. The overall findings well

demonstrated that the newly developed spray-coating method is simple to operate and requires a much lower material cost, while the resulting products possessed both a robust weathering resistance and a high NO_x removal efficiency, showing promising potential for practical applications.

Influence of Environmental Factors on NO_x Removal of Surface Layers Intermixed and Spray-Coated with TiO_2

8.1 Introduction

The negative effect of contaminating substances on the NO_x removal effectiveness of photocatalytic surfaces in real-life service, as well as their recovery capacity after undergoing cleansing processes is of real academic and practical interest. In this chapter, the NO_x removal effectiveness of two different types of photocatalytic concrete surface layers incorporated with nano-TiO_2 particles (Intermixed-Type 1 and SP-Type 2) was examined before and after being subjected to dust accumulation and oil impregnation. The recovery of their NO_x removal capacity after undergoing various cleansing processes was also evaluated, and the results were compared to those of their respective reference samples.

8.2 Photocatalytic NO_x Removal

Figure 8.1 illustrates the NO_x concentration profiles when the reference Intermixed-Type 1 and SP-Type 2 samples were subjected to the test. The SP-Type 2 samples showed a greater capacity to reduce the NO_x. This finding was consistent with that in chapter 7. The elimination rate of NO_x by the Intermixed-Type 1 and SP-Type 2 samples were 136.5 $\mu mol \cdot h^{-1} \cdot m^{-2}$ and 255.0 $\mu mol \cdot h^{-1} \cdot m^{-2}$, respectively. Thus, the SP-Type 2 sample was 80% more effective than the Intermixed-Type 1 samples. Such a superior NO_x photocatalytic removal performance delivered by the SP-Type 2 samples can be attributed to a much higher amount of TiO_2 particles on the sample's surface (supported by the following SEM-EDX analysis). As a result, most of the TiO_2 particles residing on the surface were able to gain easy access to

the UV light irradiation. In contrast, a high percentage of nano-TiO_2 particles presented in the Intermixed-Type 1 samples were completely surrounded by the hydration products and hence were not in direct contact with the UV-light, as was previously described (Guo et al., 2013).
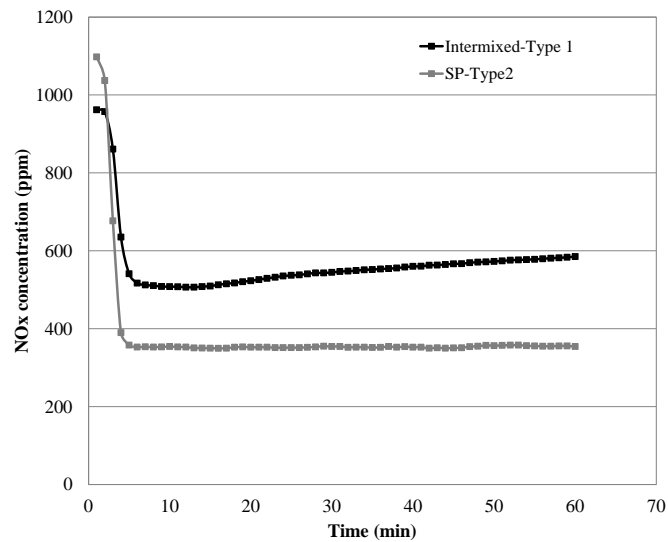
Figure 8.1 Photocatalytic NO_x removal profiles of Intermixed-Type 1 and SP-Type 2 samples
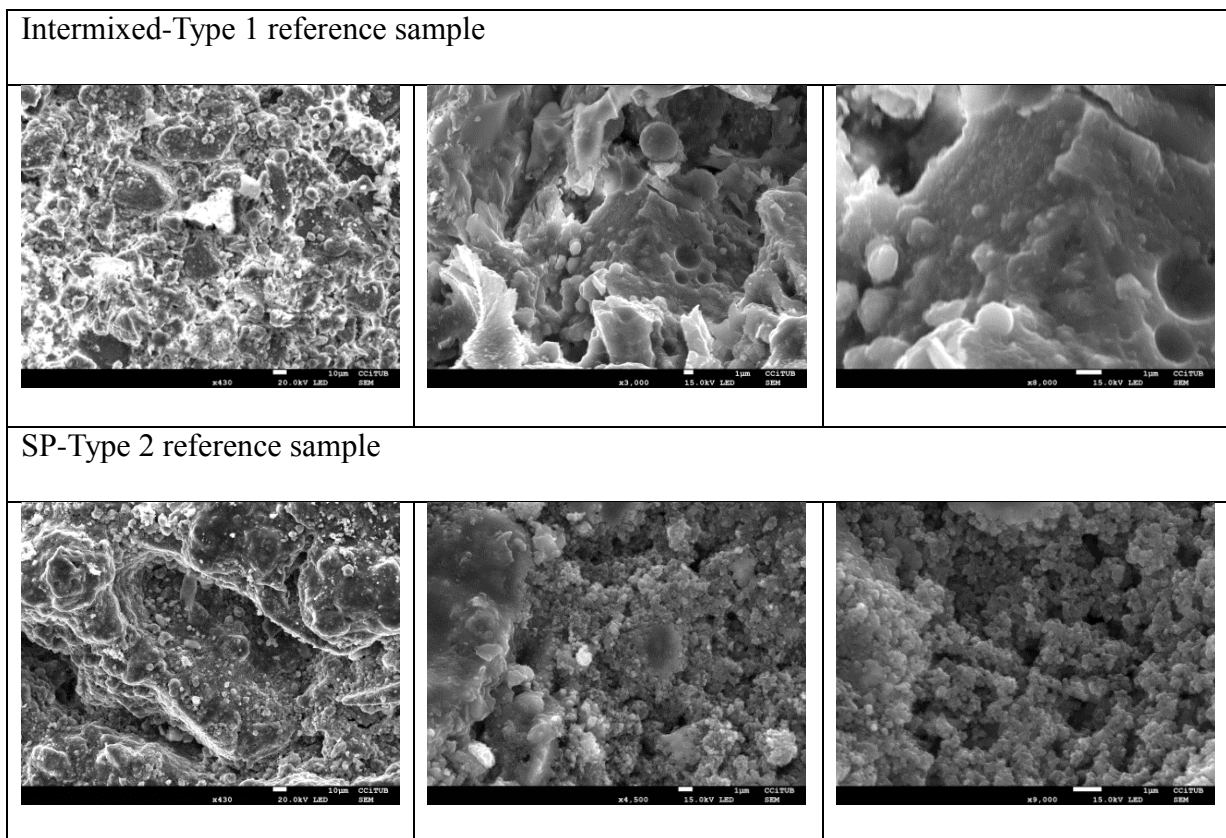
Figure 8.2 SEM morphology of the two types of concrete surface layers

The two types of samples were analysed by SEM and EDX. Fig. 8.2 clearly illustrates the

morphological differences of the two samples studied. And the EDX analysis revealed that the percentage of titanium element presented on the surface of Intermixed-Type 1 and SP-Type 2 samples was 3.3% and 26.4%, respectively. Fig. 8.2 also illustrates that some nano-TiO_2 particles in the Intermixed-Type 1 samples were completely engulfed by the surrounding cement hydrated products, which more than likely impaired the NO_x removal capacity. Whereas, most of the spray-coated TiO_2 particles were free from the accumulation of the hydration products and could be fully exposed to UV light. Therefore, the SEM-EDX results are well corroborated by the aforementioned explanations with respect to the observed differences in the photocatalytic NO_x removal.

8.3 Influence of Dust Accumulation and Recovery Cleansing Processes

8.3.1 Influence of Dust Accumulation

Figure 8.3 shows the NO_x removal profiles of the Intermixed-Type 1 (Fig. 8.3a) and SP-Type 2 samples (Fig. 8.3b) after being subjected to different amounts of dust accumulation on the surface. In general, the samples with a higher volume of accumulated dusts displayed a lower ability to remove NO_x, regardless of the sample types. For example, the 37 $g \cdot m^{-2}$ of dust accumulation significantly reduced the NO_x removal ability of both types of samples (from 136.5 to 39.5 $\mu mol \cdot h^{-1} \cdot m^{-2}$ for intermixed-Type 1 and from 254.9 to 148.7 $\mu mol \cdot h^{-1} \cdot m^{-2}$ for SP-Type 2 samples, respectively). However, it must be pointed out that even after 37 $g \cdot m^{-2}$ of dust accumulation, the SP-Type 2 samples were still able to deliver a high photocatalytic NO_x removal ability. This can be explained by the fact that the dusts accumulated on the surface were not densely compacted (no external force was applied to the dust covered surface), thus the light blocking effect was not too significant. Also, considering that the size of nano-TiO_2 particles used in this study was far smaller than that of the dust particles (see Fig.3.12), the UV light was still able to penetrate through the dust particles to reach the TiO_2 particles

underneath, and some of which were still available to produce the photocatalytic activity.
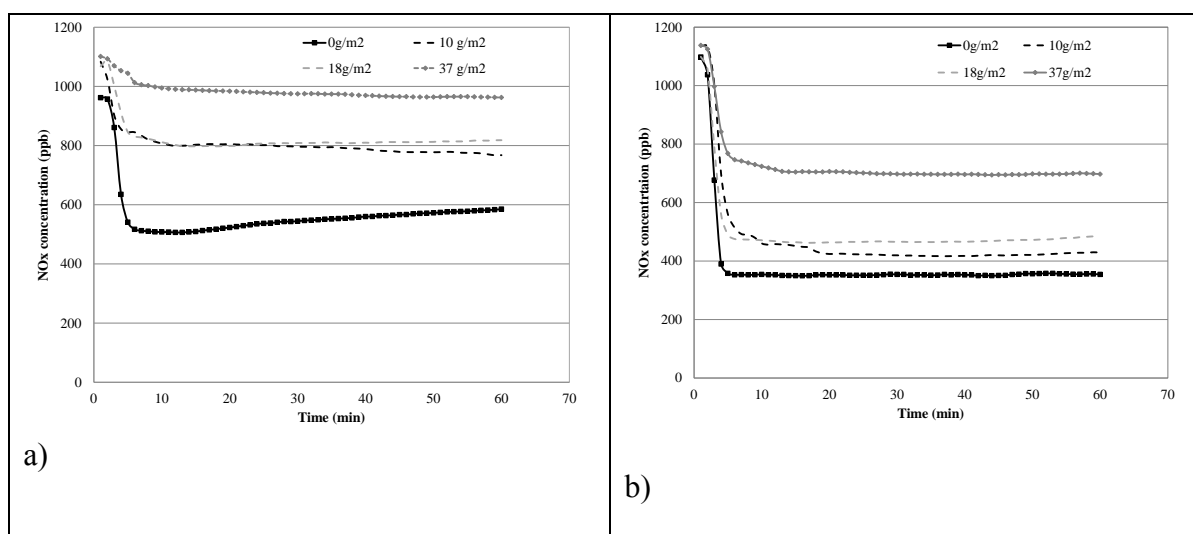
Figure 8.3 Photocatalytic NO_x removal profiles of a) Intermixed-Type 1 and b) SP-Type 2

samples after subjected to dust accumulation
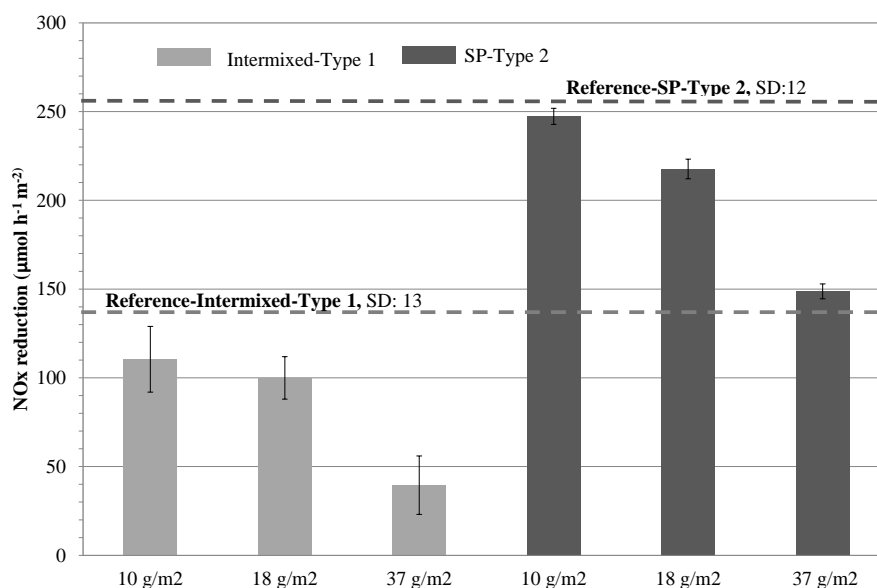
Figure 8.4 The photocatalytic NO_x removal of samples with dust accumulation on its surface

More interestingly, it was clearly observed that the dust accumulation exerted a lesser influence on the SP-Type 2 samples than on the Intermixed-Type 1 samples. This fact was consistent with the previous NO_x removal results of reference samples (section 8.2). For example, the SP-Type 2 samples still retained a relatively higher capacity of NO_x removal after exposure to 37 $g \cdot m^{-2}$ of dust accumulation (above 145 $\mu mol \cdot h^{-1} \cdot m^{-2}$), which was even higher than that of the Intermixed-Type 1 samples (136.5 $\mu mol \cdot h^{-1} \cdot m^{-2}$) without any dust

accumulation (Fig. 8.4).

8.3.2 Rejuvenation of NO_x Removal by Cleansing Processes

Figure 8.5 shows the surface appearance of the samples after they were subjected to different cleansing processes. The surfaces of all the Intermixed-Type 1 samples were similar in appearance to those of the reference sample after the application of two different cleansing processes. However, for the SP-Type 2 samples, the intensity of the white colour (an indication of the TiO_2 amount) was slightly decreased after the cleansing process due to the washing away of some nano-TiO_2 particles from the surface.

Intermixed-Type 1			SP-Type 2		
Reference	Cleaned with water after 37 $g \cdot m^{-2}$ of dust	Cleaned with water plus brush after 37 $g \cdot m^{-2}$ of dust	Reference	Cleaned with water after 37 $g \cdot m^{-2}$ of dust	Cleaned with water plus brush after 37 $g \cdot m^{-2}$ of dust

Figure 8.5 Intermixed-Type 1 and SP-Type 2 samples cleaned by different processes

Figure 8.6 demonstrates the NO_x removal of the two types of samples after they were subjected to the two cleansing processes. It was observed that both the Intermixed-Type 1 and SP-Type 2 samples recovered their initial NO_x removal capacity. According to the test results of the Intermixed-Type 1 samples, the additional use of brush (Fig. 8.6b) did not further improve the capacity of NO_x removal in comparison with the samples that were only cleaned

with water (Fig. 8.6a). This indicates that washing is sufficient to rejuvenate their initial photocatalytic NO_x removal ability. Unexpectedly, the process of cleansing slightly improved the NO_x removal capacity of the Intermixed-Type 1 reference sample. The samples subjected to a higher dust accumulation achieved a higher NO_x removal capacity. The reason behind this observation may be due to the abrasion action of the cleansing process, leading to more nano-TiO_2 particles (previously embedded) being exposed to air and thus increasing the available active TiO_2 sites on the surface (Jimenez-Relinque et al., 2015). The cleansing process also increased the roughness of the surface and the available active surface, resulting in a slight increase in the NO_x removal capacity (De Melo et al., 2012; Sugrañez et al., 2013; Jimenez-Relinque et al., 2015).

a)   b)
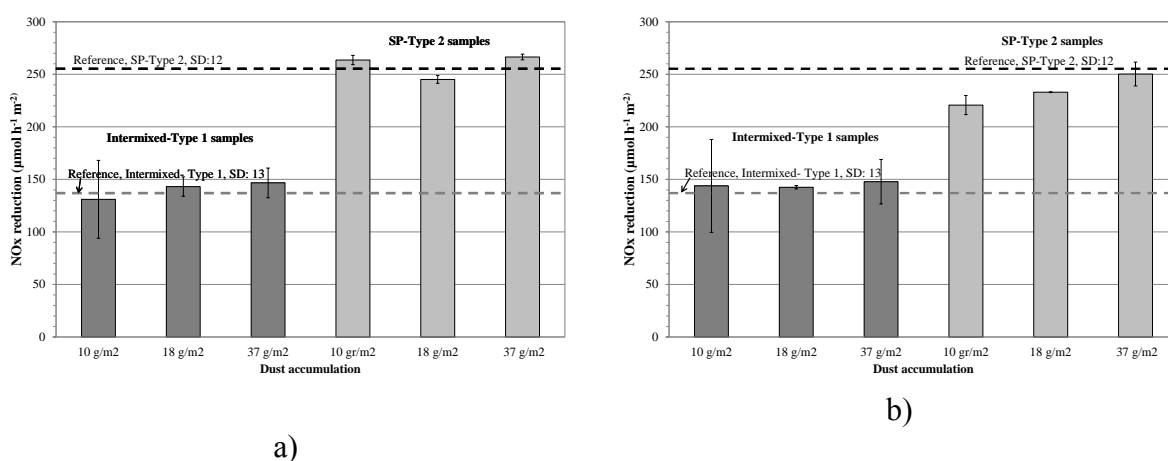
Figure 8.6 Photocatalytic NO_x removal of samples after subjected to cleansing with a) water and b) water and brush process

For the SP-Type 2 samples, the brush cleansing (Fig. 8.6b) slightly reduced the NO_x removal capacity when compared to the reference samples. The use of brush cleansing caused the removal of a certain amount of nano-TiO_2 particles from the surface of the samples, thus contributing to a decrease in their NO_x removal capacity.

8.4 Influence of Oil Accumulation and Recovery Cleansing Processes

8.4.1 Influence of Oil Accumulation

Figure 8.7a illustrates the NO_x removal activity of Intermixed-Type 1 samples and their corresponding reference samples after being impregnated with different concentrations of oil. Motor oil concentrations of 200 $g \cdot m^{-2}$ and 400 $g \cdot m^{-2}$ on the sample surfaces resulted in a complete loss of the NO_x removal capacity of the Intermixed-Type 1 sample. Similarly, the SP-Type 2 samples suffered a loss of 80-90% in their NO_x removal capacity (Fig. 8.7b).

a)

b)
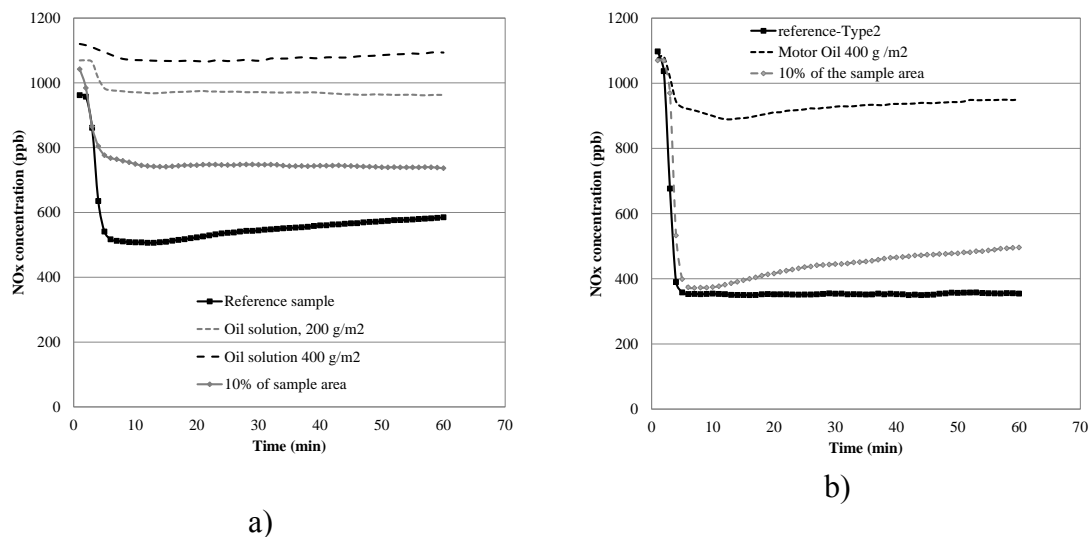
Figure 8.7 Influence of oil accumulation on photocatalytic NO_x removal a) Intermixed-Type 1 and b) SP-Type 2 samples

It was also observed that when 10% of the surface of both the Intermixed-Type1 and SP-Type 2 specimens was impregnated with oil, there occurred a reduction of approximate 25% and 10% respectively in the original NO_x removal efficiency. Apparently, the presence of oil on the surface of the nano-TiO_2 particles completely isolated them from contacting with air and light, but the effect of the localized contamination did not spread out to other parts of the concrete surface.

8.4.2 Rejuvenation of NO$_x$ Removal by Cleansing Processes

Figure 8.8 illustrates the NO$_x$ removal capacity when the samples were impregnated with the motor oil and after undergoing different cleansing processes. Both cleansing methods were found to be inefficient in removing the motor oil. For example, the SP-Type 2 sample did not fully recover its NO$_x$ removal capacity after being cleaned or treated with the n-hexane solution.
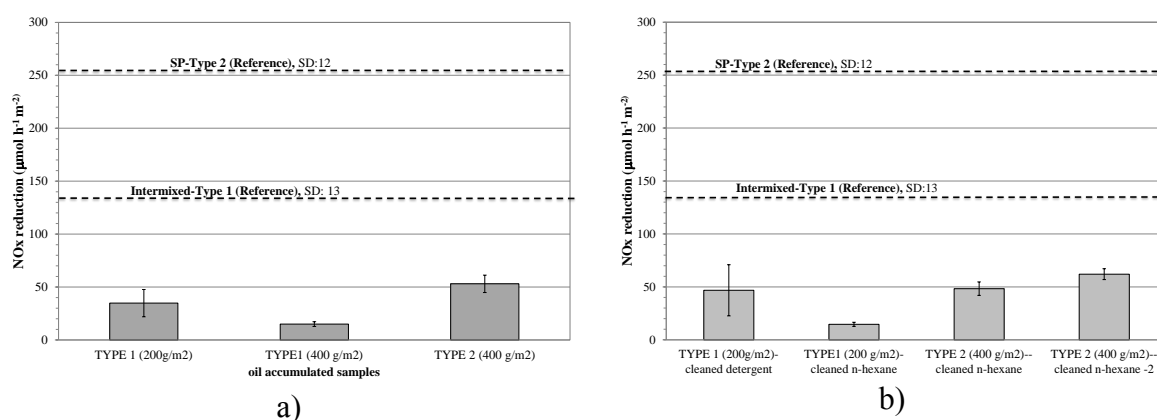
Figure 8.8 a) Photocatalytic NO$_x$ removal of the samples impregnated with motor oil; b) the Intermixed-Type 1 and SP-Type 2 samples cleaned by different cleansing methods

As mentioned in section 8.4.1, the samples which had 10% of their surface impregnated with motor oil lost approximately 10% of their NO$_x$ removal capacity. However, applying the cleansing agents extended the spread of the oil to cover the entire sample surface. Consequently, the samples having 10% of their area impregnated with motor oil experienced a decrease of NO$_x$ removal capacity from 219.8 to 188.9 $\mu mol \cdot h^{-1} \cdot m^{-2}$ when the samples were cleaned by the n-hexane solution. This demonstrates a very serious detrimental effect of oil contamination on the photocatalytic activities of the concerned samples.

SEM-EDX analysis was undertaken to examine the surface morphology of the samples in order to identify changes of the nano-TiO$_2$ particles before and after applying the oil contamination (Fig. 8.9 and 8.10). The morphology of the nano-TiO$_2$ particles presented on

136

the surface of the contaminated samples was quite similar to those of the reference sample. However, its detected titanium content through the EDX analysis was much lower. This was probably due to the presence of the oil envelope surrounding the surface of TiO_2 particles. Being oleophobic, TiO_2 nanoparticles might have tried to stay apart from the oil and hence be pushed toward the bottom (i.e. toward the sliding surface), ultimately depositing themselves on the bottom surface due to gravity (Ingole et al., 2013).
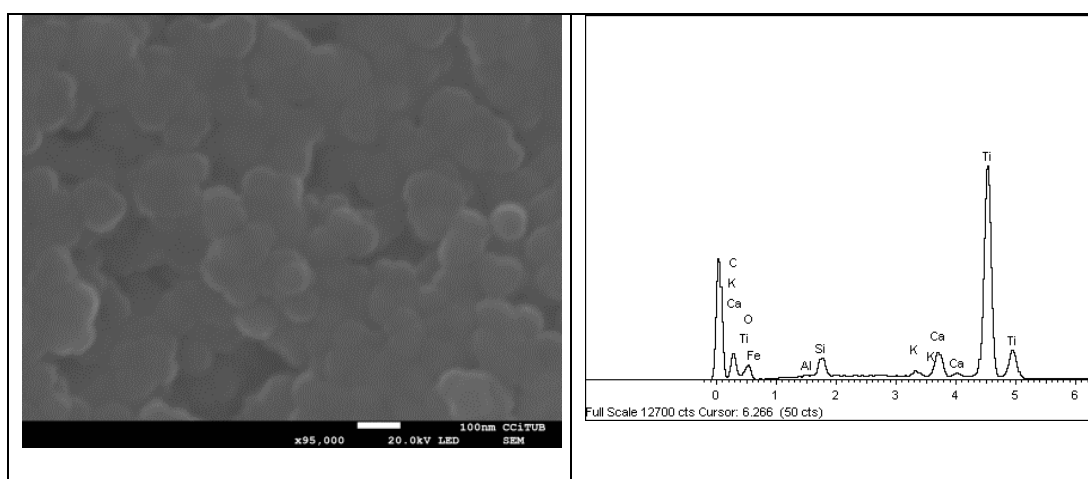
Figure 8.9 SEM-EDX analysis of SP-Type 2 reference sample before mobile oil contamination
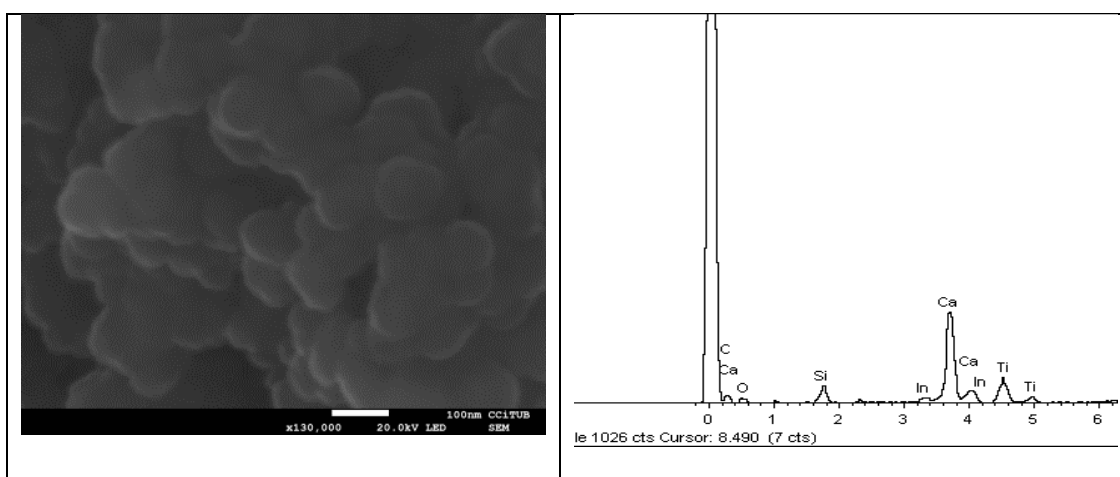
Figure 8.10 SEM-EDX analysis of the SP-Type 2 reference sample after exposure to mobile oil contamination

Probably, the most effective method for cleaning the oil contaminated samples would be to leave them for a sustained period of time under UV light, as the photocatalysis of the nano-

TiO$_2$ particles can decompose the adsorbed organic molecules due to a light-induced self-cleaning and antifouling function (Li et al., 2015). Longer term studies are required to ascertain such effects.

8.5 Summary

This chapter provides further evidence that the concrete surface layers spray-coated with nano-TiO$_2$ particle solution (SP-Type 2) were more effective in NO$_x$ removal than those produced using 5% nano-TiO$_2$ as intermixed additives (Intermixed-Type 1). A relatively higher accessibility of the bulk of the spray-coated TiO$_2$ particles to UV light irradiation was mainly responsible. When accumulated with a high amount of dusts, the SP-Type 2 samples were still able to partially maintain their initial NO$_x$ removal capacity, while the Intermixed-Type 1 samples suffered a severely impaired NO$_x$ removal capacity. However, the water cleansing process was sufficient to recover the initial NO$_x$ removal capacity of both types of samples. As for the effect of oil contamination, it is a totally different story. When motor oil was applied on the sample surface, oleophobic and high specific surface nano-TiO$_2$ particles were confined to the bottom of the oil, thus losing their photocatalytic capacity. As a result, the SP-Type 2 samples experienced a loss of 80-90% reduction in their initial NO$_x$ removal capacity, whereas, the Intermixed-Type 1 samples registered a complete loss. Moreover, cleansing processes either with an alkaline detergent or with an n-hexane solvent failed to recover their respective NO$_x$ removal capacity.

Overall, the spray coated samples (SP-Type 2) were much more effective in NO$_x$ removal than the intermixed samples in any mode of the sample tested (reference, contaminated or cleansed samples). This further demonstrates that the SP-Type 2 product holds great promise for practical applications.

CHAPTER 9

Conclusions

9.1 Introduction

The objective of this study is to develop photocatalytic cementitious materials with both a high efficiency and a low cost in order to lay a solid foundation for future real-life applications. Two types of products, namely self-compacting architectural mortar and concrete surface layers, have been produced and investigated in terms of various photocatalytic activities. For the production of architectural mortar, the traditional intermixing method was first used to combine TiO_2 with cementitious materials, as well as adopting recycled glass as aggregates (Chapter 4). Then, a clear paint containing TiO_2 was applied on the surface of architectural mortar as an alternative strategy to boost the photocatalytic efficiency. A wide range of photocatalytic activities were subsequently studied and compared (Chapter 5). Moreover, the effect of cement types on the photocatalytic NO_x removal and the underlying mechanisms were examined and dissected in detail (Chapter 6). For the fabrication of concrete surface layers, a simple but effective way to incorporate TiO_2 into the products has been developed and proved superior to the conventional intermixing method either under a myriad of experimental conditions (Chapter 7) or subject to different environmental circumstances (Chapter 8). In this chapter, the conclusions of all the above mentioned research aspects were summarized, and recommendations for the future work were also provided.

9.2 Conclusions

9.2.1 Combined Use of Recycled Glass and TiO$_2$ in Architectural Mortars

The combined use of recycled glass as aggregate and TiO$_2$ as photocatalyst in the production of architectural mortars has been realized. It has been found that samples prepared with 100% recycled glass and a dosage of 5% TiO$_2$ (by weight of binder) achieved the highest NO$_x$ removal rate. The improved photocatalytic efficiency can be attributed to the light transmittance property of recycled glass. Interestingly, the mixing rate was found to play an import role in dispersing the nano-TiO$_2$ particles. Agglomerates formed at a slower mixing rate (16 rpm) and a higher dosage of TiO$_2$ (5%), resulting in a reduction in the compressive and flexural strength. However, this problem can be circumvented when a higher rate (190 rpm) was used, reflected by an enhancement in the compressive strength. Moreover, adding more glass contents, coupled with increasing TiO$_2$ dosages, led to an increase in both the ASR expansions and carbonation depths. But the ASR expansions were all below the permissible limit (0.1) due to the use of metakaolin as a pozzolana.

9.2.2 Versatile Photocatalytic Functions of Architectural Mortars and Their Inter-Relationship

Attempts were made to enhance the photocatalytic efficiency of architectural mortars by means of applying a TiO$_2$ containing paint (PC-S7) on their surfaces. In comparison with the 5% TiO$_2$ incorporated samples prepared by the conventional intermixing method, the PC-S7-coated samples displayed a much higher efficiency in a wide range of photocatalytic activities. For example, the PC-S7-coated architectural mortars delivered both a significantly high NO$_x$ and xylene degradation performance. In stark contrast, the 5% TiO$_2$-intermixed counterparts only showed a much lower NO$_x$ removal rate and failed to degrade xylene. Also, the PC-S7-coated architectural mortars achieved a total inactivation of *E. coli* after 120 min of UVA irradiation, while the 5% TiO$_2$-intermixed samples had a negligible *E. coli* killing

activity. Moreover, both photocatalytic active architectural mortars showed a satisfactory algae killing ability compared with the reference samples. The ultra-fine particle size (specific surface area=300 $m^2 \cdot g^{-1}$), as well as a relatively higher content (10% by weight of paint) of anatase TiO_2 particles in the paint, contributed to the superior photocatalytic activities of the PC-S7-coated samples. More importantly, the PC-S7-coated samples also garnered a robust weathering-resistant ability, reflected by an almost unchanged ability to photocatalytic degrade RhB after exposure to a facade weathering process (representing a usage period of about 20 years under Hong Kong weather conditions), as well as an accelerated carbonation process, dispelling the concerns on their long-term durability.

Overall, it seems that the photocatalytic bactericidal activity was more closely related with the photocatalytic degradation ability of the organic matter (xylene and RhB). Therefore, caution should be taken when extrapolating the results of the photocatalytic NO_x removal activity to that of either the photocatalytic organic matter degradation or bactericidal activities. It is noteworthy that the porosity and roughness of the sample surface played a more prominent role than the photocatalytic activity in the process of anti-algae fouling.

9.2.3 Influence of Cement Types on NO_x Removal and the Underlying Mechanisms

An interesting finding from our previous studies showed that white cement (WC) was superior to ordinary Portland cement (OPC) in boosting the photocatalytic NO_x removal of cementitious materials. But the underlying mechanisms still remain elusive. The search for the reason focused on the potential difference in the light absorption process and electron-hole separation activity between WC and OPC, especially the role iron oxide (Fe_2O_3) played in OPC.

The results clearly demonstrated that in comparison with WC, OPC displayed a much higher light absorption ability, suggesting that less light would be reflected to the surrounding TiO_2 surface. As a result, fewer electron-hole pairs will be generated, leading to a corresponding

diminished photocatalytic redox activity. On the other hand, even if the same amount of light does strike on the surface of TiO_2, a stronger charge transfer resistance of OPC made the electron-hole pairs difficult to separate and migrate to the TiO_2 surface. Instead, the generated electron-hole pairs were prone to recombination, emitting the energy as heat. These two adverse effects worked together to give the OPC/TiO_2 mixtures a poorer photocatalytic performance. This inferior photocatalytic behaviour is mainly ascribed to a relative abundance of Fe_2O_3 in OPC as opposed to WC, which was supported by the observations that all the differences between OPC and WC were mirrored by the corresponding changes incurred by the addition of Fe_2O_3 in WC.

9.2.4 Development of Novel TiO_2 Incorporation Method and Influence of Experimental Factors on NO_x Removal

A novel method to produce photocatalytic concrete surface layers with a high efficiency and a low cost was developed. Products prepared by such a new method held various advantages over those prepared by the intermixing and dip-coating methods. The effects of variable experimental factors on the photocatalytic NO_x removal performance of the Intermixed-Type 1 and SP-Type 2 concrete surface layers were studied by employing two assessment indicators (NO_x removal rate and NO_x removal ratio) to give a more comprehensive picture. The results showed that the SP-Type 2 samples dwarfed the Intermixed-Type 1 samples regardless of the imposed experimental factors. It was found that both the NO flow rate and initial NO concentration exerted a positive impact on the NO_x removal rate but a negative influence on the NO_x removal ratio. In contrast, the UV light intensity had a positive relationship with both the NO_x removal rate and the NO_x removal ratio. However, the influence of humidity was more complex. The NO_x removal efficiency (both NO_x removal rate and NO_x removal ratio) first increased, reached a peak and then decreased with continuously increasing relative humidity. It should be pointed out that the NO_x removal rate

and NO_x removal ratio are not always positively related to each other, especially when the retention time of the gaseous pollutants in the photocatalytic reactor acts as a defining factor. The photocatalytic activity of the TiO_2 containing concrete surface layers was most effective under UV irradiation, but a comparable NO_x removal rate was also observed under Solar Light irradiation. Moreover, the products prepared by the newly developed spray-coating method also possessed a robust weathering resistant ability, holding great potential for practical applications.

9.2.5 Influence of Environmental Factors on NO_x Removal of Surface Layers Intermixed and Spray-Coated with TiO_2

To investigate the negative effect of contaminating substances on the NO_x removal efficiency of photocatalytic eco-blocks in real-life service, as well as the recovery strategies, the Intermixed-Type 1 and SP-Type 2 concrete surface layers were subject to lab-simulated dust accumulation and oil contamination. The changes in their photocatalytic NO_x removal performance were then monitored before and after applying different cleansing processes. After a high amount of dust accumulations, the SP-Type 2 samples were still able to partially retain their initial NO_x removal capacity, while the Intermixed-Type 1 samples exhibited a severely impaired NO_x removal capacity. However, the initial NO_x removal capacity of both types of samples can be almost fully recovered by the water cleansing process. On the other hand, oil contamination was proved to be a rather recalcitrant nuisance. When motor oil was imposed on the surface of the two types of concrete surface layers, the SP-Type 2 samples experienced a loss of 80-90% in their initial NO_x removal capacity, while the Intermixed-Type 1 samples suffered a complete loss. It is likely that the oleophobic and high specific surface nano-TiO_2 particles were confined to the bottom of the oil in the presence of oil contaminants, thus losing access to the light irradiation. Cleansing processes either with an alkaline detergent or with an n-hexane solvent were unable to rejuvenate their respective NO_x

removal capacity. Overall, the advantages of the spray-coated samples (SP-Type 2) over the intermixed samples were once again substantiated. This lends further support to the conclusion that the SP-Type 2 product holds great promise for practical applications.

9.3 Recommendation for Future Work

Findings from the current thesis paved the way for real-life applications of the developed photocatalytic cementitious materials. However, several suggestions are recommended for further studies in the future.

In this research, it was found that the mixing rate played a vital role in distributing nano-TiO_2 particles in the cement-based matrix. A more systematic investigation concerning varying mixing rates and duration is required to identify the optimal sample preparation parameters for enhancing both the mechanical and photocatalytic properties of the mortars.

Although various lab-simulated weathering conditions have been applied to the two categories of photocatalytic cementitious materials, field trials need to be carried out to test the long-term durability of these products in order to give justification and incentives to scale up their industrial production.

It has been found that determining the photocatalytic efficiency of eco-blocks in real-life service is rather tricky due to the constantly fluctuation of environmental factors. Thus, new methods, such as measurement of nitrite/nitrate accumulation on the surface of samples, should be developed to give a more reliable and accurate indication of the real-time photocatalytic efficiency. More importantly, a direct relationship between nitrite/nitrate accumulation and NO_x removal needs to be established in the laboratory.

The photocatalytic degradation pathways of organic matters, such as xylene, merit particular attention in the future studies to give a more comprehensive picture of the photocatalytic degradation mechanisms. Also, it is necessary and helpful to dispel concerns about the

possible generation of toxic intermediates in the process of redox reactions.

Since TiO_2 is only effective under UV light irradiation, which only accounts for about 5% of the whole solar light, it is desirable to pursue new photocatalysts, which can absorb visible light. And a better understanding of their interplay with cementitious materials will facilitate their applications in the construction industry. More intriguingly, the applications of photocatalytic functional cementitious materials can be extended from the outdoor environments to the indoor environments.

REFERENCES

Aïssa, A.H., Puzenat, E., Plassais, A., Herrmann, J.M., Haehnel, C. and Guillard, C. Characterization and photocatalytic performance in air of cementitious materials containing TiO$_2$: Case study of formaldehyde removal. *Applied Catalysis B: Environmental* **2011**, 107, 1-8.

Alberici, R.M. and Jardim, W.F. Photocatalytic destruction of VOCs in the gas-phase using titanium dioxide. *Applied Catalysis B: Environmental* **1997**, 14, 55-68.

Allen, N.S., Edge, M., Verran, J., Stratton, J., Maltby, J. and Bygott, C. Photocatalytic titania based surfaces: Environmental benefits. *Polymer Degradation and Stability* **2008**, 93, 1632-1646.

Almquist, C.B. and Biswas, P. Role of synthesis method and particle size of nanostructured TiO$_2$ on its photoactivity. *Journal of Catalysis* **2002**, 212, 145-156.

Anpo, M., Shima, T., Kodama, S. and Kubokawa, Y. Photocatalytic hydrogenation of CH$_3$CCH with H$_2$O on small-particle TiO$_2$: Size quantization effects and reaction intermediates. *The Journal of Physical Chemistry* **1987**, 91, 4035.

Ballari, M.M., Yu, Q.L. and Brouwers, H.J.H. Experimental study of the NO and NO$_2$ degradation by photocatalytically active concrete. *Catalysis Today* **2011**, 161, 175-180.

Beeldens, A. Air purification by road materials: Results of the test project in Antwerpen. In Baglioni, P. and Cassar, L. Proceedings of the International RILEM Symposium on Photocatalysis to Construction materials. Florence, Italy, 8-9 October, **2007**.

Beeldens, A. Air purification by pavement blocks: Final results of the research at the BRRC. Proceedings of Transport Research Arena-TRA 2008, Ljubljana, Slovenia, 21-24 April, **2008**.

Beeldens, A. and Boonen, E. Photocatalytic applications in Belgium, purifying the air through the pavement. Proceedings of the XXIVth World Road Conference, Mexico City,

Mexico, 26-30 September, **2011**.

Benabbou, A.K., Derriche, Z., Felix, C., Lejeune, P. and Guillard, C. Photocatalytic inactivation of *Escherischia coli*: Effect of concentration of TiO_2 and microorganism, nature, and intensity of UV irradiation. *Applied Catalysis B: Environmental* **2007**, 76, 257-263.

Benoit-Marquie, F., Wilkenhoner, U., Simon, V., Braun, A., Oliveros, E. and Maurette, M.T. VOC photodegradation at the gas-solid interface of a TiO_2 photocatalyst Part I: 1-butanol and 1-butylamine. *Journal of Photochemistry and Photobiology A: Chemistry* **2000**, 132, 225-232.

Bhatkhande, D.S., Pangarkar, V.G., and Beenackers, A.A.C.M. Photocatalytic degradation for environmental applications-A review. *Journal of Chemical Technology and Biotechnology* **2001**, 77, 102-116.

Biard, P.F., Bouzaza, A. and Wolbert, D. Photocatalytic degradation of two volatile fatty acids in annular plug-flow reactor; Kinetic modelling and contribution of mass transfer rate. *Environmental Science & Technology* **2007**, 41 (8), 2908-2914.

Boonen, E. and Beeldens, A. Recent photocatalytic applications for air purification in Belgium. *Coatings* **2014**, 4, 553-573.

Boonstra, A.H. and Mutsares, C.A.H.A. Relation between the photoadsorption of oxygen and the number of hydroxyl groups on a titanium dioxide surface. *The Journal of Physical Chemistry* **1975**, 79, 1694-1698.

Bozinovski, E., Taubert, M., Kleinsteuber, S., Richnow, H.H., Von Bergen, M., Vogt, C. and Seifert, J. Metaproteogenomic analysis of a sulfate-reducing enrichment culture reveals genomic organization of key enzymes in the m-xylene degradation pathway and metabolic activity of proteobacteria. *Systematic and Applied Microbiology* **2014**, 37, 488-501.

Brandt, A.M. Cement-based composites: Materials, mechanical properties and performance, 2nd ed.; Taylor&Francis: Oxon, 2009; p 145.

Cassar, L., Pepe, C., Tognon, G., Guerrini, G.L. and Amadelli, R. White cement for architectural concrete, possessing photocatalytic properties. Proceedings of the 11th International Congress on the Chemistry of Cement, Durban, South Africa, May, 1-11, 2003.

Cassar, L. Photocatalysis of cementitious materials: Clean buildings and clean air. *Materials Research Society Bulletin* **2004**, May, 328-331.

Cassar, L., Beeldens, A., Pimpinelli, N. and Guerrini, G. Photocatalysis of cementitious materials. Proceedings International RILEM Symposium on Photocatalysis, Environment and Construction Materials-TDP 2007. RILEM Publications SARL. Florence, Italy, 8-9 October, **2007**.

Chen, J. and Poon, C.S. Photocatalytic construction and building materials: From fundamentals to applications. *Building and Environment* **2009a**, 44, 1899-1906.

Chen, J. and Poon, C.S. Photocatalytic activity of titanium dioxide modified concrete materials – Influence of utilizing recycled glass cullets as aggregates. *Journal of Environmental Management* **2009b**, 90, 3436-3442.

Chen, J. and Poon, C.S. Photocatalytic cementitious materials: Influence of the microstructure of cement paste on photocatalytic pollution degradation. *Environmental Science & Technology* **2009c**, 43, 8948-8952.

Chen, J. Environmentally friendly concrete paving blocks for photodegradation of air pollutions. PhD thesis **2010**, The Hong Kong Polytechnic University, Hong Kong, China.

Chen, J., Kou, S.C. and Poon, C.S. Photocatalytic cement-based materials: Comparison of nitrogen oxides and toluene removal potentials and evaluation of self-cleaning performance. *Building and Environment* **2011**, 46, 1827-1833.

Chen, J., Kou, S.C. and Poon, C.S. Hydration and properties of nano-TiO$_2$ blended cement composites. *Cement and Concrete Composites* **2012**, 34, 642-649.

Chen, F.N., Yang, X.D., Xu, F.F., Wu, Q. and Zhang, Y.P. Correlation of photocatalytic bactericidal effect and organic matter degradation of TiO$_2$ Part I: Observation of phenomena. *Environmental Science & Technology* **2009**, 43, 1180-1184.

Chen, S.H., Chang, C.S., Wang, H.Y. and Huang, W.L. Mixture design of high performance recycled liquid crystal glasses concrete (HPGC). *Construction and Building Materials* **2011**, 25, 3886-3892.

Choi, W., Kim, S., Cho, S., Yoo, H.I. and Kim, M.H. Photocatalytic reactivity and diffusing OH radicals in the reaction medium containing TiO$_2$ particles. *Korean Journal of Chemical Engineering* **2001**, 18 (6), 898-902.

Colbeau-Justin, C., Kunst, M. and Huguenin, D. Structural influence on charge-carrier lifetimes in TiO$_2$ powders studies by microwave absorption. *Journal of Materials Science* **2003**, 38 (11), 2429-2437.

Dalton, J.S., Janes, P.A., Jones, N.G., Nicholson, J.A., Hallam, K.R. and Allen, G.C. Photocatalytic oxidation of NO$_x$ gases using TiO$_2$: A surface spectroscopic approach. *Environmental Pollution* **2002**, 120 (2), 415-422.

Dambournet, D., Belharouak, I. and Amine, K. Tailored preparation methods of TiO$_2$ anatase, rutile, brookite: Mechanism of formation and electrochemical properties. *Chemistry of Materials* **2010**, 1173-1179.

De Belie, N. Microorganisms versus stony materials: A love-hate relationship. *Materials and Structures* **2010**, 43, 1191-1202.

De Larrard, F. Concrete mixture proportioning: A scientific approach. Taylor & Francis: New York, **1999**.

De Melo, J.V.S., Trichês, G., Gleize, P.J.P. and Villena, J. Development and evaluation of the

efficiency of photocatalytic pavement blocks in the laboratory and after one year in the field. *Construction and Building Materials* **2012**, 37, 310-319.

De Muynck, W., Maury-Ramirez, A., De Belie, N. and Verstraete, W. Evaluation of strategies to prevent algal fouling on white architectural and cellular concrete. *International Biodeterioration & Biodegradation* **2009**, 63, 679-689.

Demeestere, K., Dewluf, J., De Witte, B. and Van Langenhove, H. Titanium dioxide mediated heterogeneous photocatalytic degradation of gaseous dimethyl sufide: Parameter study and reaction pathways. *Applied Catalysis B: Environmental* **2005**, 60 (1-2), 93-106.

Demeestere, K., Dewulf, J. and Van Langenhove, H. Heterogeneous Photocatalysis as an advanced oxidation process for the abatement of chlorinated, monocyclic aromatic and sulphurous volatile organic compounds in air: State of the art. *Critical Reviews in Environmental Science & Technology* **2007**, 37 (6), 489-538.

Demeestere, K., Dewulf, J., De Witte, B., Beeldens, A. and Van Langenhove, H. Heterogeneous photocatalytic removal of toluene from air on building materials enriched with TiO_2. *Building and Environment* **2008**, 43 (4), 406-414.

De Schutter, G., Bartos, P.J.M., Domone, P. and Gibbs, J. Self-compacting Concrete. CRC Press Inc, **2008**.

Dhar, S., Roy Barman, A., Rusydi, A., Gopinadhan, K., Feng, Y., Breese, M., Hilgenkamp, H. and Venkatesan, T. Effect of Ta alloying on the optical, electronic, and magnetic properties of TiO_2 thin films. *Functional Metal Oxides: New Science and Novel Applications* **2013**, 133-162.

Diamanti, M.V., Lollini, F., Pedeferri, M.P. and Bertolini, L. Mutual interactions between carbonation and titanium dioxide photoactivity in concrete. *Building and Environment* **2013**, 62, 174-181.

Dias, W.P.S. Reduction of concrete sorptivity with age through carbonation. *Cement and*

Concrete Research **2000**, 30, 1255-1261.

Dienemann, W. Selbstreiningende Fassadenplatten aus Beton: Self-cleaning concrete cladding panels. BFT Betonwerk + Fertigteil-Technik. *Concrete Plant + Precast Technology* **2006**, 2, 14-16.

Duan, X., Su, D., Zhu, Z., Chen, X. and Shi, P. Photocatalytic decomposition of toluene by TiO_2 film as photocatalyst. *Journal of Environmental Science & Health Part A-Toxic/Hazardous Substances & Environmental Engineering* **2002**, 37, 679-692.

Dufour, F., Pigeot-Remy, S., Durupthy, O., Cassaignon, S., Ruaux, V., Torelli, S., Mariey, L., Maugé, F. and Chanéac, C. Morphological control of TiO_2 anatase nanoparticles: What is the good surface property to obtain efficient photocatalysts? *Applied Catalysis B: Environmental* **2015**, 174-175, 350-360.

Egerton, T. and King, C. The influence of light intensity on photoactivity in TiO_2 pigmented systems. *Journal of the Oil and Colour Chemists Association* **1979**, 62 (10), 386-391.

Espinosa, R.M. and Franke, L. Influence of the age and drying process on pore structure and sorption isotherms of hardened cement pastes. *Cement and Concrete Research* **2006**, 36 (10), 1969-1984.

Folli, A., Pade, C., Hansen, T.B., De Marco, T. and Macphee, D.E. TiO_2 photocatalysis in cementitious systems: Insights into self-cleaning and depollution chemistry. *Cement and Concrete Research* **2012**, 42, 539-548.

Fonseca, A.J., Pina, F., Macedo, M.F., Leal, N., Romanowska-Deskins, A., Laiz, L., Gómez-Bolea, A. and Saiz-Jimenez, C. Anatase as an alternative application for preventing biodeterioration of mortars: Evaluation and comparison with other biocides. *International Biodeterioration & Biodegradation* **2010**, 64, 388-396.

Fox, M.A. and Dulay, M.T. Heterogeneous photocatalysis. *Chemical Reviews* **1993**, 93 (1), 341-357.

Fujishima, A. and Honda, K. Electrochemical photolysis of water at a semiconductor electrode. *Nature* **1972**, 238, 37-38.

Fujishima, A., Rao, T.N. and Tryk, D.A. Titanium dioxide photocatalysis. *Journal of Photochemistry and Photobiology C: Photochemistry Reviews* **2000**, 1 (1), 1-21.

Fujishima, A., Zhang, X.T. and Tryk, D.A. TiO$_2$ photocatalysis and related surface phenomena. *Surface Science Reports* **2008**, 63 (12), 515-582.

Gallus, M., Akylas, V., Barmpas, F., Beeldens, A., Boonen, E., Boréave, A., Cazaunau, M., Chen, H., Daële, V., Doussin, J.F., Dupart, Y., Gainoz, C., George, C., Grosselin, B., Herrmann, H., Ifang, S., Kurtenbach, R., Maille, M., Mellouki, A., Miet, K., Mothes, F., Moussionpoulos, N., Poulain, L., Rabe, R., Zapf, P. and Kleffmann, J. Photocatalytic de-pollution in the Leopold II tunnel in Brussels: NO$_x$ abatement results. *Building and Environment* **2015**, 84, 125-133.

Giannantonio, D.J., Kurth, J.C., Kurtis, K.E. and Sobecky, P.A. Effects of concrete properties and nutrients on fungal colonization and fouling. *International Biodeterioration & Biodegradation* **2009**, 63, 252-259.

Gladis, F. and Schumann, R. Influence of material properties and photocatalysis on phototrophic growth in multi-year roof weathering. *International Biodeterioration & Biodegradation* **2011**, 65, 36-44.

Goei, R. and Lim, T.T. Asymmetric TiO$_2$ hybrid photocatalytic ceramic membrane with porosity gradient: Effect of structure directing agent on the resulting membranes architecture and performances. *Ceramics International* **2014**, 40, 6747-6757.

Graniani, L., Quagliarini, E., Bondioli, F. and D'Orazio, M. Durability of self-cleaning TiO$_2$ coatings on fired clay brick facades: Effects of UV exposure and wet & dry cycles. *Building and Environment* **2014**, 71, 193-203.

Guerrini, G.L. and Peccati, E. Photocatalytic cementitious roads for depollution. In

photocatalysis, Environment and Construction Materials, Proceedings of the International RILEM Symposium, Italy, 2007; Baglioni, P. and Cassar, L., Eds.; RILEM: Bagneux, **2007**.

Guerrini, G.L. and Corazza, F. White cement and photocatalysis part 2: Applications. Proceedings of First Arab international Conference on The Uses of White Cement, Cairo, Egypt, April 28-30, **2008**.

Guo, M.Z., Ling, T.C. and Poon, C.S. TiO_2-based self-compacting glass mortar: Comparison of photocatalytic nitrogen oxide removal and bacteria inactivation. *Building and Environment* **2012**, 53, 1-6.

Guo, M.Z., Ling, T.C. and Poon, C.S. Nano-TiO_2-based architectural mortar for NO removal and bacteria inactivation: Influence of coating and weathering conditions. *Cement and Concrete Composites* **2013**, 36, 101-108.

Guo, M.Z. and Poon, C.S. Photocatalytic NO removal of concrete surface layers intermixed with TiO_2. *Building and Environment* **2013**, 70, 102-109.

Guo, T., Bai, Z.P., Wu, C. and Zhu, T. Influence of relative humidity on the photocatalytic oxidation (PCO) of toluene by TiO_2 loaded on activated carbon fibers: PCO rate and intermediates accumulation. *Applied Catalysis B: Environmental* **2008**, 79 (2), 171-178.

Gunschera, J., Andersen, J.R., Schulz, N. and Salthammer, T. Surface-catalyzed reactions on pollutant-removing building products for indoor use. *Chemosphere* **2009**, 75, 476-482.

Hager, S. and Bauer, R. Heterogeneous photocatalytic oxidation of organics for air purification by near UV irradiated titanium dioxide. *Chemosphere* **1999**, 38 (7), 1549-1559.

Han, X.G., Kuang, Q., Jin, M.S., Xie, Z.X. and Zheng, L.S. Synthesis of titania nanosheets with a high percentage of exposed {001} facets and related photocatalytic properties. *Journal of the American Chemical Society* **2009**, 131 (9), 3152-3153.

Hanaor, D. and Sorrell, C. Review of the anatase to rutile phase transformation. *Journal of Materials Science* **2011**, 46, 855-874.

Hashimoto, K., Irie, H. and Fujishima, A. TiO$_2$ photocatalysis: A historical overview and future prospects. *Japanese Journal of Applied Physics* **2005**, 44 (12), 8269-8285.

Herrmann, J.M., Péruchon, L., Puzenat, E. and Guillard, C. Photocatalysis: From fundamentals to self-cleaning glass application. The proceedings of international RILEM symposium on photocatalysis, environment and construction materials, **2007**.

Hoffmann, M.R., Martin, S.T., Choi, W.Y. and Bahnemann, D.W. Environmental applications of semiconductor photocatalysis. *Chemical Reviews* **1995**, 95, 69-96.

Hong, X.T., Luo, Z.P. and Batteas, J.D. Enhanced visible-light absorption and dopant distribution of iodine-TiO$_2$ nanoparticles synthesized by a new facile two-step hydrothermal method. *Journal of Solid State Chemistry* **2011**, 184, 2244-2249.

Huang, Z., Maness, P.C., Blake, D.M., Wolfrum, E.J., Smolinski, S.L. and Jacoby, W.A. Bactericidal mode of titanium dioxide photocatalysis. *Journal of Photochemistry and Photobiology A: Chemistry* **2000**, 130, 163-170.

Hubler, M.H., Thomas, J.J. and Jennings, H.M. Influence of nucleation seeding on the hydration kinetics and compressive strength of alkali activated slag paste. *Cement and Concrete Research* **2011**, 41 (8), 842-846.

Hung, C.H. and Mariñas, B.J. Role of water in the photocatalytic degradation of trichloroethylene vapour on TiO$_2$ films. *Environmental Science & Technology* **1997**, 31 (5), 1440-1445.

Hurum, D.C., Gray, K.A., Rajh, T. and Thurnauer, M.C. Recombination pathways in the Degussa P25 formulation of TiO$_2$: surface versus lattice mechanisms. *The Journal of Physical Chemistry B* **2005**, 109, 977-980.

Hüsken, G., Hunger, M. and Brouwers, H.J.H. Comparative study on cementitious products

containing titanium dioxide as photo-catalyst. In Photocatalysis, Environment and Construction Materials, Proceedings of the International RILEM Symposium, Italy, **2007**.

Hüsken, G., Hunger, M. and Brouwers, H.J.H. Experimental study of photocatalytic concrete products for air purification. *Building and Environment* **2009**, 44 (12), 2463-2474.

Ingole, S., Charanpahari, A., Kakade, A., Umare, S.S., Bhatt, D.V. and Menghani, J. Tribological behaviour of nano TiO_2 as an additive in base oil. *Wear* **2013**, 301, 776-785.

Jacobsen, A.E. Titanium dioxide pigments: Correlation between photochemical reactivity and chalking. *Industrial & Engineering Chemistry* **1949**, 41, 523-526.

Jalal, M., Fathi, M. and Farzad, M. Effects of fly ash and TiO_2 nanoparticles on rheological, mechanical, microstructural and thermal properties of high strength self compacting concrete. *Mechanics of Materials* **2013**, 61, 11-27.

Jeong, J., Sekiguchi, K., Lee, W. and Sakamoto, K. Photodegradation of gaseous volatile organic compounds (VOCs) using TiO_2 photoirradiated by an ozone-producing UV lamp: decomposition characteristics, identification of by-products and water-soluble organic intermediates. *Journal of Photochemistry and Photobiology A: Chemistry* **2005**, 169 (3), 279-287.

Jiang, J., Oberdörster, G., Elder, A., Gelein, R., Mercer, P. and Biswas, P. Does nanoparticles activity depend upon size and crystal phase? *Nanotoxicology* **2008**, 2 (1), 33-42.

Jimenez-Relinque, E., Rodriguez-Garcia, J.R., Castillo, A. and Castellote, M. Characteristics and efficiency of photocatalytic cementitious materials: Type of binder, roughness and microstructure. *Cement and Concrete Research* **2015**, 71, 124-131.

Johannesson, B. and Utgenannt, P. Microstructural changes caused by carbonation of cement mortar. *Cement and Concrete Research* **2001**, 31, 925-931.

Kim, S.B. and Hong, S.C. Kinetic study for photoctalytic degradation of volatile organic compounds in air using thin film TiO_2 photocatalyst. *Applied Catalysis B: Environmental*

2002, 35 (4), 305-315.

Krishnan, P., Zhang, M.H., Yu, L. and Feng H. Photocatalytic degradation of particulate pollutants and self-cleaning performance of TiO$_2$-containing silicate coating and mortar. *Construction and Building Materials* **2013a**, 44, 309-316.

Krishnan, P., Zhang, M.H., Cheng, Y.H., Riang, D.T. and Yu, L.E. Photocatalytic degradation of SO$_2$ using TiO$_2$-containing silicate as a building coating material. *Construction and Building Materials* **2013b**, 43, 197-202.

Kubacka, A., Ferrer, M., Cerrada, M.L., Serrano, C., Sánchez-Chaves, M., Fernández-García, M., De Andrés, A., Riobóo, R.J.J., Fernández-Martín, F. and Fernández-García, M. Boosting TiO$_2$-anatase antimicrobial activity: Polymer-oxide thin films. *Applied Catalysis B: Environmental* **2009**, 89, 441-447.

Lackhoff, M., Prieto, X., Nestle, N., Dehn, F. and Niessner, R. Photocatalytic activity of semiconductor-modified cement – Influence of semiconductor type and cement ageing. *Applied Catalysis B: Environmental* **2003**, 43, 205-216.

Lan, Y.Q., Hu, C., Hu, X.X. and Qu, J.H. Efficient destruction of pathogenic bacteria with AgBr/TiO$_2$ under visible light irradiation. *Applied Catalysis B: Environmental* **2007**, 73, 354-360.

Landmann, M., Rauls, E. and Schmidt, W.G. The electronic structure and optical response of rutile, anatase and brookite TiO$_2$. *Journal of Physics: Condensed Matter* **2012**, 24, 195503-19508.

Lee, B.Y., Thomas, J.J., Treager, M. and Kurtis, K.E. Influence of TiO$_2$ nanoparticles on early C$_3$S hydration. *ACI Special, Publication* **2009**, 267, 35-44.

Lee, K., Kim, M. and Kim, H.J. Catalytic nanoparticles being facet-controlled. *Journal of Materials Chemistry* **2010**, 20, 3791-3798.

Li, J.G. and Ishigaki, T. Brookite→rutile phase transformation of TiO$_2$ studied with

monodispersed particles. *Acta Materialia* **2004**, 52, 5143-5150.

Li, L., Liu, Z., Zhang, Q., Meng, C., Zhang, B.T. and Zha, J. Underwater superoleophobic porous membrane based on hierarchical TiO2 nanotubes: Multifunctional integration of oil-water separation, flow-through photocatalysis and self-cleaning. *Journal of Materials Chemistry A* **2015**, 3, 1279-1286.

Ling, T.C. and Poon, C.S. Properties of architectural mortar prepared with recycled glass with different particle size. *Material & Design* **2011**, 32, 2675-2684.

Ling, T.C., Poon, C.S. and Kou, S.C. Feasibility of using recycled glass in architectural cement mortars. *Cement and Concrete Composites* **2011**, 33, 848-854.

Linkous, C.A., Carter, G.J., Locuson, D.B., Ouellete, A.J., Slattery, D.K. and Smitha, L.A. Photocatalytic inhibition of algae growth using TiO_2, WO_3, and cocatalyst modifications. *Environmental Science & Technology* **2000**, 34, 4754-4758.

Liu, S.W., Yu, J.G. and Jaroniec, M. Anatase TiO_2 with dominant high-energy {001} facets: Synthesis, properties, and applications. *Chemistry of Materials* **2011**, 23, 4085-4093.

Lothenbach, B., Scrivener, K. and Hooton, R.D. Supplementary cementitious materials. *Cement and Concrete Research* **2011**, 41 (12), 1244-1256.

Lu, Y., Yu, H.T., Chen, S., Quan, X. and Zhao, H.M. Integrating plasmonic nanoparticles with TiO_2 photonic crystal for enhancement of visible-light-driven photocatalysis. *Environmental Science & Technology* **2012**, 46, 1724-1730.

Luan, Y., Jing, L., Xie, Y., Sun, X., Feng, Y. and Fu, H. Exceptional photocatalytic activity of 001-facet-exposed TiO_2 mainly depending on enhanced adsorbed oxygen by residual hydrogen fluoride. *ACS Catalysis* **2013**, 3 (6), 1378-1385.

Lucas, S.S., Ferreira, V.M. and Barroso de Aguiar, J.L. Incorporation of titanium dioxide nanoparticles in mortars – Influence of microstructure in the hardened state properties and photocatalytic activity. *Cement and Concrete Research* **2013**, 43, 112-120.

Maira, A.J., Yeung, K.L., Lee, C.Y., Yue, P.L. and Chan, C.K. Size effects in gas-phase photo-oxidation of trichloroethylene using nanometer-sized TiO_2 catalysts. *Journal of Catalysis* **2000**, 192, 185-196.

Marugán, J., Grieken, R.V., Sordo, C. and Cruz, C. Kinetics of the photocatalytic disinfection of *Escherichia coli* suspensions. *Applied Catalysis B: Environmental* **2008**, 82, 27-36.

Marugán, J., Grieken, R.V., Pablos, C. and Sordo, C. Analogies and differences between photocatalytic oxidation of chemicals and photocatalytic inactivation of microorganisms. *Water Research* **2010**, 44, 789-796.

Maury-Ramirez, A. and De Belie, N. Evaluation of the algaecide activity of titanium dioxide on autoclaved aerated concrete. *Journal of Advanced Oxidation Technologies* **2009**, 12, 100-104.

Maury-Ramirez, A., De Belie, N. and Demeestere, K. Self-cleaning and/or air-purifying cementitious materials: Evaluation method. Proceedings 11th FirW PhD Symposium, Ghent University, Belgium, **2010**.

Maury-Ramirez, A., De Muvnck, W., Stevens, R., Demeesterer, K. and De Belie, N. Titanium dioxide based strategies to prevent algal fouling on cementitious materials. *Cement and Concrete Composites* **2013**, 36, 93-100.

Meng, T., Yu, Y., Qian, X., Zhan, S. and Qian, K. Effect of nano-TiO_2 on the mechanical properties of cement mortar. *Construction and Building Materials* **2012**, 29, 241-245.

Micic, O.I., Meglic, M., Lawless, D., Sharma, D.K. and Serpone, N. Semiconductor photophysics. 5. Charge carrier trapping in ultrasmall silver iodide particles and kinetics of formation of silver atom clusters. *Langmuir* **1990**, 6, 487-492.

Mo, J., Zhang, Y., Xu, Q., Lamson, J.J. and Zhao, R. Photocatalytic purification of volatile organic compounds in indoor air: A literature review. *Atmospheric Environment* **2009**, 43 (14), 2229-2246.

Mohseni, M. and David, A. Gas phase vinyl chloride (VC) oxidation using TiO_2-based photocatalysis. *Applied Catalysis B: Environmental* **2003**, 46 (2), 219-228.

Mohseni, E., Miyandehi, B.M., Yang, J. and Yazdi, M.A. Single and combined effects of nano-SiO_2, nano-Al_2O_3 and nano-TiO_2 on the mechanical, rheological and durability properties of self-compacting mortar containing fly ash. *Construction and Building Materials* **2015**, 84, 331-340.

Mukharjee, B.B. and Barai, S.V. Influence of nano-Silica on the properties of recycled aggregate concrete. *Construction and Building Materials* **2014**, 55, 29-37.

Munirathinam, B., Pydimukkala, H., Ramaswamy, N. and Neelakantan, L. Influence of crystallite size and surface morphology on electrochemical properties of annealed TiO_2 nanotubes. *Applied Surface Science* **2015**, 355, 1245-1253.

Nazari, A. and Riahi, S. The effect of TiO_2 naoparticles on water permeability and thermal and mechanical properties of high strength self-compacting concrete. *Materials Science and Engineering A* **2010**, 528 (2), 756-763.

Nazari, A. The effects of curing medium on flexural strength and water permeability of concrete incorporating TiO_2 nanoparticles. *Materials and Structures* **2011**, 44, 773-786.

Neville, A.M. Properties of Concrete, 5th ed. Pearson Education Limited: England, **2011**.

Noguchi, T., Fujishima, A., Sawunytama, P. and Hashimoto, K. Photocatalytic degradation of gaseous formaldehyde using TiO_2 film. *Environmental Science & Technology* **1998**, 32, 3831-3833.

Obee, T.N. and Brown, R.T. TiO_2 photocatalysis for indoor air applications: effects of humidity and trace contaminant levels on the oxidation rates of formaldehyde, toluene, and 1, 3-butadiene. *Environmental Science & Technology* **1995**, 29 (5), 1223-1231.

Obee, T.N. and Hay, S.O. Effects of moisture and temperature on the photooxidation of ethylene on titania. *Environmental Science & Technology* **1997**, 31 (7), 2034-2038.

Ollis, D.F., Pelizzetti, E. and Serpone, N. Photocatalyzed destruction of water contaminants. *Environmental Science & Technology* **1991**, 25 (9), 1523-1529.

Oua, H.H. and Lo, S.L. Photocatalysis of gaseous trichloroethylene (TCE) over TiO_2: The effect of oxygen and relative humidity on the generation of dichloroacetyle chloride (DCAC) and phosgene. *Journal of Hazardous Materials* **2007**, 146, (1-2), 302-308.

Pacheco-Torgal, F. and Jalali, S. Nanotechnology: Advantages and drawbacks in the field of construction and building materials. *Construction and Building Materials* **2011**, 25 (2), 582-590.

Pathakoti, K., Morrow, S., Han, C.S., Pelaez, M., He, X.J., Dionysiou, D.D. and Hwang, H.M. Photoinactivitation of *Escherichia coli* by sulphur-doped and nitrogen-fluorine-codoped TiO_2 nanoparticles under solar simulated light and visible light irradiation. *Environmental Science & Technology* **2013**, 47, 9988-9996.

Pei, C.C. and Leung, W.W.F. Enhanced photocatalytic activity of electrospun TiO_2/ZnO nanofibers with optimal anatase/rutile ratio. *Catalysis Communications* **2013**, 37, 100-104.

Peller, J.R., Whitman, R.L., Griffith, S., Harris, P., Peller, C. and Scalzitti, J. TiO_2 as a photocatalyst for control of the aquatic invasive alga, *Cladophora*, under natural and artificial light. *Journal of Photochemistry and Photobiology A: Chemistry* **2007**, 186 (2-3), 212-217.

Peral, J. and Ollis, D.F. Heterogeneous photocatalytic oxidation of gas-phase organics for air purification-acetone, 1-butanol, butyraldehyde, formaldehyde, and meta-xylene oxidation. *Journal of Catalysis* **1992**, 136 (2), 554-565.

Pérez-Nicolás, M., Balbuena, J., Cruz-Yusta, M., Sánchez, L., Navarro-Blasco, I., Fernández, J.M. and Alvarez, J.I. Photocatalytic NO_x abatement by calcium aluminate cements modified with TiO_2: Improved NO_2 conversion. *Cement and Concrete Research* **2015**, 70,

67-76.

Pichat, P. and Herrmann, J.M. Adsorption-desorption, related mobility and reactivity in photocatalysis. In Photocatalysis: Fundamentals and applications; Serpone, N. and Pelizzetti, E. Eds; *John Willy & Sons: New York*, **1989**.

Poon, C.S. and Cheung, E. NO removal efficiency of photocatalytic paving blocks prepared with recycled materials. *Construction and Building Materials* **2006**, 21 (8), 1746-1751.

Puddu, V., Choi, H., Dionysiou, D.D. and Puma, G.L. TiO_2 photocatalyst for indoor air remediation: Influence of crystallinity, crystal phase, and UV radiation intensity on trichloroethylene degradation. *Applied Catalysis B: Environmental* **2010**, 94, 211-218.

Rachel, A., Subrahmanyam, V. and Boule, P. Comparison of photocatalytic efficiencies of TiO_2 in suspended and immobilized form for the photocatalytic degradation of nitrobenzenesulfonic acids. *Applied Catalysis B: Environmental* **2002**, 37 (4), 301-308.

Rao, S. Silva, P. and de Brito, J. Experimental study of the mechanical properties and durability of self-compacting mortars with nano materials (SiO_2 and TiO_2). *Construction and Building Materials* **2015**, 96, 508-517.

Rincón, A.G. and Pulgarin, C. Fe^{3+} and TiO_2 solar-light-assisted inactivation of *E.coli* at field scale: Implications in solar disinfection at low temperature of large quantities of water. *Catalysis Today* **2007**, 122, 128-136.

Rout, B., Plassais, A., Olive, F., Guillot, L. and Bonafous, L. TiO_2-containing cement pastes and mortars: Measurements of the photocatalytic efficiency using a rhodamine B-based colourimetric test. *Solar Energy* **2009**, 83-10, 1794-1801.

Saccani, A. and Bignozzi, M.C. ASR expansion behavior of recycled glass fine aggregates in concrete. *Cement and Concrete Research* **2010**, 40, 531-536.

Sanchez, B., Cardona, A.I., Romero, M., Avial, P. and Bahamonde, A. Influence of temperature on gas-phase photo-assisted mineralization of TCE using tubular and

monolithic catalysts. *Catalysis Today* **1999**, 54 (2-3), 369-377.

Seipenbusch, M., Rothenbacher, S., Weber, A.P. and Kasper, G. Interparticle forces in nanoparticle agglomerates. In Proc European Aerosol Conference, Austria, **2007**.

Senff, L., Hotza, D., Repette, W.L., Ferreira, V.M. and Labrincha, J.A. Influence of added nanosilica and/or silica fume on fresh and harden properties of mortars and cement pastes. *Advances in Applied Ceramics* **2009**, 108, 418-428.

Senff, L., Hotza, D., Lucas, S., Ferreira, V.M. and Labrincha, J.A. Effect of nano-SiO_2 and nano-TiO_2 addition on the rheological behaviour and the hardened properties of cement mortars. *Materials Science and Engineering A* **2012**, 532, 354-361.

Serpone, N., Lawless, D. and Khairutdinov, R. Size effects on the photophysical properties of colloidal anatase TiO_2 particles: Size quantization or direct transitions in this indirect semiconductor? *The Journal of Physical Chemistry* **1995**, 99, 16646-16654.

Seung, B.P., Bong, C.L. and Jeong, H.K. Studies on mechanical properties of concrete containing waste glass aggregate. *Cement and Concrete Research* **2004**, 34, 2181-2189.

Shevell, S.K. The science of colour. 2nd edition. Elsevier: United Kingdom, **2003**.

Sleiman, M., Ferronato, C. and Chovelon, J.M. Photocatalytic removal of pesticide dichlorvos from indoor air: A study of reaction parameters, intermediates and mineralization. *Environmental Science & Technology* **2008**, 42 (8), 3018-3024.

Sleiman, M., Conchon, P., Ferronato, C. and Chovelon, J.M. Photocatalytic oxidation of toluene at indoor air levels (ppbv): Towards a better assessment of conversion, reaction intermediates and mineralization. *Applied Catalysis B: Environmental* **2009**, 86, 159-165.

Srivastava, A., Kumar, J. and Bansal, A. Photocatalytic application of titanium dioxide in architectural concrete: A review. *International Journal of Scientific Research and Chemical Engineering* **2015**, 1, 24-29.

Stokke, J.M. and Mazyck, D.W. Photocatalytic degradation of methanol using silica-titania

composite pellets: effect of pore size on mass transfer and reaction kinetics. *Environmental Science & Technology* **2008**, 42 (10), 3808-3813.

Strini, A., Cassese, S. and Schiavi, L. Measurement of benzene, toluene, ethylbenzene and o-xylene gas phase photodegradation by titanium dioxide dispersed in cementitious materials using a mixed flow reactor. *Applied Catalysis B: Environmental* **2005**, 61 (1-2), 90-97.

Sugrañez, R., Álvarez, J.I., Cruz-Yusta, M., Mármol, I., Morales, J., Vila, J. and Sánchez, L. Enhanced photocatalytic degradation of NO_x gases by regulating the microstructure of mortar cement modified with titanium dioxide. *Building and Environment* **2013**, 69, 55-63.

Sun, Q. and Xu, Y. Evaluating intrinsic photocatalytic activities of anatase and rutile TiO_2 for organic degradation in water. *The Journal of Physical Chemistry C* **2010**, 114, 18911-18919.

Sunada, K., Watanabe, T. and Hashimoto, K. Studies on photokilling of bacteria on TiO_2 thin film. *Journal of Photochemistry and Photobiology A: Chemistry* **2003**, 156 (1-3), 227-233.

Terrence, R., Thomas, M. and Gruber, K.A. The effect of metakaolin on alkali-silica reaction in concrete. *Cement and Concrete Research* **2000**, 30 (3), 339-344.

Thilagam, A., Simpson, D.J. and Gerson, A.R. A first-principles study of the dielectric properties of TiO_2 polymorphs. *Journal of Physics: Condensed Matter* **2011**, 025901.

Thomas, J.J. A new approach to modelling the nucleation and growth kinetics of tricalcium silicate hydration. *Journal of American Ceramic Society* **2007**, 90 (10), 3282-3288.

Tiano, P. Biodeterioration of cultural heritage: Decay mechanisms and control methods. Proceedings of ARIADNE 9: Workshop on historic materials and their diagnostics, **2002**, online at http://www.arcchip.cz/w09/w09_tiano.pdf.

Topçu, I.B. and Canbaz, M. Properties of concrete containing waste glass. *Cement and Concrete Research* **2004**, 34, 267-274.

Vallee, F., Rout, B., Bonafous, L., Guillot, L., Pimpinelli, N., Cassar, L., Strini, A., Mapelli, E., Schiavi, L., Gobin, C., Andre, H., Moussiopoulos, N., Papadopoulos, A., Bartzis, J., Maggos, T., McIntyre, R., Lehaut-Burnouf, C., Henrichsen, A., Laugesen, P., Amadelli, R., Kotzias, D. and Pichat, P. Cementitious materials for self-cleaning and depolluting façade surface. In Environment-Conscious Materials and Systems for Sustainable Development, Proceedings of the International RILEM Symposium, Japan, 2004; Kashino, N. and Ohama, Y. Eds,; RILEM: Japan, **2004**.

Vorontsov, A.V., Savinov, E.V., Davydov, L. and Smirniotis, P.G. Photocatalytic destruction of gaseous diethyl sulphide over TiO_2. *Applied Catalysis B: Environmental* **2001**, 32, 11-24.

Wang, C.C., Zhang, Z. and Ying, J.Y. Photocatalytic decomposition of halogenated organics over nanocrystalline titania. *NanoStructured Materials* **1997**, 9, 583-586.

Wang, K.H. and Hsieh, Y.H. Heterogeneous photocatalytic degradation of trichloroethylene in vapour phase by titanium dioxide. *Environment International* **1998**, 24 (3), 267-274.

Wang K.H., Tsai, H. and Hsieh, Y. A study of photocatalytic degradation of trichloroethylene in vapor phase on TiO_2 photocatalyst. *Chemosphere* **1998**, 36, 2763-2773.

Wang, Z.M., Yang, G.X., Biswas, P., Bresser, W. and Boolchand, P. Processing of iron-doped titania powders in flame aerosol reactors. *Powder Technology* **2001**, 114, 197-204.

Wolfrum, E.J., Huang, J., Blake, D.M., Maness, P., Huang, Z., Fiest, J. and Jacoby, W.A. Photocatalytic oxidation of bacteria, bacterial and fungal spores, and model biofilm components to carbon dioxide on titanium dioxide-coated surfaces. *Environmental Science & Technology* **2002**, 36, 3412-3419.

Wu, J.F., Hung, C.H. and Yuan, C.S. Kinetic modelling of promotion and inhibition of

temperature on photocatalytic degradation of benzene vapour. *Journal of Photochemistry and Photobiology A: Chemistry* **2005**, 170 (3), 299-306.

Xu, N.P., Shi, Z.F., Fan, Y.Q., Dong, J.H., Shi, J. and Hu, M.Z.C. Effects of particle size of TiO$_2$ on photocatalytic degradation of methylene blue in aqueous suspensions. *Industrial & Engineering Chemistry Research* **1999**, 38, 373-379.

Yamazaki, S., Tanaka, S. and Tsukamoto, H. Kinetic studies of oxidation of ethylene over a TiO$_2$ photocatalyst. *Journal of Photochemistry and Photobiology A: Chemistry* **1999**, 121, 55-61.

Yang, H.G., Liu, G., Qiao, S.Z., Sun, C.H., Jin, Y.G., Smith, S.C., Zou, J., Cheng, H.M. and Lu, G.Q. Solvothermal synthesis and photoreactivity of anatase TiO$_2$ nanosheets with dominant {001} facets. *Journal of the American Chemical society* **2009**, 131, 4078-4083.

Yang, L.Y., Jia, Z.J., Zhang, Y.M. and Dai, J.G. Effects of nano-TiO$_2$ on strength, shrinkage and microstructure of alkali activated slag pastes. *Cement & Concrete Composites* **2015**, 57, 1-7.

Zapata, L., Portela, G., Suárez, O. and Carrasquillo, O. Rheological performance and compressive strength of superplasticized cementitious mixtures with micro/nano-SiO$_2$ additions. *Construction and Building Materials* **2013**, 41, 708-716.

Zhan, Y. Methodology for aesthetic repair and rehabilitation of architectural concrete. Master thesis, University of Johannnesburg, South Africa, **2005**.

Zhang, H., Lv, X.J., Li, Y.M., Wang, Y. and Li, J.H. P25-graphene composite as a high performance photocatalyst. *ACS Nano* **2010**, 4, 380-386.

Zhang, R., Cheng, X., Hou, P.K. and Ye, Z.M. Influences of nano-TiO$_2$ on the properties of cement-based materials: hydration and drying shrinkage. *Construction and Building Materials* **2015**, 81, 35-41.

Zhang, Z.B., Wang, C.C., Zakaria, R. and Ying, J.Y. Role of particle size in nanocrystalline

TiO$_2$-based photocatalysts. *The Journal of Physical Chemistry B* **1998**, 102, 10871-10878.

Zhao, J. and Yang, X. Photocatalytic oxidation for indoor air purification: A literature review. *Building and Environment* **2003**, 38, 645-654.

Zheng, Z.K., Huang, B.B., Qin, X.Y., Zhang, X.Y., Dai, Y., Jiang, M.H., Wang, P. and Whangbo, M.H. Highly efficient photocatalyst: TiO$_2$ microspheres produced from TiO$_2$ nanosheets with a high percentage of reactive {001} facets. *Chemistry A European Journal* **2009**, 15, 12576-12579.

Zhu, X.B., Chang, D.L., Li, X.S., Sun, Z.G., Deng, X.Q. and Zhu, A.M. Inherent rate constants and humidity impact factors of anatase TiO$_2$ film in photocatalytic removal of formaldehyde from air. *Chemical Engineering Journal* **2015**, 279, 897-903.

Zorn, M.E., Tompkins, D.T., Zeltner, W.A. and Anderson, M.A. Photocatalytic oxidation of acetone vapour on TiO$_2$/ZrO$_2$ thin films. *Applied Catalysis B: Environmental* **1999**, 23 (1), 1-8.